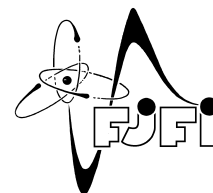




CZECH TECHNICAL UNIVERSITY IN PRAGUE
Faculty of Nuclear Sciences and Physical
Engineering



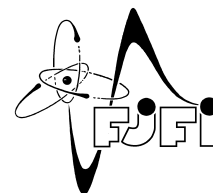
Transverse expansion in nuclear collisions at RHIC BES

Diploma thesis

Author: **Bc. Jakub Štěrba**
Supervisor: **prof. Dr. Boris Tomášik**
Consultant: **Dr. Iurii Karpenko**
Academic year: 2021/2022



ČESKÉ VYSOKÉ UČENÍ TECHNICKÉ V PRAZE
Fakulta jaderná a fyzikálně inženýrská



Příčná expanze v jaderných srážkách na RHIC BES

Diplomová práce

Autor: **Bc. Jakub Štěrba**
Vedoucí práce: **prof. Dr. Boris Tomášik**
Konzultant: **Dr. Iurii Karpenko**
Akademický rok: 2021/2022



Katedra: fyziky

Akademický rok: 2021/2022

ZADÁNÍ DIPLOMOVÉ PRÁCE

Student: Bc. Jakub Štěrba

Studijní program: Jaderná a částicová fyzika

Název práce: Příčná expanze v jaderných srážkách na RHIC BES
(česky)

Název práce: Transverse expansion in nuclear collisions at RHIC BES
(anglicky)

Pokyny pro vypracování:

- 1) Nastudujte formalismus viskózní relativistické hydrodynamiky, včetně členu s objemovou viskozitou
- 2) Proved'te simulace srážek Au+Au při 27 GeV na NN pár za pomoci hybridního modelu GLISSANDO + vHLLE + SMASH a porovnejte je s daty. Do inicializace vHLLE přidejte anizotropní příčný tok.
- 3) Zkonstruujte Monte Carlo Glauberovský model, ve kterém se připustí možnost příčné hybnosti pro deponovanou energii. Použijte tento model jako počáteční podmínky pro hydrodynamické simulace.
- 4) Porovnejte nové simulace s daty ze spekter v příčné hybnosti a s měřeným eliptickým tokem.

Doporučená literatura:

- [1] Iu. Karpenko, P. Huovinen and M. Bleicher: A 3+1 dimensional viscous hydrodynamic code for relativistic heavy ion collisions, *Comput. Phys. Commun* 185 (2014) 3016-3027
- [2] Iu. Karpenko, P. Huovinen, H. Petersen and M. Bleicher: Estimation of the shear viscosity at finite net-baryon density from A+A collision data at $\sqrt{s_{NN}} = 7.7 - 200$ GeV, *Physical Review* 91 (2015) 064901
- [3] J. Weil, et al.: Particle production and equilibrium properties within a new hadron transport approach for heavy-ion collisions, *Physical Review C* 94, 054905 (2016)
- [4] M. Rybczynski, G. Stefaniak, W. Broniowski and P. Božek: GLISSANDO 2: Glauber Initial State Simulation and more..., ver. 2, *Computer Physics Communication* 185, 1759 (2014)

Jméno a pracoviště vedoucího diplomové práce:

prof. Dr. Boris Tomášik, Ph.D.

Katedra fyziky, Fakulta jaderná a fyzikálně inženýrská ČVUT v Praze

Jméno a pracoviště konzultanta:

Dr. Iurii Karpenko

Katedra fyziky, Fakulta jaderná a fyzikálně inženýrská ČVUT v Praze

Datum zadání diplomové práce: 20.10.2021

Termín odevzdání diplomové práce: 02.05.2022

Doba platnosti zadání je dva roky od data zadání.



.....
garant studijního programu



.....
vedoucí katedry



.....
děkan

V Praze dne 20.10.2021

Čestné prohlášení:

Prohlašuji, že jsem svou diplomovou práci vypracoval samostatně a uvedl jsem všechnu použitou literaturu.

Nemám závažný důvod proti použití tohoto školního díla ve smyslu §60 Zákona č. 121/2000 Sb., o právu autorském, o právech souvisejících s právem autorským a o změně některých zákonů (autorský zákon).

V Praze dne 2. května 2022

Jakub Štěrba

Acknowledgement:

I would like to express my gratitude to my supervisor prof. Dr. Boris Tomášik for his guidance, valuable advice and also for his kind attitude, which kept me motivated throughout the work. He has taught me a lot and it has always been a pleasure to work with him. Further, I thank to Dr. Iurii Karpenko for answering all my questions and for helpful discussions we had. I also thank to Ing. Jakub Cimerman for his invaluable help with technical and practical issues of my work and without whom the work would be much more troublesome.

Last but not least, I sincerely thank to my beloved ones who have always tirelessly supported me.

Jakub Štěřba

Název práce:

Příčná expanze v jaderných srážkách na RHIC BES

Autor: Bc. Jakub Štěrba

Studijní program: Jaderná a částicová fyzika

Druh práce: Diplomová práce

Vedoucí práce: prof. Dr. Boris Tomášik, ČVUT, FJFI, Jaderná a částicová fyzika

Konzultant: Dr. Iurii Karpenko, ČVUT, FJFI, Experimentální jaderná a částicová fyzika

Abstrakt: Během srážek těžkých iontů vzniká velmi horká silně interagující hmota, která při dostatečné energii může přejít do stavu kvark-gluonového plazmatu. Na počátku srážky je energie rozdělena nerovnoměrně a jelikož se vzniklá hmota chová kolektivně, dochází k jejímu anizotropickému vývoji. Počítačovou simulací srážek a porovnávám výsledků s experimentálně naměřenými daty je možné silně interagující hmotu studovat. Jednou z možností, jak simulovat kolektivní vývoj kvark-gluonového plazmatu je pomocí hydrodynamických modelů, kdy je plazma popisováno jako viskózní tekutina. Řešení hydrodynamických modelů jsou však závislé na počátečním stavu. Jedním z experimentů snažícím se prozkoumat fázový diagram silně interagující hmoty je program RHIC BES, během nějž byla nabírána data ze srážek Au+Au při energiích $\sqrt{s_{NN}} = 7.7 - 62.4$ GeV. Kolaborací STAR byly prezentovány výsledky eliptického toku a spekter v příčné hybnosti. Úkolem této práce je konstrukce nového Glauberovského modelu, ve kterém je možné připustit počáteční příčnou hybnost, která povede na počáteční příčnou expanzi v hydrodynamickém modelu vHLL. Společně s vHLL je použit transportní model SMASH pro simulaci koncového stavu. Výsledky simulací s novým modelem jsou porovnány s výsledky kolaborace STAR a s výsledky simulací s generátorem počátečních podmínek Glissando pro energii srážky $\sqrt{s_{NN}} = 27$ GeV a pro centralitu 10-20%, 20-30% a 30-40%.

Klíčová slova: anizotropie, Beam Energy Scan, centralita, eliptický tok, Glauber model, hydrodynamický model, kvark-gluonové plazma, srážky těžkých iontů

Title:

Transverse expansion in nuclear collisions at RHIC BES

Author: Bc. Jakub Štěrba

Study program: Nuclear and Particle Physics

Sort of project: Diploma thesis

Supervisor: prof. Dr. Boris Tomášik, CTU, FNSPE, Nuclear and Particle Physics

Consultant: Dr. Iurii Karpenko, CTU, FNSPE, Nuclear and Particle Physics

Abstract: During heavy-ion collisions a very hot and dense strongly interacting matter is created. Such matter can pass into the state of quark-gluon plasma, if sufficient energy density is reached. At the beginning of the collision, the energy is distributed unevenly and since the created matter behaves collectively, it leads to its anisotropic evolution. It is possible to study the strongly interacting matter by computer simulations and comparing the results to the experimental data. One of the approaches for simulation of the quark-gluon plasma evolution is by means of hydrodynamic models, where the plasma is described as a viscous fluid. However, the solutions of hydrodynamic models are strongly dependent on the initial state. One of the experiments, the aim of which is to probe the phase diagram of the strongly interacting matter is RHIC BES program, during which Au+Au collisions at the energies $\sqrt{s_{NN}} = 7.7 - 62.4$ GeV were taken. There were presented results of the elliptic flow and particle spectra in transverse momentum by STAR collaboration. The aim of this work is to create a new Glauber model, which would allow initial transverse momentum deposition that would lead to an initial transverse expansion in hydrodynamic code vHLLE. Altogether with vHLLE code, the SMASH transport model is used for final state simulations. Results from the simulations with the new model are compared to the results presented by STAR collaboration and also with results from the simulations with Glissando initial state generator for collision energy $\sqrt{s_{NN}} = 27$ GeV and for the centralities 10-20%, 20-30% a 30-40%.

Key words: anisotropy, Beam Energy Scan, centrality, elliptic flow, Glauber model, heavy-ion collisions, hydrodynamic model, quark-gluon plasma

Contents

| | |
|------------------------------------------------------------------|-----------|
| Introduction | 17 |
| 1 High energy heavy-ion collisions | 19 |
| 1.1 Brief introduction to quantum chromodynamics | 19 |
| 1.2 Quark-Gluon Plasma | 21 |
| 1.2.1 Time evolution of collision | 22 |
| 1.2.2 Particle p_T spectrum | 24 |
| 2 Glauber model and centrality of the collision | 27 |
| 2.1 Glauber model | 27 |
| 2.1.1 Optical Glauber model | 28 |
| 2.1.2 Glauber Monte Carlo | 30 |
| 2.2 Centrality definition | 30 |
| 3 Expansion of the medium | 33 |
| 3.1 Anisotropic flow | 34 |
| 3.1.1 Elliptic flow centrality dependence | 36 |
| 3.1.2 Elliptic flow momentum dependence | 36 |
| 3.1.3 Measurement of flow | 37 |
| 4 Hydrodynamic modelling | 39 |
| 4.1 Relativistic ideal fluid dynamics | 39 |
| 4.2 Relativistic viscous hydrodynamics | 40 |
| 4.3 Basic principles of hydrodynamic numerical methods | 42 |
| 5 Hybrid vHLLE package | 45 |
| 5.1 Initial conditions | 45 |
| 5.1.1 Glissando | 45 |
| 5.2 vHLLE | 46 |
| 5.3 hadronSampler | 49 |
| 5.3.1 SMASH | 49 |
| 6 Beam Energy Scan at RHIC | 51 |
| 6.1 Particle spectra from BES | 52 |
| 6.2 Elliptic flow from BES | 52 |
| 7 Motivation | 55 |
| 7.1 Adding initial velocity to hydrodynamic grid | 55 |
| 8 IMAGO: Glauber model with initial momentum anisotropy | 61 |
| 8.1 Basic principles of IMAGO | 61 |
| 8.1.1 Generating nuclei | 61 |

| | | |
|----------|-------------------------------------------------------|-----------|
| 8.1.2 | Collision of nuclei | 63 |
| 8.1.3 | Centrality determination | 65 |
| 8.2 | Introducing initial transverse momentum | 68 |
| 8.2.1 | Output from IMAGO | 69 |
| 8.3 | Implementing initial p_T into vHLLE hydro | 69 |
| 9 | Results | 77 |
| | Conclusion | 81 |

Introduction

There are four fundamental forces in the current physical description of the nature - weak, strong, electromagnetic and gravitational. Each of these forces influence the nature significantly, however, the strong force is of the main interest in this work. It manifests itself on small scales and therefore this is exactly the force, which causes binding of the elementary particles into structures one can observe quite regularly - most importantly protons and neutrons.

One of the key questions in contemporary physics is to describe the behaviour of the strongly interacting matter. At some region of energy scales, the predictions can be obtained from *quantum chromodynamics* (QCD) calculations, however, at other regions, the first principles of QCD are not applicable and complex models, which are very computationally demanding, are able to describe such systems only in limited measure. One of such systems, which are challenging to describe, is also *quark-gluon plasma* (QGP), i.e. strongly interacting matter under extreme conditions, when very high temperatures, high energy densities and high pressures are present. It is a state of matter, when quarks and gluons, usually bound in hadrons, suddenly become asymptotically free. It is believed that the matter is in such a state during the compact star merging and that it was in this state even a few moments after the Big Bang.

Experimentally, the matter under such extreme conditions is hard to observe. Nevertheless, it can be observed by means of particle accelerators and colliders. For the study of the quark-gluon plasma, collisions of heavy nuclei, or rather heavy ions, are the most effective. In the colliders, the nuclei are accelerated in the opposite directions and then collided at given place. If the collision is strong enough, such extreme conditions as mentioned above, can be created and the matter can be studied. The most significant experiments in current research of heavy-ion collisions are ALICE at CERN in Geneva and STAR at BNL in the United States.

Once the nuclei collided and a small droplet of quark-gluon plasma is created, the matter starts to evolve. From the data, it can be seen that the evolution of the matter shows collective behaviour and one of the fundamental features of such collectivity is *flow*, which can be measured and then the properties of the strongly interacting matter studied. The phase of QGP lasts, however, for a very small period of time, after which quarks and gluons start to form various particle species. These particles are detected in a detector surrounding the area where the QGP was formed and the quantities such as mass, velocity or momentum of the particles are measured. Such measurements give information about the collision, thus about the strongly interacting matter.

There are several ways how to describe the evolution of QGP from the point of view of phenomenological models. First approach is based on the microscopical description of the system, i.e. simulates the behaviour of each particle and the interactions between them. These kinds of setups are called *transport models*. The other approach, which is also used in this work, is the approach of *hydrodynamic modelling*. As already foreseen above, the quark-gluon plasma can be looked at as a droplet of a liquid, and therefore can be described by the hydrodynamic equations. However, the QGP is not an ideal fluid and thus the viscosity of the fluid has to be considered, as well.

In Chapter 1, basic problems in heavy-ion collisions, QGP formation, the quantities measured and their significance for the description of strongly interacting matter are briefly introduced. Description of the optical Glauber model and Glauber Monte Carlo, together with

discussion of the centrality of a collision can be found in Chapter 2. The expansion of the QGP, the anisotropic flow and methods for its measurement are described in Chapter 3. In Chapter 4, the basics of the hydrodynamical approach to the expansion of the medium are noted together with basic principles of hydrodynamic modelling. The Chapter 5 presents a particular hydrodynamic model vHLE, initial state generator Glissando and final state simulator SMASH within the vHLE hybrid package. In Chapter 6, the experimental data of elliptic flow and particle p_T spectra from RHIC BES program reported by STAR collaboration are shown. The Chapter 7 is the first part, where a new contributions of this work are presented, starting by its motivation. A new Monte Carlo Glauber model for simulation of the initial state for heavy-ion collisions, IMAGO, is presented in Chapter 8. In the last Chapter 9, the results from the new model are discussed and compared to the original results with Glissando.

Chapter 1

High energy heavy-ion collisions

In this work, we are particularly focused on the physics of high energy heavy-ion collisions, also called heavy-ion physics (HIP). This incorporates collisions of heavy nuclei, such as ^{197}Au or ^{208}Pb , which are probably the most common heavy-ions used. For $\sqrt{s} \geq 10$ GeV the kinetic energy of such colliding nucleus is much bigger than its rest energy. Since the collision of systems of such kind is very complicated many-body problem, it cannot be described by first principles of the strong interaction, quantum chromodynamics. Nevertheless, some further approaches to treat such problem have been developed.

1.1 Brief introduction to quantum chromodynamics

In the first place, let us introduce a theory which describes the strong interaction - quantum chromodynamics (QCD). The main components of the theory are *quarks* and *gluons*. Both of these are elementary particles of the Standard Model. There are six *flavours* (kinds) of quarks - *up*, *down*, *charm*, *strange*, *top* and *bottom*. In addition, there are eight gluons - to see which, read further discussion. Moreover, the gluons are the mediators of the strong interaction. Gluons are massless, it is important however, that unlike for photons in quantum electrodynamics, the gluons can interact among themselves.

In QCD, a new quantum number called *color charge* is introduced. There are three quantum states which span the possible space for the quarks. These are customarily referred to as blue, red, and green. In addition, corresponding anti-color states are there for the antiquarks. On the other hand, each gluon carries both, color and anti-color charge. Altogether, there are nine possible color charge combinations for gluon, however, only eight of them are physical. Any bound state of the quarks and antiquarks has to be *colorless*, in other words the final color charge has to be zero. This is due to the property of strong interaction called *color confinement*. This property states that color-charged particle cannot be isolated. Simple illustration can be made using an example of a bound state of a quark-antiquark pair. The bound state is colorless. If we imagine increasing of the distance between the quarks, it is more energetically favourable to produce a quark-antiquark pair and split the bond between the original quark-antiquark pair. Thus we arrive with two quark-antiquark pairs. Then again, under extreme conditions of matter, color deconfinement can happen and quarks can move freely in relative scale, but even at distances larger than size of a nucleon.

The strength of the interaction is represented by coupling constant $\alpha_s(Q^2)$. In spite of calling $\alpha_s(Q^2)$ a constant, it is not constant at all, rather a function of the momentum transfer Q , (Fig.1.1). The form of the dependence can be quite easily analytically expressed only to the first order of the perturbative series as

$$\alpha_s(Q^2) = \frac{12\pi}{(33 - 2n_f) \ln\left(\frac{Q^2}{\Lambda^2}\right)}, \quad (1.1)$$

where n_f is the number of flavours and Λ is the *QCD scale parameter*, where the coupling becomes relatively large. For the number of flavours $n_f \leq 16$ the coupling constant decreases as the Q^2 grows. From this, the characteristic behaviour of strong interaction can be deduced - the asymptotical freedom.

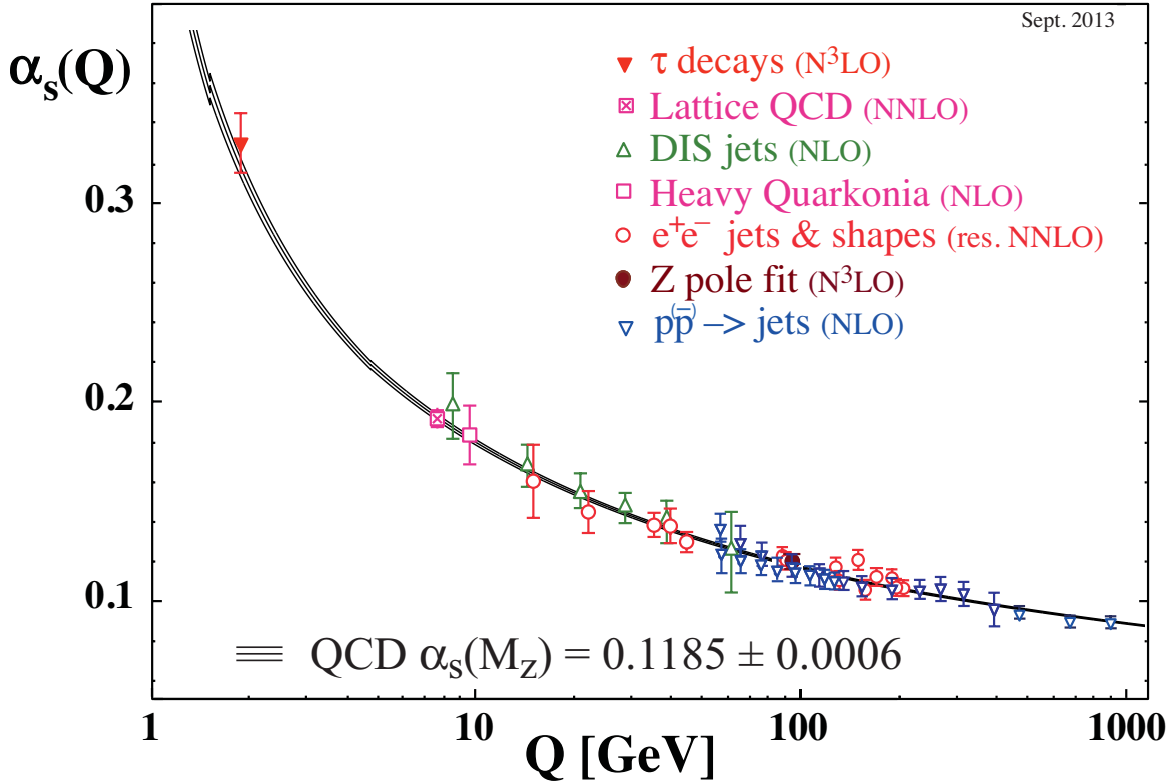


Fig. 1.1: The dependence of strong coupling constant α_s as a function of momentum transfered Q . Figure taken from [1].

It can be seen that for small values of momentum transfer the α_s eventually rises up to values close to unity. For these values of the coupling, the matter is in state, when quarks are confined and the strong processes are happening at large distances, such as size of a hadron. In this region, perturbative QCD computations cannot be used, since the calculations cannot be organised in series of powers of the small coupling constant, but non-perturbative approaches, such as lattice QCD computations, are helpful. Lattice QCD is a discrete theory the principle of which is that the space-time is divided into a space-time lattice. It is based on explicit calculation of action, which is then used for computation of the partition function of the system. In order to be more illustrative, the whole process can be simplified into an image, when quarks are located in the corners of the lattice and gluons are being exchanged along the lattice links. This approach is computationally very demanding and therefore high-performance computers are needed. That is why the precision of some of the results includes rather considerable errors, as the lattice has to be chosen smaller, i.e. the gaps between the cells of the lattice are larger.

At high values of the momentum transfer and small distances of the processes, the typical behaviour of strong interaction can be deduced. As values of α_s in this region are much smaller than 1, in fact $\alpha_s \approx 0.1$, interesting phenomenon called *asymptotic freedom* occurs. Since the interaction gets weaker as α_s decreases, the quarks and gluons become relatively free and are

not confined in hadrons anymore. In this regime the perturbative QCD approach can be used.

These properties of strong interaction give a sufficient ground for quark-gluon plasma formation.

1.2 Quark-Gluon Plasma

There are important predictions from lattice QCD calculations when the temperature of the matter is ascending. As the temperature reaches higher values, a strong rise in thermodynamic observables such as pressure, energy density or entropy, occurs (see Fig.1.3). This may be caused by a phase transition of some kind and thus a sudden increase in the number of degrees of freedom, when partons (quarks and gluons) are deconfined from hadrons. Such transition into the quark-gluon plasma state of matter was estimated to happen at the critical temperature $T_c = 156.5 \pm 1.5$ MeV (see [2]).

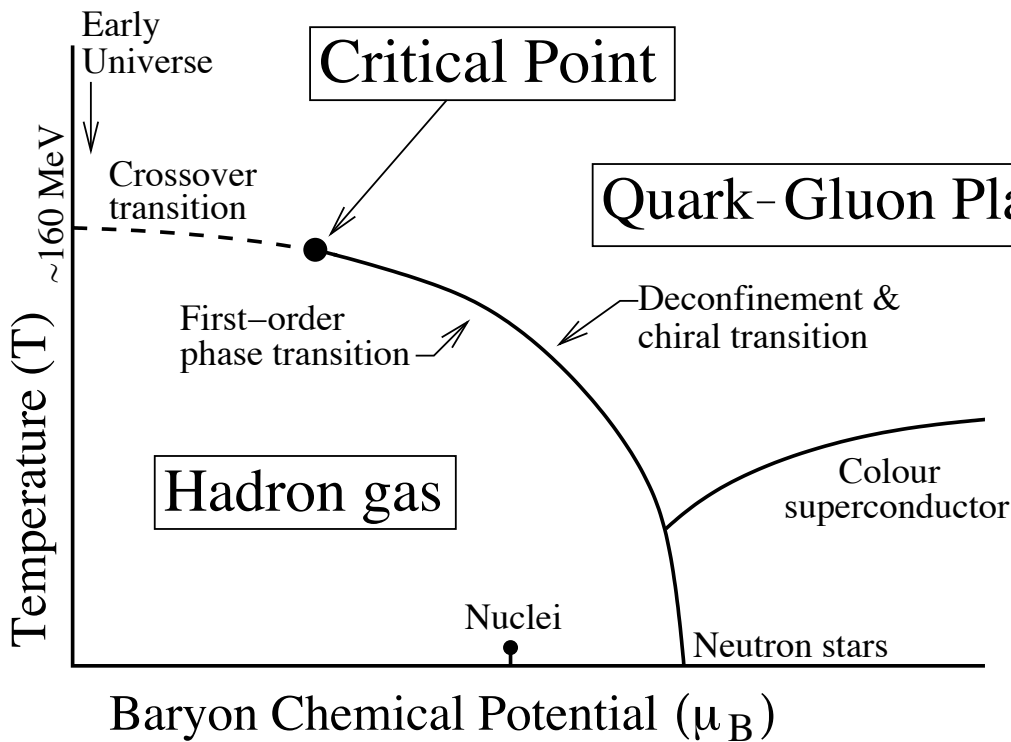


Fig. 1.2: An outline of phase diagram of strongly interacting matter. Figure taken from [3].

In fact, the transition to the QGP phase is not the only kind of phase transition which occurs at this stage. There is also an important transition called *chiral symmetry restoration*. Chiral symmetry is a symmetry which tells that the constituent mass of the quarks is fully due to Higgs mechanism. However, for light confined quarks this symmetry is violated and the constituent masses of light quarks are much bigger than their masses according to Higgs mechanism. The interesting part here is that the temperatures for parton deconfinement and chiral symmetry restoration are very close to each other. This happens to be really a coincidence since there are no links from the first principles of QCD for this to happen.

In order to systemize the behaviour of the strongly interacting matter, there is an effort to study a *phase diagram*. Usually, such phase diagram is constructed as a dependence on the temperature T and *baryon chemical potential* μ_B . Baryon chemical potential, as one of the fundamental thermodynamic variables, expresses the number of baryons against the number of antibaryons at the area of the collision. At high energies of the collision, like at the LHC, the baryon chemical potential is nearly zero $\mu_B \sim 0$ and the ratio of the number of baryons against

antibaryons is close to unity. If this was not the case, any of the initial baryons present in the incoming nucleus would have to slow down dramatically in order to stay at the area of the collision, which, however, does not happen due to the high energy. This is close to the *Bjorken scenario*, see [4]. At lower collision energies, on the other hand, the baryon chemical potential is higher because it is much likely for a baryon to stay in the area of the collision and therefore the ratio of the number of baryons against the number of antibaryons is much bigger than unity. This is close to the *Landau scenario*, see [5].

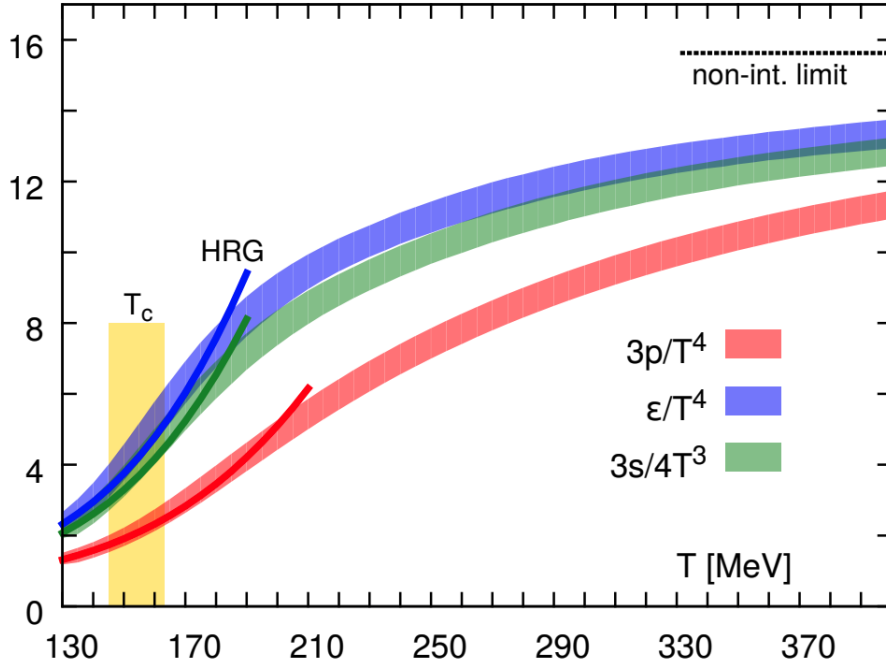


Fig. 1.3: Computations from lattice QCD for suitably normalized pressure $\frac{3p}{T^4}$, energy density $\frac{\epsilon}{T^4}$ and entropy density $\frac{3s}{4T^3}$ as a function of temperature T . The critical temperature $T_c = (154 \pm 9)$ MeV. Figure taken from [6].

Now, having the ingredients needed, the shape of the phase diagram of strongly interacting matter can be roughly estimated (Fig.1.2). The state of matter at normal conditions is represented by *Nuclei* at a non zero baryon chemical potential and relatively low temperature. The point sits at those values of μ_B , where there is a natural matter-antimatter imbalance in the nuclei. The solid curve represents the phase transition of first order from *hadron gas*, where partons are still bound in hadrons, to the QGP phase, in which partons are deconfined and the chiral symmetry is restored. This line is assumed to be ended at a *critical point*. The critical point, like in classical thermodynamics, represents a point in the phase diagram at which both phases merge together into a single phase at this point a phase transition is of the second order or also called *continuous phase transition*. From the mathematical point of view, at the critical point the correlation lengths diverge. The transition beyond this point is called *crossover transition* and this transition is fast and smooth without latent heat. LHC and RHIC at their maximum energies operate in this region. In addition, there are more phases of strongly interacting matter expected, such as *color superconduction*, but the discussion is beyond this work.

1.2.1 Time evolution of collision

Let us have a look at the collision itself and the evolution of the matter right after the collision. For the nuclei accelerated to velocities comparable to the velocity of light, relativistic

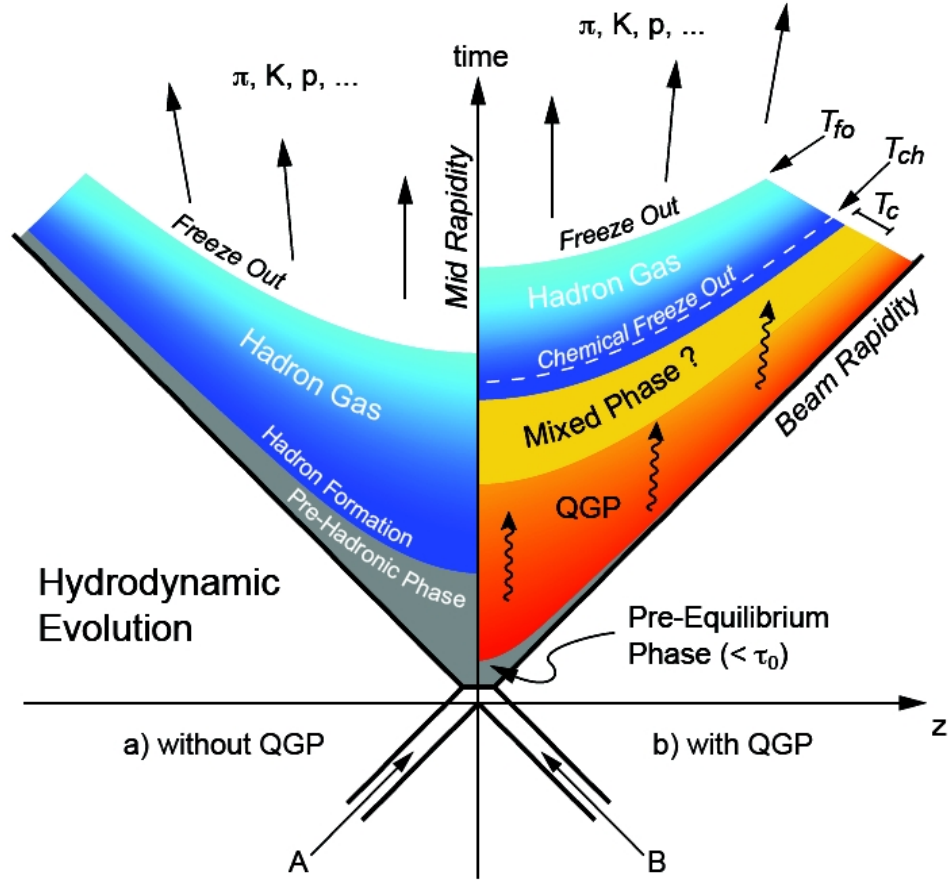


Fig. 1.4: Time evolution of the collision. Left side of the graph (a) shows the evolution of collisions where sufficient conditions are not reached and QGP is not formed. The right side of the graph (b) depicts the evolution when QGP is formed. Figure taken from [7].

effects appear. For high energies, the nuclei are Lorentz-contracted and collide in the form of *discs* or rather funnily *pancakes*. The first stage during the collision is *pre-equilibrium* phase. At this stage the disc-shaped nuclei begin to penetrate each other and inelastic interactions between nucleons take place. Due to the inelasticity of the collision, the energy is transferred from the *longitudinal* direction, which is the direction of flight of the nucleus, to the *transverse plane*, the plane perpendicular to the longitudinal direction. Therefore, high transverse momentum particles are created at this stage. Further inelastic and elastic processes of the partons cause the system to thermalize. At this stage, the energy density of the system is very high. Such a thermalized system shows collective behaviour and the presence of internal pressure causes the system to expand. During the expansion, the system is cooling down until the critical temperature, or rather critical energy density, is reached. At this point the system is already dilute enough so the *hadronization* begins to happen. Partons start to form hadrons via two ways - fragmentation for more energetic partons, when the final hadron has a lower momentum than the leading parton, and coalescence for partons with lower energy, when the final hadron has a higher momentum. The hadronization stops at the point of the *chemical freeze-out*, e.i. the point at which the ratio of hadron yields stays constant. However, formed hadrons can still interact elastically, but only up to the point of *kinetic freeze-out*, i.e. the point at which the medium becomes so dilute that the hadrons do not interact between each other. After this point, resonances created from the medium can decay and thus particles detected by the detector do not fully correspond to those, which were created directly from the medium. Some resonances can be reconstructed efficiently, since they decay at some distance from the primary collision.

However, if quark-gluon plasma is not created during the collision, which is the case e.g. for collisions at lower energies, the evolution is slightly different. The matter created also behaves

collectively, but the final hadrons are set earlier and are not created in the hadronization process but by direct interactions.

An illustration of the timeline of the evolution, as well as comparison of the two cases, can be seen in the Fig.1.4.

1.2.2 Particle p_T spectrum

The particle spectrum (Fig.1.5) can be divided into two parts. At the low transverse momentum p_T , there is a *bulk* or *soft* part of the spectrum. These particles are created during the processes in the QGP. Most of the particles are produced in this region. Moreover, this is exactly the region, where α_s has a high value and a non-perturbative QCD approach must be used. The other part of the spectrum, at a rather high transverse momentum, is called *hard* part. This part could basically be described by the perturbative QCD, since the momentum transferred Q is high here, but particles in this region of the spectrum are affected by the medium and thus cannot be computed from the first principles either.

One of the reasons, why one should study particle spectrum is that it can be approximated as an exponential function of the transverse mass $m_T = \sqrt{m^2 + p_T^2}$ given by $\propto \exp(-m_T/T)$, where m is the mass of a particle species and T plays the role of the inverse slope parameter. If the inverse slope is studied as a function of hadron mass, it can be interpreted as the spectrum is observed *blue-shifted*, i.e. it appears to have higher temperature T . This occurs, since the medium expands with some transverse velocity and thus the spectrum has not only the temperature component, but also the collective velocity component. If the mean velocity of the particles is the same, the more massive ones has to have larger momentum. That is why one can observe an increase of the inverse slope with the hadron mass, i.e. flatter spectrum, if the transverse expansion is present. An example is shown at the end of Chapter 3.

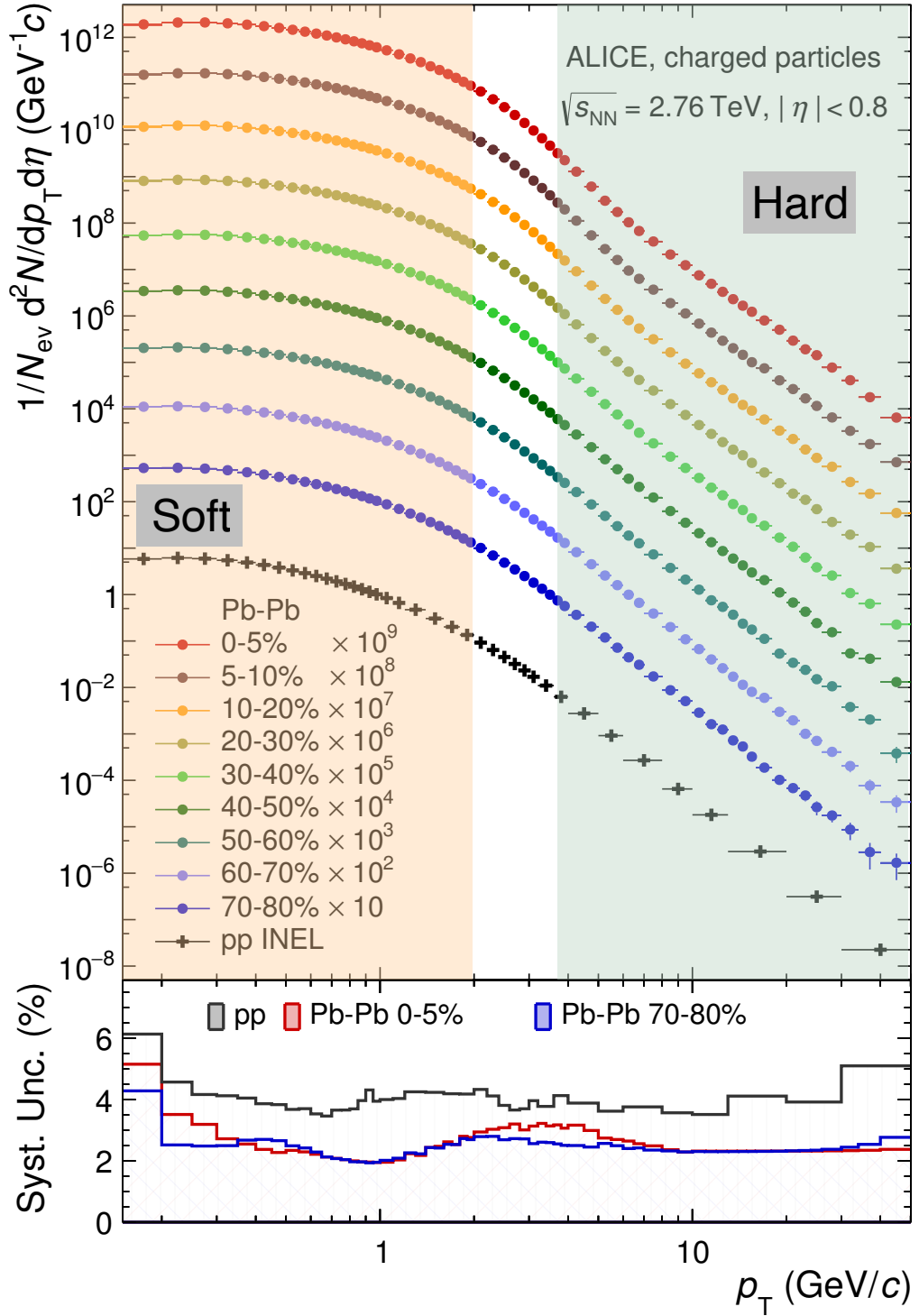


Fig. 1.5: A typical particle p_T spectrum. The spectrum is plotted for charged hadrons from Pb+Pb collisions at $\sqrt{s_{NN}} = 2.76 \text{ TeV}$ for different centralities. The orange panel represents the soft part of the spectrum whereas the blue panel represents the hard part. Figure taken from [8] and modified.

Chapter 2

Glauber model and centrality of the collision

Since the collisions do not always happen head-on, it is convenient to categorize them into centrality classes. It is favourable also for better understanding and description of the physics of the collisions. Therefore the centrality of a collision is introduced.

In simplicity, when two nuclei collide, only the overlapping area of the two nuclei is in fact the region of the actual collision. This region varies from collision to collision and the fashion in which a collision occurs affects further evolution. From the point of view of the particle multiplicity, let us as an example compare a central collision, where both of the nuclei fully overlap, and a peripheral collision, where the overlapping area is small. The multiplicity of the particles in the central collision is much higher than in the peripheral ones and also the effects of the QGP medium are shown most, whereas in peripheral collisions the effect of the QGP might not be even noticeable. Unfortunately, in an experiment it is impossible to distinguish the centrality of a collision directly, however, using a model which would connect the particle multiplicity with a corresponding centrality of the collision, it can be sorted later.

2.1 Glauber model

Firstly, before the whole mechanism of the Glauber model will be explained, let us introduce some fundamental quantities and terms. One of the most significant is the *impact parameter* b and it is defined as the distance between the centers of the colliding nuclei in the transversal plane, i.e. the plane perpendicular to the direction of the flight of the nuclei (see Fig.2.1). From the definition it is clear that for purely central collisions $b = 0$ and for any non-central ones $b > 0$. There are also two types of the nucleons from the collision point of view. The first type is *participants*, which are those nucleons which undergo at least one nucleon-nucleon interaction, and thus indeed participate in the actual collision. The other type of the nucleons is *spectators*. Spectators are the remaining nucleons which do not participate in the actual collision in a sense that they do not interact with the nucleons from the other nucleus, and they eventually fly away in the original direction. There are also *wounded nucleons* which are the nucleons which undergo at least one *inelastic* nucleon-nucleon interaction. However, for most of the cases, the wounded nucleons and participants coincide and the terms are interchangeable.

The Glauber model was designed and described in the 1950s by Roy J. Glauber. According to [9], there were no systematic calculations treating the many-body nuclear systems as a projectile or as a target. Moreover, the results of the model were consistent with the experimental results.

Now, let us have a look at the general basic assumptions and ideas of the Glauber model. It is a geometrical model that treats the collision of the nuclei by following individual nucleons as they pass the another nucleus. It is assumed in the model that for each subsequent collision the

inelastic cross section is constant. The main idea is that the nucleons from one nucleus (projectile) traverse the other nucleus (target) on straight lines and can undergo multiple collisions with the nucleons from the target. The assumption of traversing the nucleus on straight line is valid since the deflection sideways at high energies can be neglected for the time until the next nucleon arrives. One last assumption is that the interactions between the nucleons during the collision are independent.

For the model, nevertheless, some data are needed to be given as an input. First, the density profile of the nucleons inside the nucleus is needed. Usually, the Woods-Saxon distribution of such nuclear density is used, the form of which is

$$\rho(r) = \frac{\rho_0}{1 + \exp(\frac{r-R}{a})}, \quad (2.1)$$

where R is the radius of a nucleus, a is the thickness of the skin layer of a given nucleus and ρ_0 is the density in the center of the nucleus. The other important input is a cross section of inelastic nucleon-nucleon collisions, which can be obtained from experimental measurement of proton-proton collisions.

The Glauber model exists basically in two forms, the analytical *Optical Glauber model* and numerical *Monte Carlo Glauber model*. Firstly, let us take a look at the analytical approach.

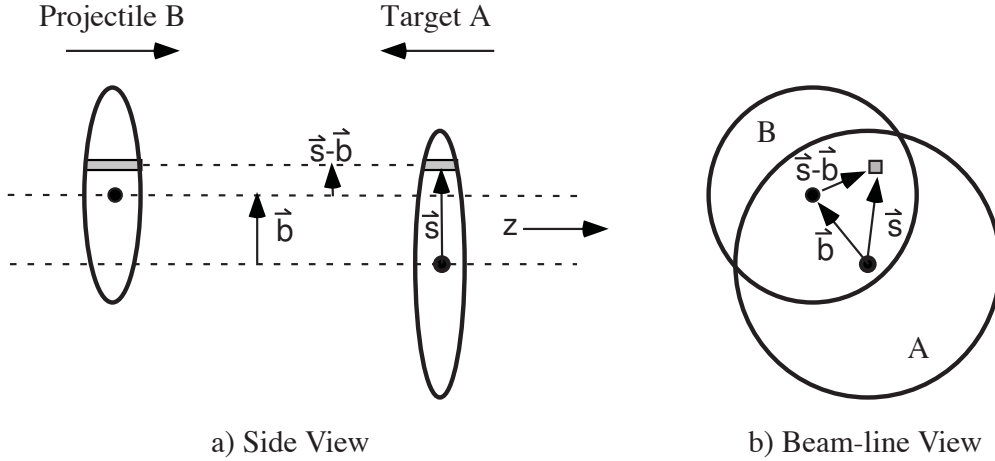


Fig. 2.1: A sketch of the collision of two different nuclei in a) side view and b) view in the direction of the flight of the nuclei. The impact parameter b , displacement s and flux tube (grey area) are also illustrated. Figure taken from [9].

2.1.1 Optical Glauber model

Let us now focus on the analytical derivation of the model. Consider a simple situation when two different nuclei are colliding and we shall name one of them *projectile B* and the other *target A*. As it is illustrated in Fig.2.1, we focus on the flux tubes located at the displacement \vec{s} within the transverse plane with respect to the target A or $\vec{s} - \vec{b}$ to the projectile B respectively. The probability per unit transverse area of a given nucleon being located in the target flux tube in nucleus A is

$$\hat{T}_A(\vec{s}) = \int \rho_A(\vec{s}, z_A) dz_A \quad \text{and} \quad \int \hat{T}_A(b) d^2b = 1, \quad (2.2)$$

where $\rho_A(\vec{s}, z_A)$ is a probability density of finding a nucleon at the point (\vec{s}, z_A) . The probability ρ_A was obtained from (2.1) by dividing by the nucleon number A . The joint probability per

unit area of nucleons being located in the respective overlapping flux tubes of a differential area d^2s of the target and the projectile can be expressed as $\hat{T}_A(\vec{s})\hat{T}_B(\vec{s}-\vec{b})d^2s$. From this, the joint probability can be integrated to obtain a *thickness function*

$$\hat{T}_{AB}(\vec{b}) = \int \hat{T}_A(\vec{s})\hat{T}_B(\vec{s}-\vec{b})d^2s, \quad (2.3)$$

which has a unit of inverse area. The corresponding probability of one nucleon-nucleon interaction to occur is $\hat{T}_{AB}(\vec{b})\sigma_{inel}^{NN}$, where σ_{inel}^{NN} is the cross section of the nucleon-nucleon inelastic interaction. Now, important remark is that the elastic processes are not considered in Glauber model calculations due to very small contribution to the energy loss of nucleons. Therefore, only the inelastic ones contribute to the calculations. The probability of n nucleon-nucleon interactions between target A with A nucleons and projectile B with B nucleons is given by the binomial distribution

$$P(n, \vec{b}) = \binom{AB}{n} \left[\hat{T}_{AB}(\vec{b})\sigma_{inel}^{NN} \right]^n \left[1 - \hat{T}_{AB}(\vec{b})\sigma_{inel}^{NN} \right]^{AB-n}, \quad (2.4)$$

where the combinatorial term $\binom{AB}{n}$ expresses the number of combinations for finding n collisions out of AB possible nucleon-nucleon interactions, the second term gives the probability of having n collisions and the last term gives the probability of having $AB - n$ misses.

Finally, once we know the probability distribution, some useful quantities can be derived. The total probability of an interaction of the target A and the projectile B is

$$\frac{d^2\sigma_{inel}^{A+B}}{db^2} = \sum_{n=1}^{AB} P(n, \vec{b}) = 1 - \left[1 - \hat{T}_{AB}(\vec{b})\sigma_{inel}^{NN} \right]^{AB}. \quad (2.5)$$

Providing the colliding nuclei are not polarized, the impact parameter vector \vec{b} can be replaced by its scalar value as a distance of the centers of the nuclei. Using that, the total cross section is then

$$\sigma_{inel}^{A+B} = \int_0^\infty 2\pi b db \left\{ 1 - \left[1 - \hat{T}_{AB}(b)\sigma_{inel}^{NN} \right]^{AB} \right\}. \quad (2.6)$$

Particularly important are the following two quantities. The *total number of inelastic nucleon-nucleon collisions* N_{coll} can be found as

$$N_{coll}(b) = \sum_{n=1}^{AB} nP(n, b) = AB\hat{T}_{AB}(b)\sigma_{inel}^{NN}. \quad (2.7)$$

It can be seen, that the N_{coll} expressed in the equation (2.7) depends on the inelastic nucleon-nucleon cross section σ_{inel}^{NN} . The σ_{inel}^{NN} , however, grows with the collision energy. Therefore the number of inelastic nucleon-nucleon collisions is also dependent on the collision energy \sqrt{s} . The other important quantity is the *number of participants* N_{part} at given impact parameter b , which is given by relation

$$N_{part}(\vec{b}) = A \int \hat{T}_A(\vec{s}) \left\{ 1 - \left[1 - \hat{T}_B(\vec{s}-\vec{b})\sigma_{inel}^{NN} \right]^B \right\} d^2s + B \int \hat{T}_B(\vec{s}-\vec{b}) \left\{ 1 - \left[1 - \hat{T}_A(\vec{s})\sigma_{inel}^{NN} \right]^A \right\} d^2s. \quad (2.8)$$

The N_{part} energy dependence is much less significant, nonetheless, the total number of particles produced is scaled by N_{part} and so does particle multiplicity.

There are some differences between the Optical model and Monte Carlo approach which will be described in further section.

2.1.2 Glauber Monte Carlo

In the Monte Carlo approach for the Glauber computations the nucleons in the colliding nuclei are generated accordingly to the density distribution, e.g. (2.1), in the three-dimensional coordinate system. Then, the impact parameter is taken randomly from the interval $0 \leq b \leq 2R$ for each collision. Just like in the Optical model, the collision of the nuclei is treated as a set of independent binary nucleon-nucleon collisions while the nucleons travel along straight lines and the inelastic cross section is not affected by the collisions occurred before. The nucleon-nucleon collision occurs if the distance in the transverse plane between the nucleon from projectile and the nucleon from the target is below some limit. The limit is usually chosen as

$$d \leq \sqrt{\frac{\sigma_{inel}^{NN}}{\pi}}, \quad (2.9)$$

and thus is dependent on the energy of the collision, see Fig.2.3.

If sufficient number of collisions is simulated, the distributions of the quantities N_{coll} and N_{part} can be obtained and the mean values can be computed.

The considerable difference between the Monte Carlo and Optical model is the calculation of the integrals in the Optical approach, where the optical limit is used. This results into the fact that the incoming nucleons see the target as a smooth distribution of the nucleon density. Thus, the computations for the total cross section, N_{part} and N_{coll} give average values. However, in Monte Carlo approach there are different values of N_{part} and N_{coll} for each collision, because every collision is given by statistical procedure. Therefore, the Monte Carlo approach introduces fluctuations of N_{part} and N_{coll} , which is favourable for event-by-event modelling.

Particular example of the Monte Carlo Glauber event generator is presented in more detail in Chapter 5 and Chapter 8.

2.2 Centrality definition

Centrality can be generally defined as a percentage of the total nuclear cross section

$$c = \frac{1}{\sigma_{AB}} \int_0^b \frac{d\sigma}{db'} db'. \quad (2.10)$$

According to the percentage, *centrality classes* are defined (see Fig.2.2) once the total integral of the distribution is known. Alas, neither of N_{part} nor N_{coll} can be directly measured in the experiment, but a method for classification of the events with respect to the corresponding centrality classes is was developed. Usual distribution measured in the experiment (such as dN_{ent}/dN_{ch} , where N_{ch} is the number of charged hadrons) is used to map to the distribution obtained from the Glauber model via connecting the mean values for each centrality class from both measured and Glauber-obtained distributions. The important assumption for this method is that the impact parameter b is monotonic function of particle multiplicity. For this reason, one can expect high multiplicity of particles if b is small and low multiplicity if b is large.

Of course this is valid for the experimental estimation of the centrality. For this method the centrality definition in the Glauber model is needed as well. In a model, there are many ways how the centrality can be defined. Since the impact parameter is known, the centrality classes can be based on the percentage of the impact parameter distribution. However, this may cause inconsistencies in comparison with an experiment, since the two definitions do not fully correspond to each other. The usual way to overcome this and to make the centrality classes consistent with an experiment is to define centrality classes by the distribution of so called RDS¹, which is a combination of N_{part} and N_{coll} and is proportional to the particle multiplicity.

¹see Chapter 5 or Chapter 8 for more information

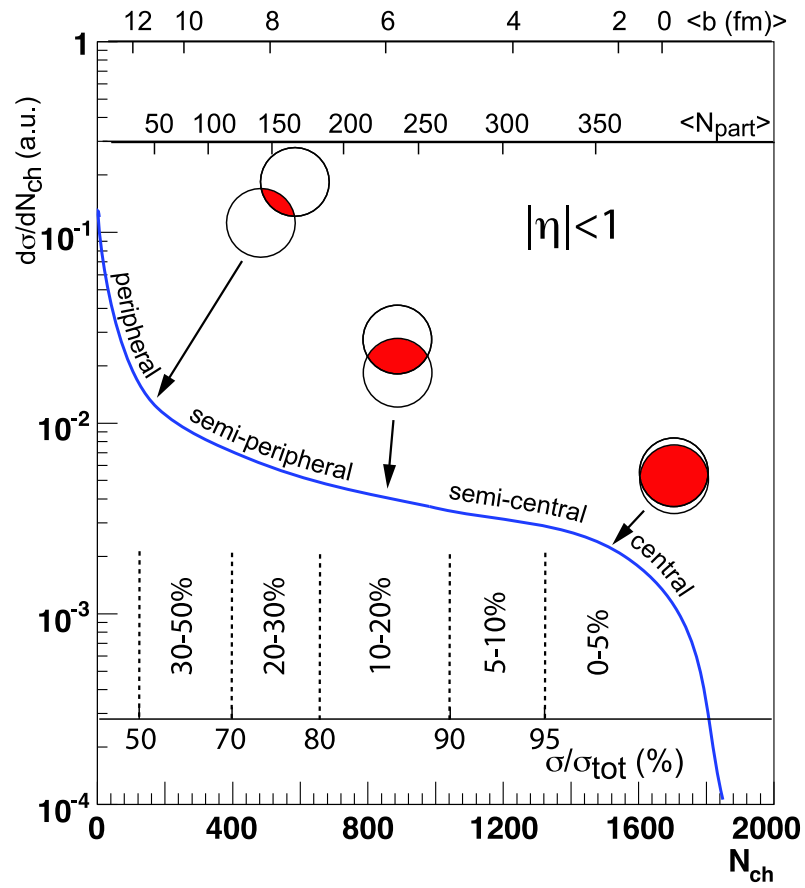


Fig. 2.2: An illustrative centrality distribution according to the mapping of final state observable N_{ch} and Glauber model computations. Figure taken from [9].

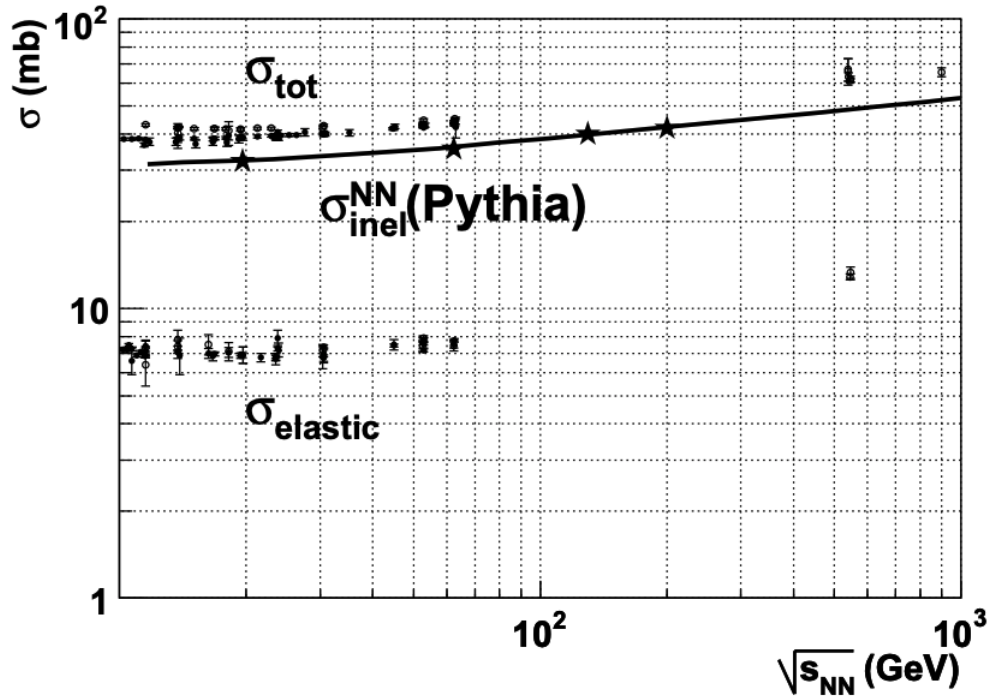


Fig. 2.3: The cross section σ collision energy $\sqrt{s_{NN}}$ dependence. The inelastic cross section σ_{inel}^{NN} (solid line) is presented as parametrized by Pythia. Also data for the total cross section σ_{tot} and the elastic cross section $\sigma_{elastic}$ are presented. Figure taken from [9].

Chapter 3

Expansion of the medium

After the collision of the nuclei occurred and after the creation of the quark-gluon plasma, the energy density is very high in the system. Moreover, once the nuclei collide, the strong pressure gradients from the center of the medium created to its boundary are present. As a consequence of the pressures, the medium starts to expand to the outer vacuum and starts to move collectively. Such collective movement is commonly called *flow*.

There is a connection between the particle transverse momentum spectra (integrated over the azimuthal angle) and radial expansion of the system, which is called *radial flow*, because the flow makes the spectrum flatter (see Fig.3.1). The more flow is present, the more the spectrum flattens, i.e. the more particles have higher values of transverse momentum. This fact will be important for this work later.

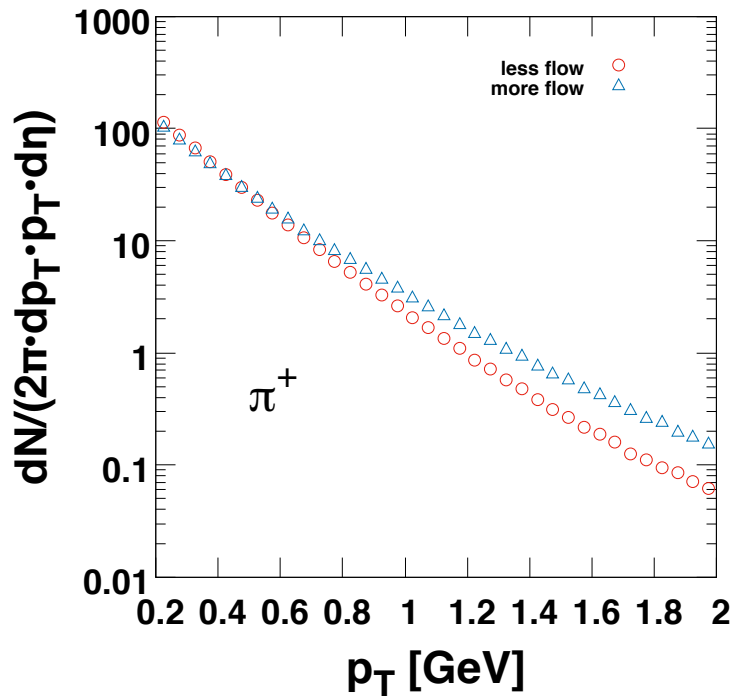


Fig. 3.1: Positive pion spectra from vHLE simulation. The red circles represent evolution, where less flow is present, whereas the blue triangles represent evolution with more flow.

3.1 Anisotropic flow

Firstly, let us deal with some nomenclature again. There are several distinctive planes which help to describe the collision. Probably the most significant one is called *reaction plane*. This plane is defined by the impact parameter and the beam direction. The angle Ψ_{RP} reflects the orientation of the two colliding nuclei with respect to the set of coordinates of the experiment x, y , i.e. plane perpendicular to the beam direction. Experimental estimation of the reaction plane is called *event plane*. The next one is *symmetry plane* which refers to the plane with respect to which the flow is measured. The symmetry plane is defined because the participants may fluctuate during the evolution of the expansion. Since the nucleons are randomly distributed in the nuclei, the actual symmetry plane of the collision can be tilted with respect to the reaction plane. This plane is called *participant plane* and takes into account the fluctuations of the position of nucleons.

In an experiment, anisotropies in hadron azimuthal distribution are observed. In fact, there are the p_T spectra with different flatness in different directions. That leads to the idea, that there is a different expansion in different directions. Using the defined planes (and corresponding angles) above, flow can be thought as a correlation of the azimuthal angle of emitted particles with respect to the symmetry plane. It basically shows the preferred direction of particle emission. In order to parametrize the azimuthal anisotropies as individual components of the real flow it is convenient to use a Fourier expansion of the distribution of hadrons in azimuthal angle

$$E \frac{d^3N}{dp^3} = \frac{d^2N}{2\pi p_T dp_T dy} \left\{ 1 + 2 \sum_{n=1}^{\infty} v_n(p_T) \cos[n(\varphi - \Psi_n)] \right\}, \quad (3.1)$$

where E is the particle energy, p the momentum, y refers to the rapidity, φ the azimuthal angle of emission w.r.t set coordinates and Ψ_n the symmetry plane angle. On the grounds of physical interpretation, these anisotropies are called anisotropic flow. The n -th Fourier coefficient can be expressed as

$$v_n = \langle \cos[n(\varphi - \Psi_n)] \rangle, \quad (3.2)$$

and these coefficients are called *flow coefficients*. The angular brackets in (3.2) denote averaging over all particles. In essence, the flow coefficients give the order of the harmonic flow. For $n = 1$ it is a case of *directed flow* and it can be interpreted as dipole deformation of hadron distribution, which is not azimuthally symmetric. The second coefficient, however, is crucial for the study of anisotropic expansion of the medium. It is called *elliptic flow* or v_2 . In Fig.3.2, there is an illustration of the fireball expansion.

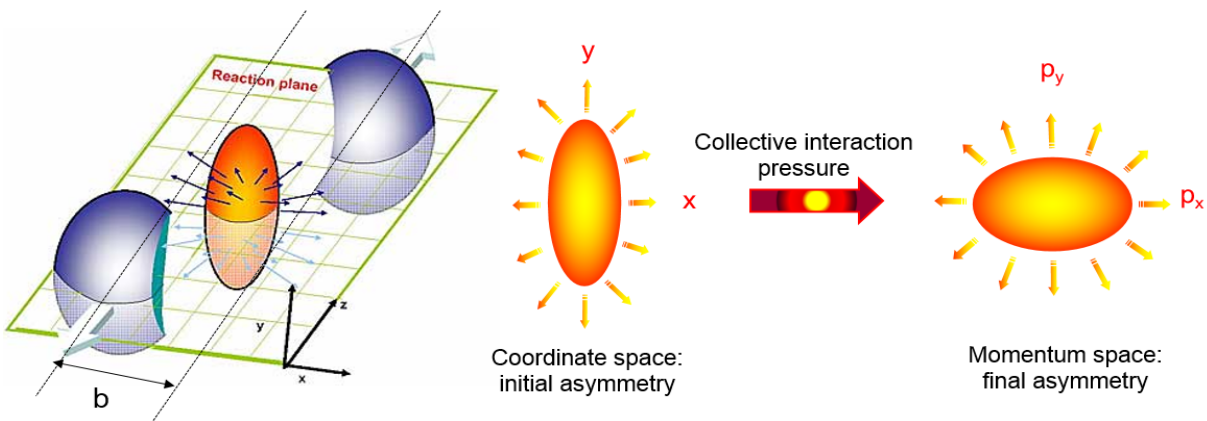


Fig. 3.2: An illustration of the development of a fireball. The initial spatial anisotropy is transformed into the final momentum anisotropy. Figure taken from [10].

As discussed in the previous chapter, the nuclei do not always (in fact in most of the events) collide head-on. Hence, the medium, usually referred to as *fireball*, is produced in so called *almond shape* and thus has non-zero second-order spatial anisotropy ϵ_x ,

$$\epsilon_x = \frac{\langle y^2 - x^2 \rangle}{\langle y^2 + x^2 \rangle}. \quad (3.3)$$

The angular brackets denote averaging over the transversal plane. The pressure gradients in various directions in the created fireball have then different magnitude. The gradients are smaller in the direction, in which the fireball extends to a longer size. The initial anisotropy is then due to different pressure gradients transferred to the final particle production anisotropy, which is possible only due to the presence of the strongly interacting medium. As a consequence of the imbalance of the pressures, the elliptic flow arise and the initial spatial anisotropy decreases. Then again, there is also an anisotropy in the momentum space ϵ_p ,

$$\epsilon_p = \frac{\langle T_{yy} - T_{xx} \rangle}{\langle T_{yy} + T_{xx} \rangle}, \quad (3.4)$$

where T_{xx} and T_{yy} refer to the diagonal components of the energy momentum tensor of the medium. As the spatial anisotropy vanishes, the momentum anisotropy grows in the perpendicular direction.

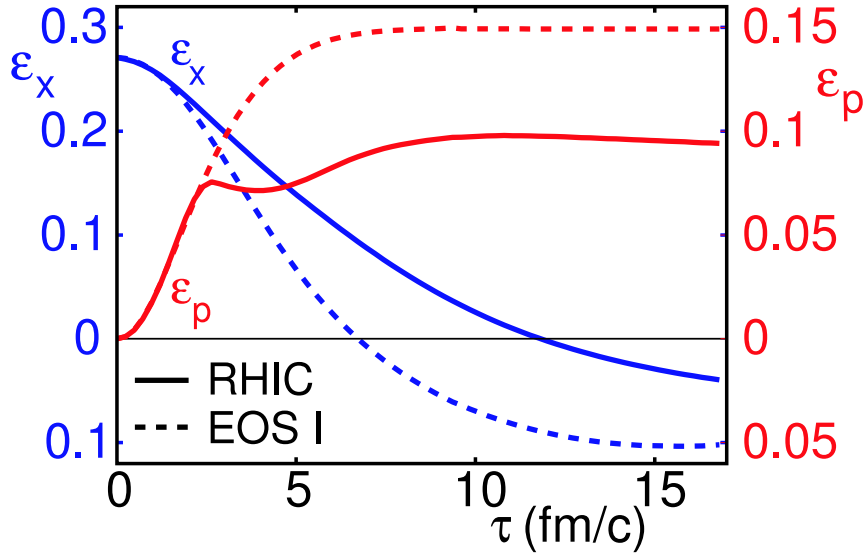


Fig. 3.3: An example of the time dependence of both spatial and momentum anisotropies. The shape of the evolution depends on EOS. Figure taken from [11].

Together with the evolution of spatial anisotropy and formation of the elliptic flow, the momentum anisotropy can provide information about the equation of state of the strongly interacting matter as it carries the information about the energy-momentum development during the evolution of the medium. Though ϵ_p cannot be directly observed in the experiment, its dependence on equation of state is reflected in the elliptic flow, which can be also parametrized as

$$v_2 = \frac{\langle p_y^2 - p_x^2 \rangle}{\langle p_y^2 + p_x^2 \rangle}, \quad (3.5)$$

where p_x , p_y are momenta of hadrons produced in corresponding directions. The elliptic flow is then a consequence of the momentum anisotropy.

The final value of the flow is sensitive to *initial conditions* before the evolution (i.e. the

distribution of initial energy density in the transverse plane) and to *transport coefficients* (shear viscosity,...). Such quantities are important for hydrodynamical description of the evolution of the medium.

3.1.1 Elliptic flow centrality dependence

Elliptic flow shows strong centrality dependence. As seen in Fig.3.4, for central collisions, which corresponds to centrality percentile around 0% (as described in previous chapter), the elliptic flow coefficient becomes small. In fact, the elliptic flow is not just a consequence of the initial almond-shaped fireball, but also the effect of fluctuations of positions of the nucleons inside the nuclei. This can be seen (Fig.3.4) at centrality close to zero. If the elliptic flow was caused only by the "almond" shape of the fireball, the values of v_2 would decrease to zero. The values of v_2 , however, are not zero, since the fluctuations are present. As the centrality rises, the values of elliptic flow rise as well up to the point of saturation and for very peripheral collisions the values start to drop down again. For central collisions, the small values of v_2 are a result of the fact that there is still very small initial spatial anisotropy due to fluctuations of the nucleons, which is then transformed into the momentum anisotropy. On the other hand, for the peripheral collisions it is the effect of the system not being long-lived enough to transfer the initial anisotropy completely. However, the effect of jets can also be seen in the figure, for $p_T = 3 - 6$ GeV, which are less suppressed in the shorter direction of the fireball.

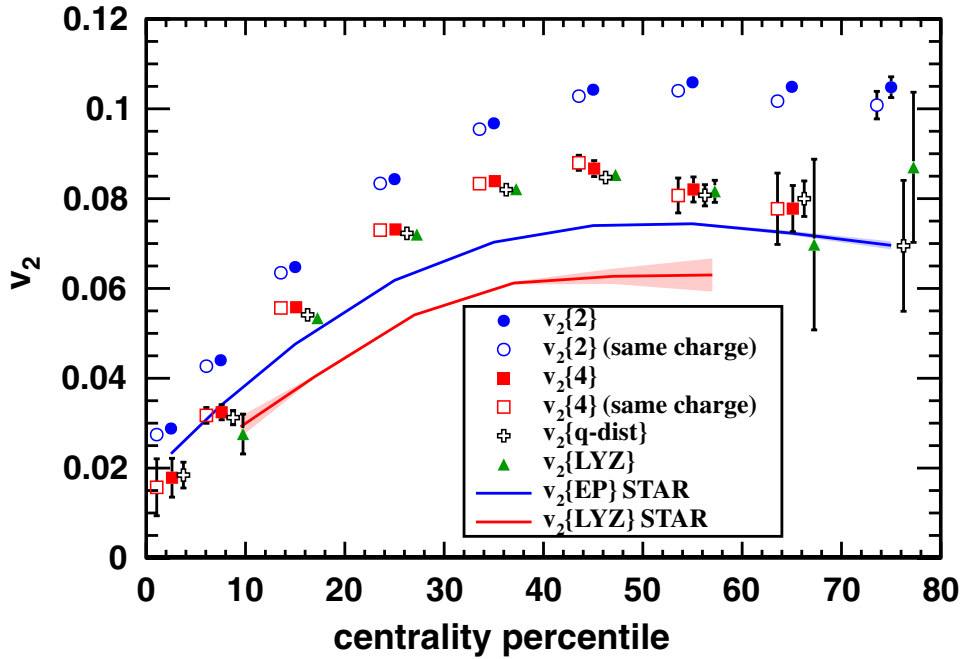


Fig. 3.4: Integrated elliptic flow (over p_T) as a function of the centrality. Figure taken from [12].

3.1.2 Elliptic flow momentum dependence

In Fig.3.5, typical transverse momentum dependence of elliptic flow is shown. As one could expect, the value of the v_2 coefficient rises as p_T of the particles gets higher. If p_T is zero, then elliptic flow has to be zero as well. This is a result of symmetry - if there is no transverse direction, the flow cannot be even defined. For low and intermediate transverse momentum it is the case of the bulk part of the particle spectrum, i.e. the soft part. This corresponds to the effect of the evolution of the fireball. Low p_T particles are produced from thermalized fireball. For higher p_T the particles are produced from regions of homogeneity which are smaller than the fireball and spatially deformed.

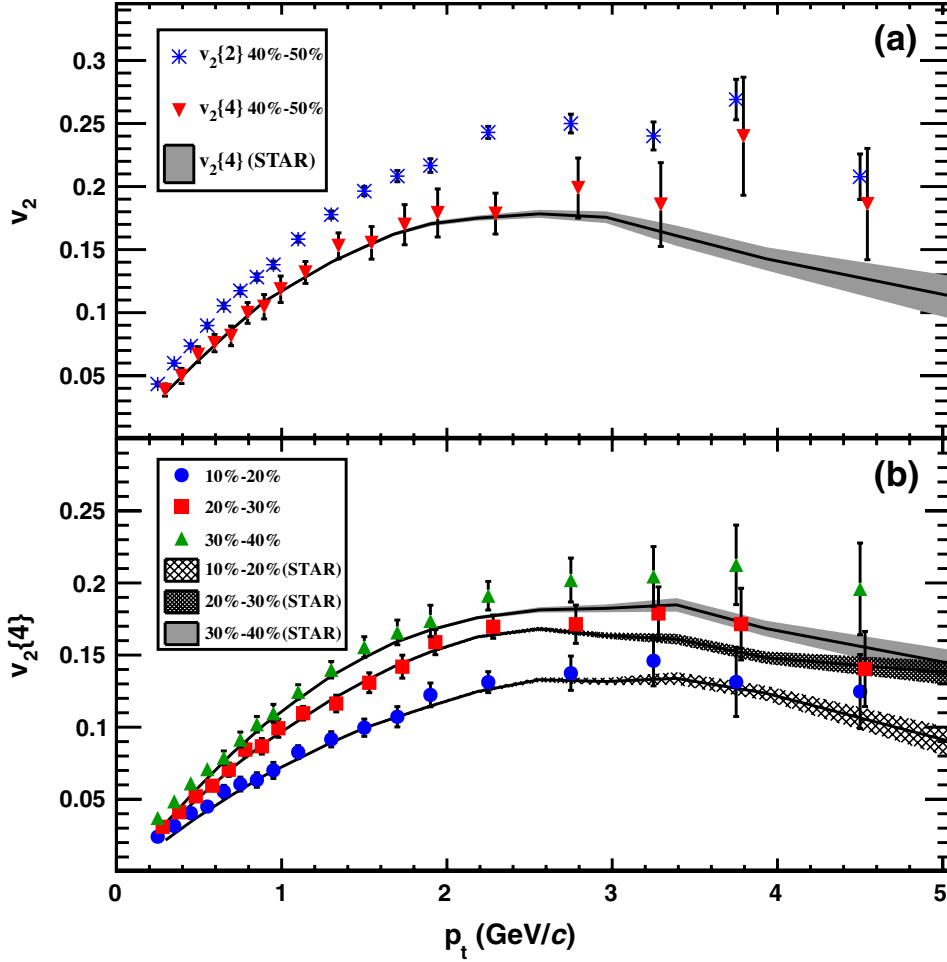


Fig. 3.5: v_2 as a function of p_T from ALICE measurement. Figure taken from [12].

3.1.3 Measurement of flow

There are several methods for computing the elliptic flow from the data. Here the two most commonly used are discussed, i.e. the event plane method and the cumulant method.

3.1.3.1 Event plane method

The first method, which will be discussed is the event plane method. As mentioned in section 3.1, the event plane is the experimental approximation of the reaction plane, which is the plane defined by impact parameter and the beam direction. For this method the *event flow vector* Q_n and the *event plane angle* Ψ_n are defined as

$$Q_n \cos n\Psi_n = Q_n^x = \sum_i w_i \cos n\varphi_i \quad (3.6)$$

$$Q_n \sin n\Psi_n = Q_n^y = \sum_i w_i \sin n\varphi_i \quad (3.7)$$

$$\Psi_n = \frac{1}{n} \arctan\left(\frac{Q_n^y}{Q_n^x}\right), \quad \text{where } \Psi_n \in \left[-\frac{\pi}{n}, \frac{\pi}{n}\right). \quad (3.8)$$

The summation in (3.6) and (3.7) runs over all particles. The n denotes the order of the harmonics, φ_i refers to the azimuthal angle of the i -th particle and w_i is a weight for the i -th particle, which is usually chosen as particle transverse momentum p_T .

As mentioned above in (3.2), the observed elliptic flow can be expressed as

$$v_2^{obs} = \langle \cos[2(\varphi - \Psi_n)] \rangle, \quad (3.9)$$

where the averaging is over all particles. In order to avoid self-correlation effects, the particles used for computing the v_2 are excluded from the computation of the flow vectors. Since the event plane may fluctuate due to the finite number of particles, the correction to the v_2^{obs} has to be introduced. The event plane resolution is defined as a correlation of the event plane with the reaction plane

$$R_n = \langle \cos[2(\Psi_n - \Psi_{RP})] \rangle, \quad (3.10)$$

where here the angular brackets refer to averaging over all events. The observed elliptic flow has to be divided by the resolution R_n in order to obtain the corrected elliptic flow as

$$v_2 = \frac{v_2^{obs}}{\langle \cos[2(\Psi_n - \Psi_{RP})] \rangle}. \quad (3.11)$$

Since the reaction plane angle Ψ_{RP} cannot be obtained directly, the denominator in (3.11) can be rewritten by the correlation of two subset groups of particles, called sub-events A and B as

$$\langle \cos[2(\Psi_n - \Psi_{RP})] \rangle = C \sqrt{\langle \cos[2(\Psi_n^A - \Psi_n^B)] \rangle}, \quad (3.12)$$

where the factor C can be calculated from the multiplicity dependence of the resolution.

3.1.3.2 Cumulant method

As previously explained, the symmetry plane cannot be measured exactly and the estimation of the event plane carries a certain uncertainty. Computing flow coefficient from such estimation can provide quite imprecise results. Instead of the estimation of the event plane, are often measured particle correlations. From the definition of the flow coefficient (where the brackets refer to averaging over the particles):

$$v_n = \langle \cos[n(\varphi - \Psi_n)] \rangle = \langle e^{in(\varphi - \Psi_n)} \rangle. \quad (3.13)$$

Now, for the two particle correlation function we write the two-particle *cumulants* of the v_n distribution in the form

$$\begin{aligned} c_n\{2\} &= \langle \langle e^{in(\varphi_1 - \varphi_2)} \rangle \rangle = \langle \langle e^{in(\varphi_1 - \Psi_n - (\varphi_2 - \Psi_n))} \rangle \rangle \\ &= \langle \langle e^{in(\varphi_1 - \Psi_n)} \rangle \langle e^{-in(\varphi_2 - \Psi_n)} \rangle + \delta_2 \rangle = \langle v_n^2 + \delta_2 \rangle, \end{aligned} \quad (3.14)$$

where the second brackets refer to averaging over all events. For four-particle cumulants

$$\begin{aligned} c_n\{4\} &= \langle \langle e^{in(\varphi_1 + \varphi_2 - \varphi_3 - \varphi_4)} \rangle \rangle - 2 \langle \langle e^{in(\varphi_1 - \varphi_2)} \rangle \rangle^2 \\ &= \langle v_n^2 + \delta_4 + 4v_n^2\delta_2 + 2\delta_2^2 \rangle - 2 \langle v_n^2 + \delta_2 \rangle^2 = \langle -v_n^4 + \delta_4 \rangle. \end{aligned} \quad (3.15)$$

The delta symbols in cumulant expressions are called *non-flow*. Non-flow effects, such as jets, resonance decays or particles not correlated to the symmetry plane tend to increase the flow signal. However, it is possible to get rid of the non-flow effects of higher order by computing higher order cumulants as seen when comparing (3.14) and (3.15).

Chapter 4

Hydrodynamic modelling

For the description of the evolution of the quark-gluon plasma, an approach which treats the QGP hydrodynamically was proved to be useful. The collective behaviour of the medium is well described by relativistic equations of fluid dynamics. Signs of collectivity such as radial and elliptic flow are sensitive to the equation of state which is a crucial ingredient of hydrodynamic models. Let us introduce basic hydrodynamic equations and principles of hydrodynamic modeling.

Generally, basic assumption for fluid computations are, that the system is composed of many volume elements which contain large number of particles and every volume element has a different density and collective velocity. Mean free path, i.e. the distance without any interaction, of the particles is much smaller than macroscopic scale of the whole system. The state of the system is defined by velocity field and some other two thermodynamic variables.

4.1 Relativistic ideal fluid dynamics

Unlike in computations for non-relativistic ideal fluid, the mass and the number of particles is not conserved in the relativistic case, since new baryon-antibaryon pairs can be created (conserving baryon number), moreover, non-strange mesons can be created freely (since there is no meson charge). Then again, strangeness must be conserved and strange mesons are also produced in pairs (but this could be pairs of meson-baryon, e.g. kaon and Lambda). On the other hand, the conserved quantities are energy, momentum and charge. The conservation of local energy-momentum can be written as

$$\partial_\nu T^{\mu\nu} = 0. \quad (4.1)$$

In this expression, the energy-momentum tensor corresponds to the local flow of energy and momentum through a surface. Should $d\mathbf{p}=(dE, dp_x, dp_y, dp_z)$ be differential 4-momentum and $d\mathbf{x}=(dt, dx, dy, dz)$ differential space-time 4-vector, the components of the energy-momentum tensor can be written for $\mu = \nu = 0$ as

$$T^{00} = \frac{dE}{dx dy dz} = \frac{dE}{dV} = \varepsilon \quad (4.2)$$

where ε denotes the energy density, $c = 1$, and for $i = j$

$$\begin{aligned} T^{11} &= \frac{dp_x}{dt dy dz} \\ T^{22} &= \frac{dp_y}{dt dx dz} \\ T^{33} &= \frac{dp_z}{dt dx dy}. \end{aligned} \quad (4.3)$$

Since the common part of energy-momentum tensor components $\frac{dp}{dt}$ is an expression for a force and this force is exerted on a differential surface, the Pascal law can be formulated

$$T^{ij} = p \cdot \delta^{ij}, \quad (4.4)$$

where p denotes pressure. Using this, the energy-momentum tensor in the rest frame can be expressed as

$$T = \begin{pmatrix} \varepsilon & 0 & 0 & 0 \\ 0 & p & 0 & 0 \\ 0 & 0 & p & 0 \\ 0 & 0 & 0 & p \end{pmatrix}. \quad (4.5)$$

In order to obtain an expression for $T^{\mu\nu}$ in any moving frame, not only the rest frame, the Lorentz transformation has to be applied on the tensor

$$T^{\mu\nu} = \Lambda_{\mu}^{\rho} \Lambda_{\nu}^{\sigma} T_{RF}^{\rho\sigma}, \quad (4.6)$$

where $\Lambda^{\mu\nu}$ is a Lorentz transformation and label RF refers to the rest frame. Using the fact that an expression for 4-velocity can be obtained from the Lorentz transformation as $u^{\mu} = \Lambda_0^{\mu}$ and the term $\Lambda_i^{\rho} \Lambda_i^{\sigma} = u^{\rho} u^{\sigma} - g^{\rho\sigma}$, where the summation over i is assumed ($g^{\mu\nu}$ is a metric tensor) the energy-momentum tensor can be rewritten into the well-known form

$$T^{\mu\nu} = (\varepsilon + p)u^{\mu}u^{\nu} - p \cdot g^{\mu\nu}. \quad (4.7)$$

The equations of relativistic hydrodynamics are the equation of local energy-momentum conservation (4.1) where $T^{\mu\nu}$ now has the form (4.15). However, two more equations are needed to have a complete set of equations. Because mass is not conserved in the relativistic case, other quantity has to be chosen. Fortunately, the charge is conserved even in relativistic case, so the first of the equations is

$$\partial_{\mu} N^{\mu} = 0 \quad \text{where } N^{\mu} = n \cdot u^{\mu} \quad (4.8)$$

and n is charge density. The other equation needed is the equation of state, $p = p(\varepsilon, n)$, n here denotes baryon density (but could also be strangeness, in which case we would have another charge flow and another conservation equation).

For practical purposes, the hydrodynamic equation can be projected into the directions along u^{μ} and into the direction perpendicular to u^{μ} by defining a projector

$$\Delta_{\mu\nu} = g^{\mu\nu} - u^{\mu}u^{\nu} \quad \text{so that } \Delta^{\mu\nu}u_{\nu} = 0. \quad (4.9)$$

The equations can be then rewritten into the forms, which are analogous to continuity equation

$$u_{\mu}\partial_{\nu}T^{\mu\nu} = u^{\nu}\partial_{\nu}\varepsilon + (\varepsilon + p)\partial_{\nu}u^{\nu} = 0 \quad (4.10)$$

and to Euler equations

$$\Delta_{\mu}^{\alpha}\partial_{\nu}T^{\mu\nu} = (\varepsilon + p)u^{\nu}\partial_{\nu}u^{\alpha} - \Delta^{\alpha\nu}\partial_{\nu}p = 0. \quad (4.11)$$

4.2 Relativistic viscous hydrodynamics

Alas, the real fluid is not ideal and thus some modifications to the fluid equations have to be done. A real fluid has, compared to the ideal one, more parameters to be considered.

Let us begin by introduction of classical non-relativistic Navier-Stokes equations, which describe viscous fluid

$$\rho(\partial_i v_i + v_k \partial_k v_i) = -\partial_i p + \eta \Delta v_i + \left(\zeta + \frac{\eta}{3}\right) \partial_i (\partial_k v_k). \quad (4.12)$$

Here, new parameters appear and correspond to two *viscosity* types - η denotes *shear viscosity* and ζ *bulk viscosity*. The first type, *shear viscosity*, quantifies the resistance or unwillingness to fast deformation. In a microscopic scale, it can also be thought of as momentum transfer between thin fluid layers. The other type of viscosity, *bulk viscosity*, quantifies the resistance of the bulk to its fast expansion or compression. Both of these viscosities remain valid even for relativistic fluids and play an important role in the evolution of such fluids. Let us now derive hydrodynamic equations for relativistic viscous fluids.

The hydrodynamic equations for the viscous case has the same general form as for the ideal fluid, i.e. (4.1). Nevertheless, since the fluid is not ideal anymore, the energy-momentum tensor and also charge have to contain additional terms

$$\begin{aligned} T^{\mu\nu} &= (\varepsilon + p)u^\mu u^\nu - p \cdot g^{\mu\nu} + W^\mu u^\nu + W^\nu u^\mu + \Pi^{\mu\nu} \\ N^\mu &= nu^\mu + v^\mu, \end{aligned} \quad (4.13)$$

where W^μ is the energy flow in the local rest frame and $\Pi^{\mu\nu}$ is yet to be determined in following steps. The prescription of the flow velocity u^μ can be chosen in so called *Landau frame* as

$$u^\mu = \frac{T^{\mu\nu} u_\nu}{\sqrt{u_\alpha T^{\alpha\beta} T_{\beta\gamma} u^\gamma}}, \quad (4.14)$$

so u^μ is the energy flow velocity and thus as a consequence $W^\mu = 0$. The energy-momentum tensor then takes the form

$$T^{\mu\nu} = (\varepsilon + p)u^\mu u^\nu - p \cdot g^{\mu\nu} + \Pi^{\mu\nu}. \quad (4.15)$$

In simplicity, the form of $\Pi^{\mu\nu}$ shall be determined next. Because of the presence of viscosity, the entropy should increase

$$\partial_\mu (s u^\mu) > 0, \quad (4.16)$$

where s is the entropy density. Using equations (4.10) together with (4.15) one obtains

$$T \partial_\mu (s u^\mu) = \Pi^{\mu\nu} \partial_\mu u_\nu. \quad (4.17)$$

Here T stands for the thermodynamic temperature. The notation $\partial_{\langle\mu} u_{\nu\rangle} = \frac{1}{2}(\partial_\mu u_\nu + \partial_\nu u_\mu)$ will be used onward. Also, the right hand side term $\Pi^{\mu\nu} \partial_\mu u_\nu$ is symmetric in the μ and ν indices. By separating the $\Pi^{\mu\nu}$ into traceless and non-traceless parts one obtains

$$\Pi^{\mu\nu} = \pi^{\mu\nu} - \Delta^{\mu\nu} \Pi, \text{ where } \text{Tr}(\pi) = 0, \quad (4.18)$$

and $\Delta^{\mu\nu}$ corresponds to the projector defined in (4.9). For the derivative term $\partial_{\langle\mu} u_{\nu\rangle}$ one can introduce

$$\partial_{\langle\mu} u_{\nu\rangle} = \left[\frac{1}{2}(\Delta_\mu^\alpha \Delta_\nu^\beta + \Delta_\mu^\beta \Delta_\nu^\alpha) - \frac{1}{3} \Delta_{\mu\nu} \Delta^{\alpha\beta} \right] \partial_\alpha u_\beta, \quad (4.19)$$

which is also traceless. Using these relations, the right hand side of (4.17) can be rewritten as

$$T \partial_\mu (s u^\mu) = \Pi^{\mu\nu} \partial_\mu u_\nu = \pi^{\mu\nu} \partial_{\langle\mu} u_{\nu\rangle} - \Pi \partial^\beta u_\beta. \quad (4.20)$$

Since the entropy cannot decrease, the condition (4.16) can be fulfilled only if

$$\pi^{\mu\nu} = \eta \partial^{\langle\mu} u^{\nu\rangle} \text{ and } \Pi = -\zeta \partial_\mu u^\mu, \quad (4.21)$$

where $\eta > 0$ is identified with shear viscosity and $\zeta > 0$ bulk viscosity. The $\pi^{\mu\nu}$ is then called *shear stress tensor* and Π is *bulk pressure*. At last, we arrive at relativistic Navier-Stokes equations projected to the direction parallel to u^μ and the direction perpendicular to u^μ respectively

$$D\varepsilon + (\varepsilon + p - \zeta\nabla_\alpha u^\alpha)\partial_\mu u^\mu - 2\eta\partial^{(\alpha}u^{\beta)}\partial_{(\alpha}u_{\beta)} = 0 \quad (4.22)$$

and

$$(\varepsilon + p - \zeta\partial_\alpha u^\alpha)Du^\mu - \partial^\mu(p - \zeta\nabla_\alpha u^\alpha) + 2\Delta_\alpha^\mu\partial_\beta(\eta\partial^{(\alpha}u^{\beta)}) = 0. \quad (4.23)$$

Here the notation $D \equiv u^\mu\partial_\mu$ is used. Both of these equations (4.22) and (4.23) can be used in a numerical algorithm and after the initial state, boundary conditions and the equation of state are provided, the equations can be solved.

However, these equations have some difficulties. The spectral analysis of relativistic Navier-Stokes equations shows, that the equations are acausal, which causes instabilities in the computations. Therefore, in order to obtain a causal theory, the equations have to be modified and relaxation parameters need to be introduced. The left hand side of the equations (4.21) have then additional terms

$$\begin{aligned} \pi^{\mu\nu} = \eta\partial^{(\mu}u^{\nu)} &\implies \tau_\pi D\pi^{\mu\nu} + \pi^{\mu\nu} = \eta\partial^{(\mu}u^{\nu)} = \pi_{NS} \\ \Pi = -\zeta\partial_\mu u^\mu &\implies \tau_\Pi D\Pi + \Pi = -\zeta\partial_\mu u^\mu = \Pi_{NS}. \end{aligned} \quad (4.24)$$

The parameters $\tau_\pi = \tau_\pi(\eta)$ and $\tau_\Pi = \tau_\Pi(\zeta)$ are called relaxation times and are linear functions of the corresponding viscosity. Recalling the condition (4.16) still needs to be satisfied, an analogous procedure as for derivation of relativistic Navier-Stokes equations leads to the commonly used form of relativistic viscous hydrodynamic equations

$$\begin{aligned} D\pi^{(\mu\nu)} &= -\frac{\pi^{\mu\nu} - \pi_{NS}^{\mu\nu}}{\tau_\pi} - \frac{4}{3}\pi^{\mu\nu}\partial_\alpha u^\alpha \\ D\Pi &= -\frac{\Pi - \Pi_{NS}}{\tau_\Pi} - \frac{4}{3}\Pi\partial_\alpha u^\alpha. \end{aligned} \quad (4.25)$$

The relaxation time $\tau_\pi = \frac{k\eta}{sT}$, where k has typical values in interval from 3 to 5. These equations are now causal and thus provide more stability to the numerical computations.

4.3 Basic principles of hydrodynamic numerical methods

The most common approach of hydrodynamic numerical computations is based on the evolution of the fluid via (4.25) and (4.1) type of equations, which were derived from the principle of energy-momentum conservation, as can be seen in the both of the previous sections. Once an initial state energy or entropy distribution is provided, it is transformed into the fluid. The fluid created is then divided into many fluid cells, each of which contains its total energy-momentum T^{0i} . While the total energy-momentum in whole system is conserved, the energy and momentum is transported between the cells by fluxes T^{ij} . Subsequently, every cell has also its own velocity, which is key for viscosity introduction, as mentioned in previous section.

In addition to the hydrodynamic equations, there are several inputs needed for the computation. One of them is an aforementioned initial state with initial conditions. In other words, the initial energy-momentum distribution (i.e. energy-momentum tensor) has to be provided. The charge distribution has to be given as well. As such initial state simulators, a Glauber Monte Carlo algorithms can be used among many others. The profile of initial conditions affects the hydrodynamic evolution substantially, because as various initial state generators provide different initial conditions (as can be seen in Fig.4.1), the fluid created has the same properties but

evolves differently due to different initial states. The other important inputs, which in fact we want to study, are the equation of state $p = p(\varepsilon, n)$, which connects the energy density and pressure, and the transport coefficients ζ, η . The EOS and the viscosities can be studied from final observables investigation. The observable obtained from the simulations, where the equation of state and transport coefficients are known, can be compared to the observables measured by an experiment and therefore important data can be retrieved.

As the initial conditions are needed before the hydrodynamic evolution, the final conditions are needed after it. The hydrodynamic evolution stops at the point when the critical energy density is reached and the remainder of the fireball evolution is usually simulated by a transport code. After the hydrodynamic evolution stops, a hypersurface Σ of constant temperature or constant energy density is formed. At this hypersurface the fluid decouples and the momentum distribution is finally set for the transport simulations. From the kinetic theory of matter, the form of the particle momentum distribution can be obtained by means of well known Cooper-Frye formula

$$p^0 \frac{d^3 N}{d p^3} = \int_{\Sigma} d\Sigma_{\mu} p^{\mu} f(x, p). \quad (4.26)$$

Nowadays the *particlization* process is used. After this process, the momentum distribution can still change. Particles are created from the fluid and exist in a form of *hadron resonance gas*. Each hadron species is distributed in one corresponding hadron gas. The distribution of the i -th species in thermal and chemical equilibrium (or close to it) has usually the form of

$$f_i(x, p) = f_{i,eq} = \frac{g_i}{(2\pi)^3} \frac{1}{\exp\left(\frac{p^{\nu} u_{\nu} - \mu_i(x)}{T(x)} \pm 1\right)}, \quad (4.27)$$

where g_i is the degeneracy factor, $\mu_i(x)$ local chemical potential and $T(x)$ is local temperature. When viscous hydrodynamic approach is used, the usual modification of the distribution can be done as

$$f_i = f_{i,eq} + f_{i,eq} (1 \pm f_{i,eq}) \frac{p^{\mu} p^{\nu} \pi_{\mu\nu}}{2(\varepsilon + p)T^2}. \quad (4.28)$$

These hadrons are then rescattered via a hadronic cascade *afterburner* code (e.g. UrQMD) in order to get final distribution and for even better modelling.

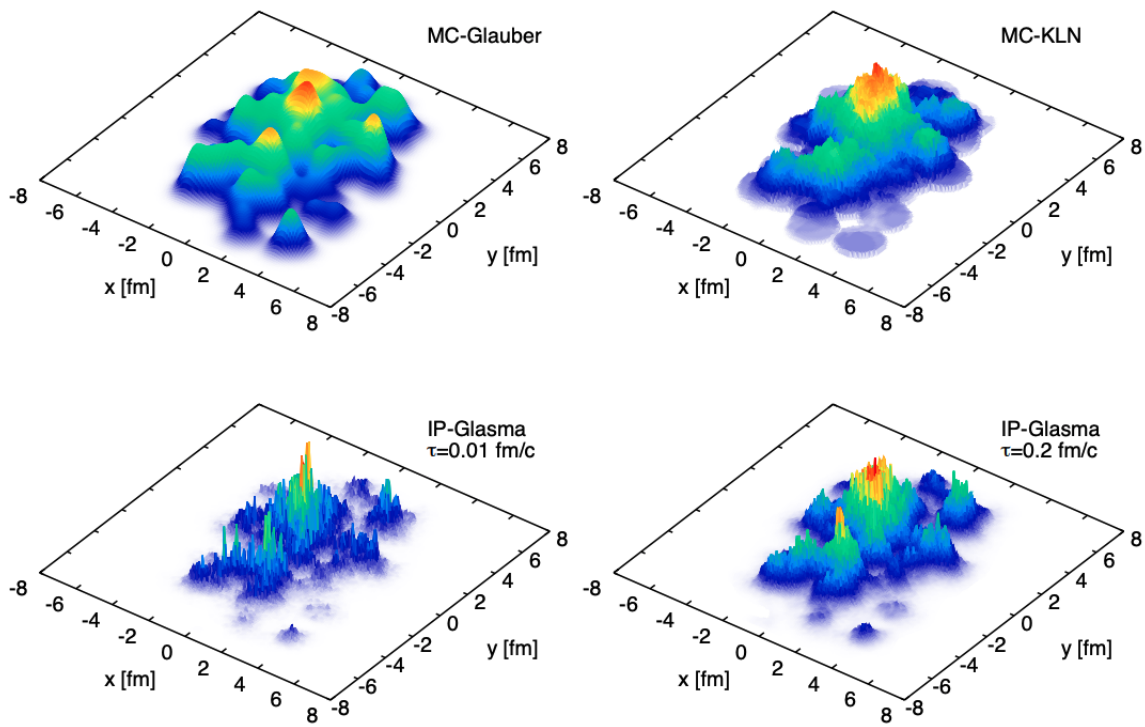


Fig. 4.1: Various initial energy distribution for the same configuration of nucleons and impact parameter $b = 4$ fm as outputs of different generators. From top left: MC-Glauber, MC-KLN model. Bottom: IP-Glasma for two settings of relaxation time. Figure taken from [13].

Chapter 5

Hybrid vHLE package

For modelling heavy-ion collisions so called *hybrid model* concept is commonly used. Essentially, it is three step procedure of generating initial conditions (i.e. initial energy distribution), then the initial state is transformed into a fluid, which is evolved by hydrodynamic code and the last part is creation of particles out of the fluid, particlization, and their rescattering. The hybrid vHLE package does contain the hydrodynamic code, but the initial conditions generator and a final transport model must be provided.

5.1 Initial conditions

Basically, the initial state generators simulate the initial collision of the primary nuclei. The collision takes place according to the physical approach of given model. Moreover, only one collision must be generated at a time since the model works in event-by-event mode. The output of the initial state generator is usually an energy density profile or entropy profile. As stated above, the vHLE package does not contain such initial conditions generator, so some of the available generators have to be used, such as UrQMD [14], Glissando [15], [16], [17] or Trento [18]. In this part let us focus on the Glissando generator, because in this work we shall explore the Glauber Monte Carlo initial state models.

5.1.1 Glissando

The name Glissando stands for *GLauber Initial-State Simulation AND mOre*. As the name suggests, Glissando is a Glauber Monte Carlo simulator of the nucleus-nucleus collisions. The principle of the simulation can be summarized into the following steps.

First, the positions of nucleons in the colliding nuclei are generated according to the Woods-Saxon nuclear density. In fact, only the centers of nucleons are generated by the Woods-Saxon density, however, since the nucleons are not point-like objects, a minimal distance between each two nucleons has to be kept in order to reproduce short-range repulsion of nuclear forces. For maintaining such spacing, parameters of the distribution have to be chosen in a way to reproduce density distribution obtained by electron-nucleus scattering combined with Gaussian nucleon charge profile. Usual scale for the distance between the nucleons is a fraction of femtometer. The distancing of nucleons, together with a shift of the generated coordinates to the center-of-mass frame of the nucleus, cause change of the shape of the density distribution and must be taken into account.

In order to collide the generated nuclei at certain centrality, the impact parameter has to be introduced. For systemization of the collisions, the centrality classes can be chosen either by means of the impact parameter or relative deposited strength, which will be discussed later in this section. The condition for the collision to take place is that the distance between the center

of one nucleon from one nucleus to the center of another nucleus from the other nucleus has to be less than *wounding distance*

$$r_0 = \sqrt{\frac{\sigma_w}{\pi}}, \quad (5.1)$$

where σ_w is the nucleon-nucleon inelastic cross section at given collision energy. From this it can be seen, that for various collision energies, the wounding distance has different value, as the cross section grows as a function of collision energy.

During the collision a certain amount of energy is deposited at the area of a source, which is meant as individual deposition of the transverse energy at a definitive position in the transverse plane. This energy deposited might vary from source to source and in order to be able to observe these fluctuations the *relative deposited strength* (RDS) is introduced. This quantity is defined as

$$RDS = (1 - \alpha) \frac{N_{part}}{2} + \alpha N_{coll}, \quad (5.2)$$

where α is an energy-dependent parameter, N_{part} is the number of participants and N_{coll} is the number of binary collisions. The RDS is proportional to the particle multiplicity, in fact, the first term corresponds to the soft part of the particle spectrum and the other term to the hard part.

Glissando includes several settings for the modelling of centrality selection - wounded nucleon model, binary collisions model and mixed model. For the wounded nucleon model the RDS has the value of one half of the number of the wounded nucleons, therefore corresponds to $\alpha = 0$ in (5.2). In binary collisions model the RDS has the same value as the number of binary collisions, this coincides with $\alpha = 1$. Nevertheless, best results are obtained by mixed model which combines wounded nucleons model with binary collisions. Here, the value of the α parameter lies in the interval (0,1) and has to be determined for given collision energy.

As an output, Glissando provides the positions of the sources in the transversal plane and the corresponding RDS value. The sources then have to be transformed into the fluid in order to execute hydrodynamical computations.

For the description of Glissando in more detail see [15] and [16].

5.2 vHLL

The vHLL code is the main part of the package, which contains the 3+1 dimensional viscous hydrodynamic computations. But before the hydrodynamic computations can begin, the initial state needs to be transformed into a viscous fluid. Basically, the energy-momentum tensor created and divided into a spatial grid. For each cell of the grid the energy-momentum tensor is filled and after all cells are prepared, the grid is smeared in order to get smoother distribution. Then the fluid can be evolved by the hydrodynamic equations until the critical energy density is reached, i.e. until freeze-out.

For Glissando one more procedure has to be done. Since the output from Glissando is only in transverse plane (thus in 2D), the energy distribution has to be extended into the rapidity. This is done as suggested in [19], [20]. The whole procedure is described in more detail in Chapter 8.

The name vHLL is a shortcut for *viscous Harten-Lax-van Leer-Einfeldt*. The HLL is a common method for solving Riemann problem, which is a type of problem naturally appearing in the solution of Euler-like equations, thus in hydrodynamics. The Riemann problem is defined as a problem concerning conservation equations with piecewise initial conditions, which has a single discontinuity at the area of interest. This means, that the Riemann problem appears at the

borders of the cells of the hydrodynamic grid, when e.g. energy has to be transferred between the two neighbouring cells.

There are many other approaches for the solution of Riemann problem, but here, the very basic idea of HLLC solution is presented. The HLLC approach is based on Godunov method. The fundamental idea of this method is that for each cell of the grid, into which the fluid is divided, the conserved variables, such as energy-momentum density, are set. According to these conserved variables the *flow variables*¹ are introduced, such as pressure and velocity. The flow variables are limited in order to have linear profile in each cell. Now, the most appealing step is to solve Riemann problem at the boundaries between each two cells in order to obtain *resolved states* or *fluxes*. The new conserved variables, for next step in evolution, are then a combination of the old conserved variables with the resolved states.

To explain the paragraph above more illustratively, one can imagine a tube divided into several cells. Let us have vector of conserved variables in i -th cell during the n -th time step Q_i^n . Then, at the boundary between i -th and $(i + 1)$ -st cell, there is a flux $F(Q_i^n, Q_{i+1}^n)$. Since each cell has two boundaries the new conserved variables of i -th cell for $(n + 1)$ -st time step is

$$Q_i^{n+1} = Q_i^n - \frac{\Delta t}{\Delta x} \left(F(Q_i^n, Q_{i+1}^n) - F(Q_{i-1}^n, Q_i^n) \right), \quad (5.3)$$

where Δt is a size of the time step and Δx size of the cell. This procedure is done at each time step for each two cells until the hydrodynamic computations are finished after the final time step.

Back to the model itself, the hydrodynamic equations are solved in Israel-Stewart framework. The equations are in the form

$$\begin{aligned} \tilde{\gamma} \left(\partial_\tau + \tilde{v}_i \tilde{\partial}_i \right) \tilde{\pi}^{\mu\nu} &= - \frac{\tilde{\pi}^{\mu\nu} - \tilde{\pi}_{NS}^{\mu\nu}}{\tau_\pi} + I_\pi^{\mu\nu} \\ \tilde{\gamma} \left(\partial_\tau + \tilde{v}_i \tilde{\partial}_i \right) \Pi &= - \frac{\Pi - \Pi_{NS}}{\tau_\Pi} + I_\Pi, \end{aligned} \quad (5.4)$$

together with

$$\partial_\nu T^{\mu\nu} = 0 \quad (5.5)$$

and the full solution of the equations can be summarized in three steps. Firstly, only the ideal part (without the viscous terms) is evolved over full timestep in order to obtain the ideal part of the solution. Secondly, the Israel-Stewart equations are solved to propagate $\pi^{\mu\nu}$ and Π to the next timestep and Navier-Stokes terms are computed in the half-step. In the last step the equations are evolved with viscous terms only. For the longitudinal expansion the Milne coordinates are used.

One of the main features of the vHLLC code is that the common assumptions of boost-invariant longitudinal expansion and zero net-baryon density in the entire system are relaxed. Such loosening of those assumptions is necessary for collisions at lower energies, such as those energies $\sqrt{s_{NN}} = 7.7 - 62.4$ GeV at RHIC Beam Energy Scan.

Last year brought a crucial improvement for the vHLLC code. In addition to already implemented shear viscosity, the bulk viscosity was used as well. There are several bulk viscosity parametrizations available. The first parametrization is given by

¹note: different quantity from anisotropic flow

$$\frac{\zeta}{s}(T) = \begin{cases} 0.03 + 0.9e^{\frac{T/T_p-1}{0.0025}} + 0.22e^{\frac{T/T_p-1}{0.022}} & T < 180 \text{ MeV} \\ 27.55\frac{T}{T_p} - 13.45 - 13.77\frac{T}{T_p}^2 & 180 \text{ MeV} < T < 200 \text{ MeV} \\ 0.001 + 0.9e^{\frac{-(T/T_p-1)}{0.0025}} + 0.25e^{\frac{T/T_p-1}{0.13}} & T > 200 \text{ MeV}, \end{cases} \quad (5.6)$$

where T is the temperature and $T_p = 180$ MeV. The first parametrization is referred as *Param. I* in Fig.5.1. The second parametrization, *Param. II* in Fig.5.1, is defined as

$$\frac{\zeta}{s}(T) = \begin{cases} B_{norm} \frac{B_{width}^2}{(T/T_{peak}-1)^2 + B_{width}^2} & T > T_{peak} \\ B_{norm} \exp\left[-\left(\frac{T-T_{peak}}{T_{width}}\right)^2\right] & T < T_{peak}. \end{cases} \quad (5.7)$$

The parameters are set with $T_{peak} = 165$ MeV, $B_{norm} = 0.24$, $B_{width} = 1.5$ and $T_{width} = 10$ MeV. The last, *Param. III* in Fig.5.1, is established as

$$\frac{\zeta}{s}(T) = \begin{cases} B_n \exp\left(-\frac{(T-T_p)^2}{B_1^2}\right) & T < T_p \\ B_n \exp\left(-\frac{(T-T_p)^2}{B_2^2}\right) & T > T_p. \end{cases} \quad (5.8)$$

Here, the parameters have values $B_n = 0.13$, $B_1 = 10$ MeV, $B_2 = 120$ MeV and $T_p = 160$ MeV. All of the parametrizations are depicted in the Fig.5.1. For further information about the parametrization see [21] for *Param. I*, [22] for *Param. II* and [23] for *Param. III*.

The whole principle of the vHLE code is described in more detail in [24].

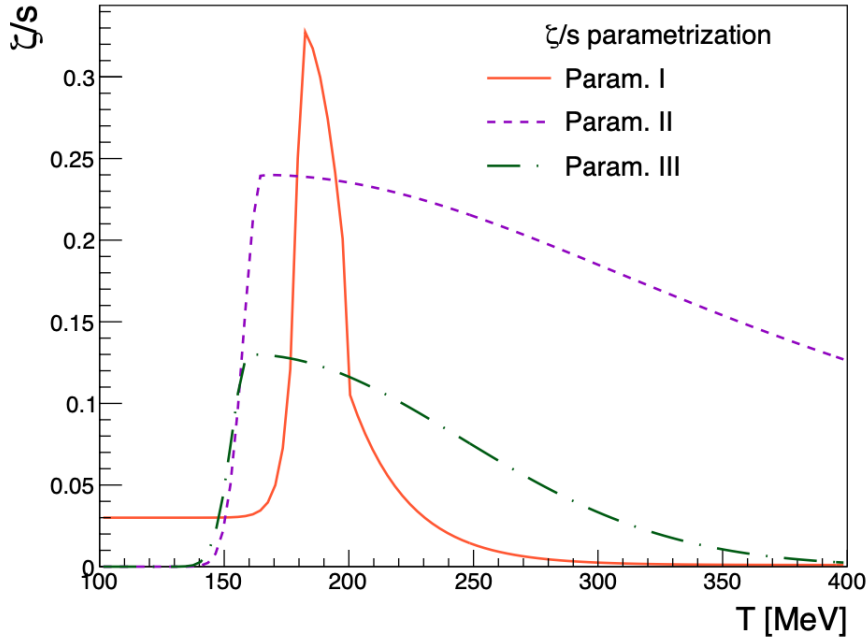


Fig. 5.1: Depiction of courses of the parametrizations of the bulk viscosity $\frac{\zeta}{s}$ as a function of temperature T . *Param. I* corresponds to parametrization (5.6), *Param. II* to (5.7) and *Param. III* to (5.8). Figure taken from [25].

5.3 hadronSampler

The last piece to the whole package is a hadronSampler code. Once the system becomes dilute, the hydrodynamic approach is not valid anymore. That is why, as the system reaches the critical energy density and hydrodynamic evolution is terminated, the particlization is performed by hadronSampler code. It is based on the Cooper-Frye formula (5.11) which is applied to particlize the system at the formed hyperurface of constant local rest-frame energy density, the critical energy density. This step is crucial in order to obtain identified particle spectra and correlation observables, which are influenced by resonance decays and baryon annihilation. In the original package, UrQMD is included for post freeze-out rescattering of particles created from the fluid. However, in the past year, the hadronSampler was changed and the modified SMASH² hadronSampler is now used instead of the UrQMD.

5.3.1 SMASH

The SMASH (Simulating Many Accelerated Strongly-interacting Hadrons) code is hadronic transport approach model which includes the effects of the hot and dense matter such as many-body interactions. It is based on solving non-equilibrium dynamics of hadrons by means of relativistic Boltzmann equation

$$p^\mu \partial_\mu f_i(x, p) + m_i F^\alpha \partial_\alpha^p f_i(x, p) = C_{coll}^i, \quad (5.9)$$

where C_{coll}^i is the collision term, $f_i(x, p)$ is a single-particle distribution for each species, F^α is the force experienced by individual particles and m_i is the mass of the particle. The Boltzmann equation is a integro-differential equation in 6+1 dimensions. The criterion for a collision to occur is that the distance

$$d < d_{int} = \sqrt{\frac{\sigma_{tot}}{\pi}}, \quad (5.10)$$

where the σ_{tot} is the total cross section.

Moreover, the SMASH code can be used as *afterburner* for the hydrodynamic model, once the particles are sampled from the Cooper-Frye hypersurface. The particles are then rescattered accordingly to the SMASH procedure.

For further description of the SMASH code see [26], and for SMASH hadronSampler see [27], [28] and [29].

In addition to the SMASH, the hadronSampler was modified (see [27], [30] and [31]) in order to be capable of treatment of the viscosity corrections. The Cooper-Frye formula containing the corrections for the viscosities used in SMASH hadronSampler has the form

$$\frac{d^3 \Delta N_i}{dp^* d(\cos \theta) d\varphi} = \underbrace{\frac{\Delta \sigma_\mu^* p^{*\mu}}{p^{*0}}}_{W_{residual}} \underbrace{p^{*2} f_{eq}(p^{*0}; T; \mu_i)}_{isotropic} \underbrace{\left[1 + (1 \mp f_{eq}) \frac{p_\mu^* p_\nu^* \pi^{*\mu\nu}}{2T^2(\varepsilon + p)} \right]}_{W_{viscous}}. \quad (5.11)$$

The symbol of the star denotes the rest frame values of given quantities and f_{eq} is the phase space distribution function. The procedure for creation of an ensemble of particles at each hypersurface element $\Delta \sigma_i$ can be summarized into few simple steps.

Firstly the average number of every species of a hadron is computed as

$$\Delta N_i = \Delta \sigma_\mu u^\mu n_{i,th} = \Delta \sigma_\mu^* n_{i,th}^*, \quad (5.12)$$

²which is open-source

where u^μ is the flow velocity and $n_{i,th}^\mu$ is flux of species i through the freeze-out hypersurface. Then, using the total mean number of particles, $\langle N_{tot} \rangle = \sum_i N_i$, as a mean value, the number of particles to be generated is given by Poisson distribution. For each particle, the species is randomly chosen accordingly to the probability N_i/N_{tot} .

The momentum of the created particle is assigned randomly according to the isotropic part in (5.11), taking into account, however, the corrections for $W_{residual}$ or $W_{residual} \cdot W_{viscous}$ respectively.

The form of the phase space distribution function f_{eq} , which also takes into account the bulk viscosity corrections, can be expressed as in [30], [31],

$$f_{eq,n} = \frac{\mathcal{Z}_n g_n}{\exp \left[\frac{\sqrt{p'^2 + m_n^2}}{T + \beta_\Pi^{-1} \Pi \mathcal{F}} - b_n \left(\alpha_B + \frac{\Pi \mathcal{G}}{\beta_\Pi} \right) \right] + \Theta_n}. \quad (5.13)$$

Here n denotes a particle species, \mathcal{Z}_n is a normalization factor, g_n spin degeneracy factor, α_B is the ratio of chemical potential and temperature. The \mathcal{F} , \mathcal{G} and β_Π are coefficients and $\Theta_n \in [-1, 1]$ accounts the quantum statistics of fermions or bosons.

Chapter 6

Beam Energy Scan at RHIC

In recent years LHC and RHIC operated at their maximum energies. These collisions at maximum energies of LHC or RHIC probe the part of the phase diagram of strongly interacting matter, where baryon chemical potential is close to zero $\mu_B \simeq 0$ and rather high temperatures. However, phase transition at this region is now quite well understood. Therefore, study of the phase diagram of the strongly interacting matter in different sections is at hand. One can maneuver in the phase diagram by adjusting the collision energy. For lower collision energies (as described more in Chapter 1) the baryon chemical potential reaches higher values, and thus other regions of the diagram than those for high energies can be probed. This is exactly the aim of RHIC Beam Energy Scan (BES) program. During the Beam Energy Scan the Au+Au were collided and the program was operated at the energies in range from $\sqrt{s_{NN}} = 7.7 - 62.4$ GeV. Even lower-energy collisions are available when using fixed target measurements.

There are basically three main goals of the RHIC BES program. First is to search for the onset of the deconfinement, i.e. the point of the phase transition. The last two are then search for the critical point of the phase diagram and search for the signatures which could indicate the first order transition of the matter. The range $\sqrt{s_{NN}} = 7.7 - 62.4$ GeV is believed to cover all three goals.

Schematic illustration of the phase diagram with BES energies is depicted in Fig.6.1.

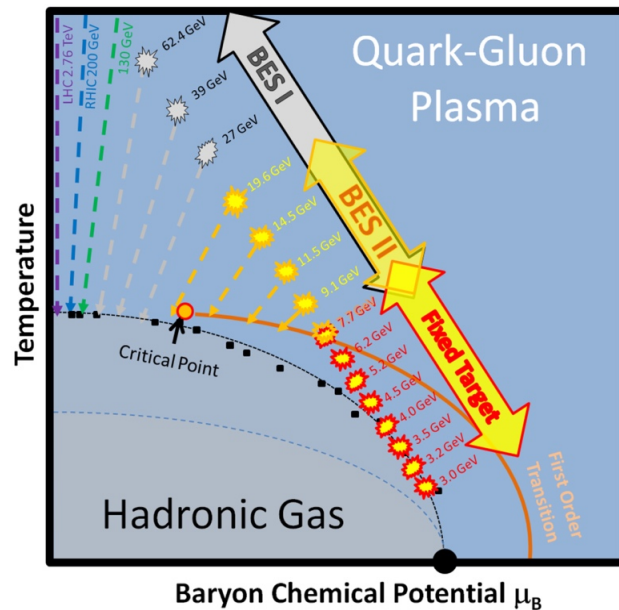


Fig. 6.1: An illustration of phase diagram with values of collision energy probes by RHIC BES program. Figure taken from [32].

6.1 Particle spectra from BES

Basic but important results of the analysis of the data taken during the BES program are identified hadron spectra. Such spectra are presented in the paper [33] together with other bulk properties for different centralities and various collision energies. In our case, the interest is mainly in particle spectra from collision at energy $\sqrt{s_{NN}} = 27$ GeV. In the Fig.6.2, there are the pion, kaon and proton spectra for various centrality classes. Each centrality class is scaled by corresponding factor in order to make the plot clearer. The spectrum is in range of $p_T = 0 - 2$ GeV/c, thus only the soft part of the particle spectrum is presented. Eventually, the π^+ spectrum for centrality 20-30% will be particularly important, concerning the task of this work. The data were taken with minimum bias trigger and 33 million events were analyzed.

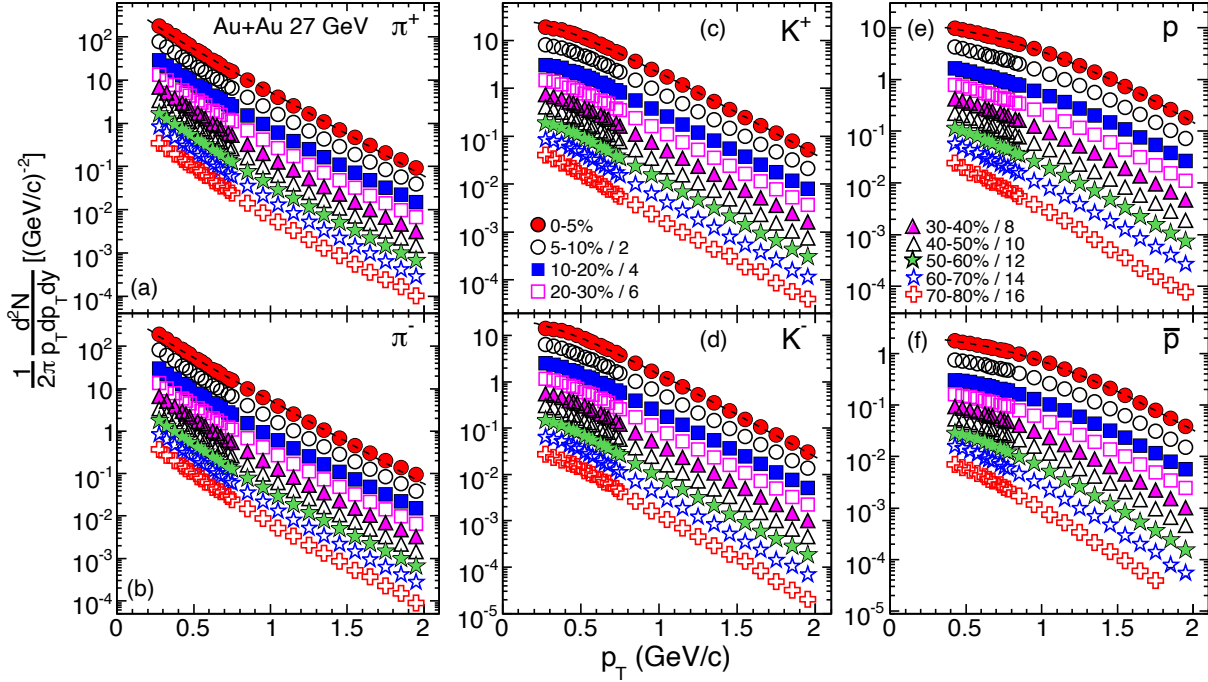


Fig. 6.2: Mid-rapidity ($|\eta| < 0.1$) transverse spectra for (a) π^+ , (b) π^- , (c) K^+ , (d) K^- , (e) p and (f) \bar{p} in Au+Au collisions at $\sqrt{s_{NN}} = 27$ GeV for different centralities. The spectra for centralities other than 0–5% are scaled for clarity as shown in figure. The uncertainties are statistical and systematic added in quadrature. Figure and caption taken from [33].

6.2 Elliptic flow from BES

The other important results of the analysis of the data are presented in the paper [34]. Here, the results of the elliptic flow for different centrality bins and various collision energies are presented. In the paper, several approaches to compute the elliptic flow v_2 are used. Among others, also 2 and 4 particle cumulant method and event plane method are used. Various methods are used in order to study nonflow fluctuations. The results were also compared to UrQMD simulation (Fig.6.4, using 4 cumulant method), which does underpredict the flow obtained by the STAR collaboration. Again, the particular plot which is the most significant for this work is the one for collision energy $\sqrt{s_{NN}} = 27$ GeV, Fig.6.3 (d1). The comparison with UrQMD, however, is not presented for the energy $\sqrt{s_{NN}} = 27$ GeV.

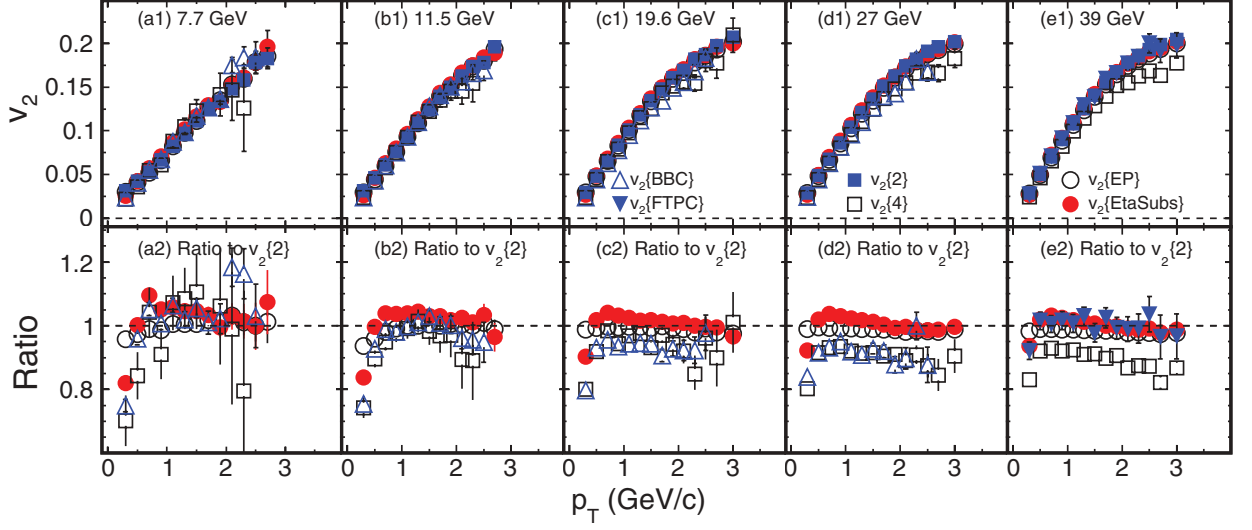


Fig. 6.3: The elliptic flow as a function of p_T for Au+Au collisions at centrality 20-30%. Dependencies for several collision energies are plotted. Figure taken from [34].

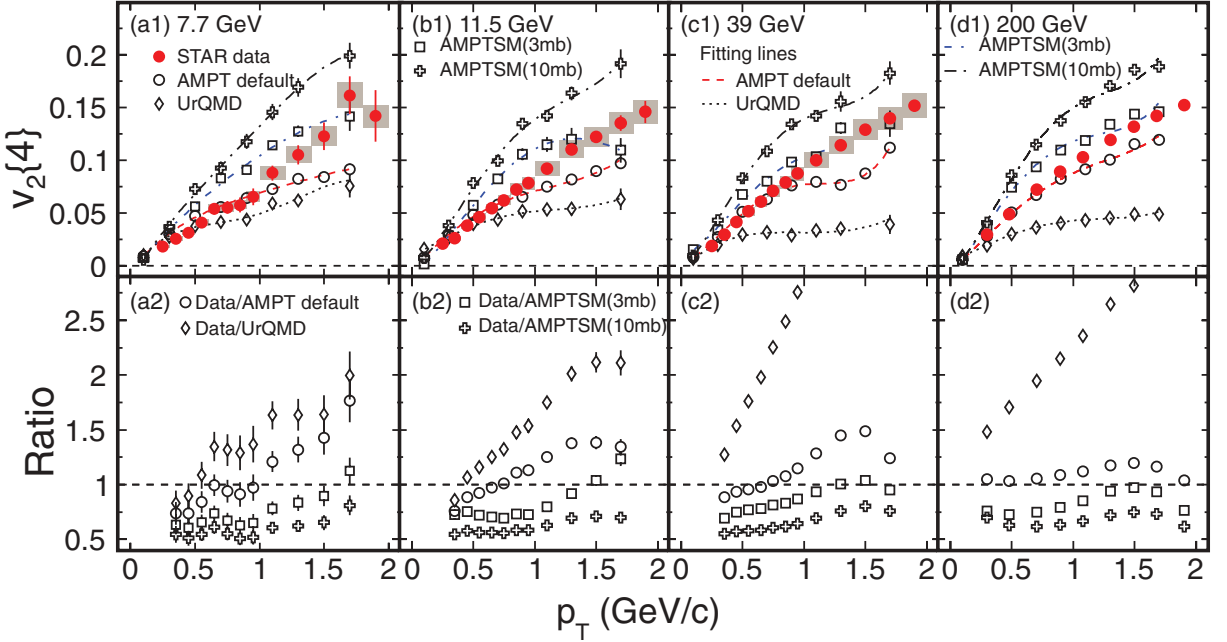


Fig. 6.4: Data obtained by STAR collaboration (red points) compared to several model simulations. The centrality class is 20-30%. Figure taken from [34].

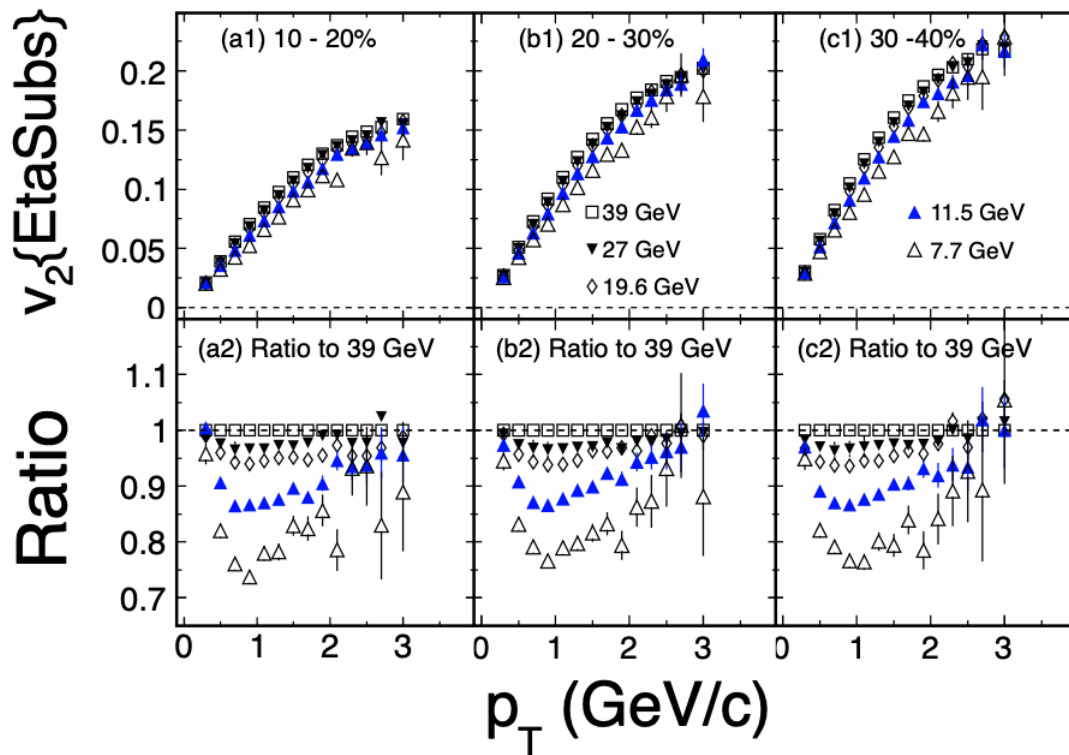


Fig. 6.5: The elliptic flow as a function of p_T , obtained by the η sub-event method. The data are presented for several collision energies (7.7 GeV, 11.5 GeV, 19.6 GeV, 27 GeV and 39 GeV) and for three centrality classes (10-20%, 20-30% and 30-40%). Figure taken from [34].

Chapter 7

Motivation

For the purpose of study of the properties of the strongly interacting matter, it is convenient to compare experimental data to those obtained by models. In case of this work, the vHLE hybrid model with Glissando Glauber model as initial conditions was used to reproduce the RHIC BES data, e.g. in [35], but the elliptic flow does not match the experimental data obtained by the STAR collaboration (see Fig.7.1). However, it would be useful to have simulations corresponding to experimental data. The aim of our effort is to come up with a way, how to introduce the elliptic flow increase to the simulation.

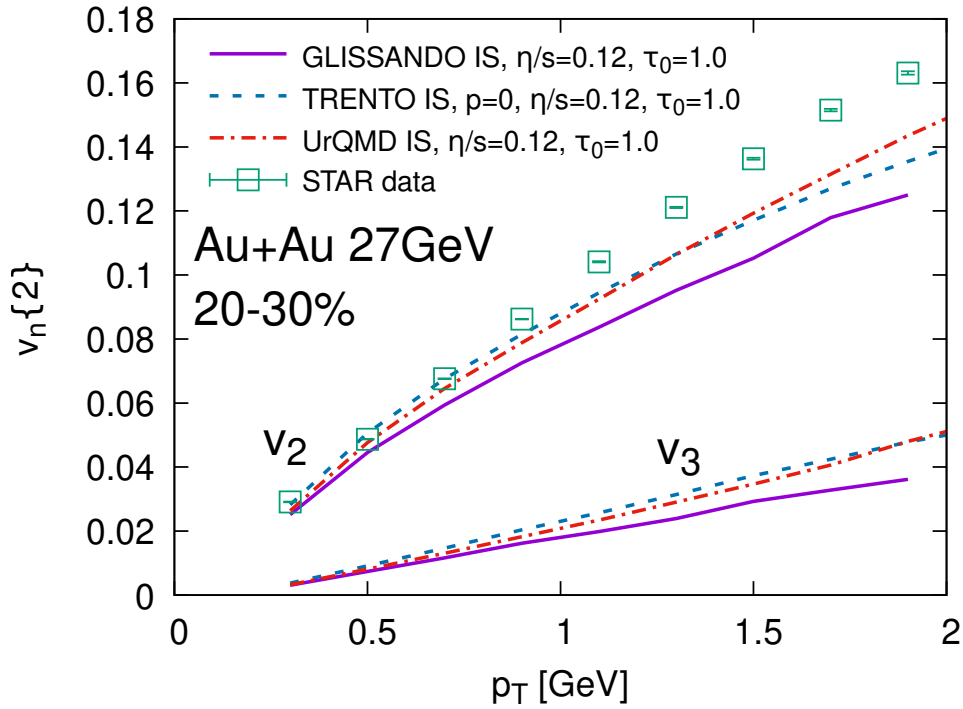


Fig. 7.1: Elliptic flow v_2 and triangular flow v_3 transverse momentum dependence for all charged hadrons for Au+Au collisions at $\sqrt{s_{NN}} = 27$ GeV and centrality 20-30%. The green points represent RHIC BES data from [34] and the purple line the flow obtained using Glissando and vHLE package. Figure taken from [35].

7.1 Adding initial velocity to hydrodynamic grid

In our recent work, the Research task [36] in particular, a simplistic approach for adding the elliptic flow to initial conditions was used. The main idea was to introduce some initial velocity

directly to each cell of the hydrodynamic grid. Nevertheless, the initial velocity should satisfy a few assumptions in order to add the elliptic flow. Firstly, it should reflect the radial coordinate of the cell being added to. For a cell further from the center of the collision, thus closer to the edge of the fireball, the magnitude of the velocity should be bigger than for those cells which are closer to the center, i.e. the velocity should grow in some manner with the radius. Secondly, the elliptic flow should be added, so the angular dependence should be set in accordance with eq. (3.2). The prescription for the velocity added was chosen as

$$v(r, \varphi) = \zeta \left(\frac{r}{r_{max}} \right)^2 (1 + 2a \cos(2\varphi)) + v_{rand}. \quad (7.1)$$

The radial dependence is provided by the r/r_{max} term, where r is the radial coordinate of the cell in the transverse plane and $r_{max} = 3.5$ fm denotes typical size of the fireball at the beginning of the evolution in non-central collisions in the 20-30% centrality class. The distribution of the velocity along the radial coordinate is not linear, hence the second power of the ratio r/r_{max} was chosen and turned out to be sufficient. The term $\cos(2\varphi)$ secures the right variation in the azimuthal angle and thus adding indeed the elliptic flow. The prescription for the velocity (7.1) has also several parameters. First of them, ζ denotes the amplitude or strength of the radial part of the velocity added. The second parameter a represents the amplitude of the azimuthal part of the velocity distribution, in this work called the ellipticity of the distribution.

The last term, v_{rand} , actually contains two more parameters. It represents a random component of the velocity given by the Gaussian distribution on top of the radial and azimuthal distribution. The two parameters mentioned are the width of the Gaussian σ and the mean value of the Gaussian μ . In order to have more positive contribution from the v_{rand} , the μ was set to 0.05 in natural units. Moreover, the v_{rand} adds just the magnitude of the velocity, i.e. its contribution is in the same direction.

For the norm of the velocity the condition

$$\|v\| < 1 \quad (7.2)$$

is held, in order not to exceed the speed of light. For those cells the velocity of which is bigger than 1, the velocity is artificially set to $v = 0.999$.

The influence of the three parameters on spectra and v_2 is depicted in Fig.7.2-7.7. The results for the process of adding the initial velocity are demonstrated on the Au+Au collision at centrality 20-30% and at the collision energy $\sqrt{s_{NN}} = 27$ GeV. By hydrodynamics, 200 events were simulated. From each event simulated by hydrodynamics, 200 events were produced by hadronSampler (using UrQMD). For all following plots in this section, the red points represent data obtained by STAR collaboration (taken from [33] and [34]). The black solid line represents the simulation with no initial velocity, i.e. before the velocity (7.1) was added. The colored lines correspond to individual values of each parameter. In addition, throughout this whole chapter, the bulk viscosity is set to zero in the hydrodynamics.

All in all, the parameters have favourable behaviour. The value of the ζ parameter can be set accordingly to the shape of the spectrum from experiment and once ζ is fixed, the a parameter can be set in order to reproduce the desired elliptic flow. The σ parameter should be set in reasonable range.

Alas, the spectrum is spoiled by addition of any flow and thus the parameters cannot be set. The possible solution for lowering the radial flow might be introduction of the bulk viscosity to the vHLLC.

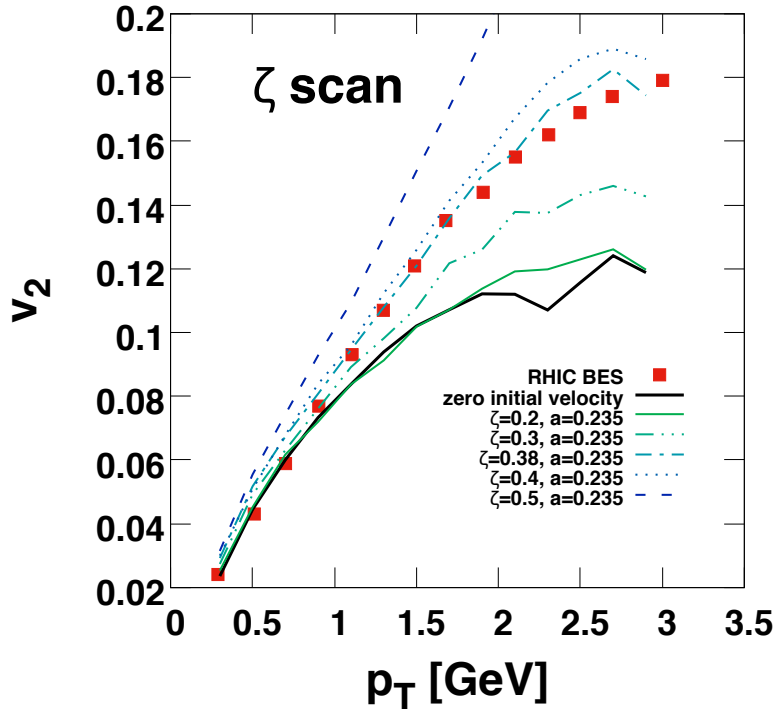


Fig. 7.2: Scan of the ζ parameter influence on elliptic flow v_2 for Au+Au collision at centrality 20-30% and $\sqrt{s_{NN}} = 27$ GeV. The red points represent BES data from [34], the black solid line refers to the result of the simulation for no initial velocity added. The colored lines denote individual parameter values. The parameter a is set constant $a = 0.235$ and $v_{rand} = 0$.

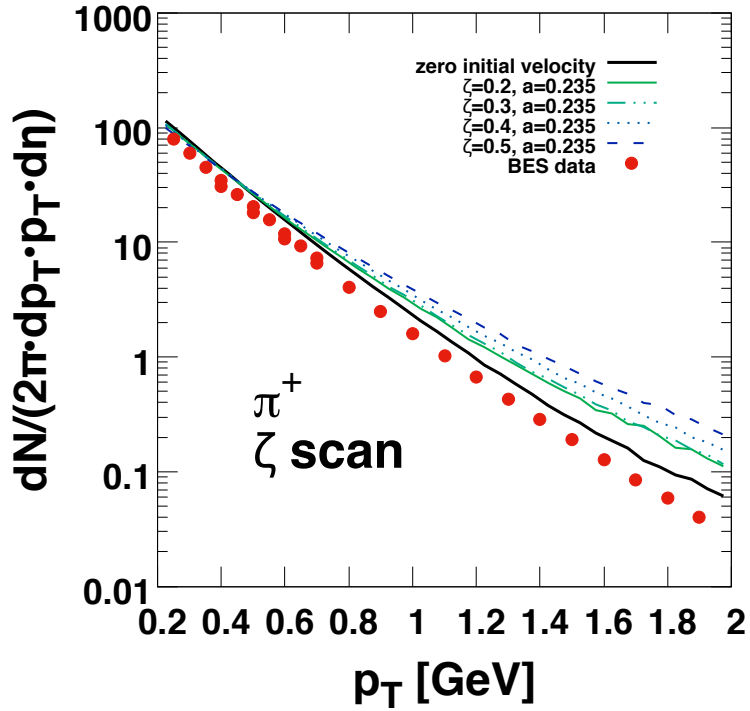


Fig. 7.3: Scan of the ζ parameter influence on p_T spectrum for Au+Au collision at centrality 20-30% and $\sqrt{s_{NN}} = 27$ GeV. The red points represent BES data from [33], the black solid line refers to the result of the simulation for no initial velocity added. The colored lines denote individual parameter values. The parameter a is set constant $a = 0.235$ and $v_{rand} = 0$.

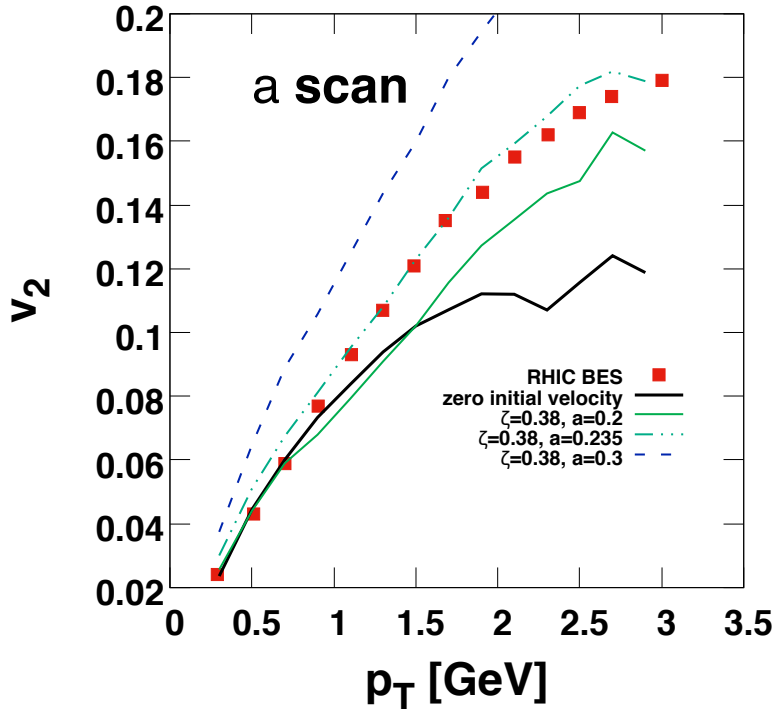


Fig. 7.4: Scan of the a parameter influence on elliptic flow v_2 for Au+Au collision at centrality 20-30% and $\sqrt{s_{NN}} = 27$ GeV. The red points represent BES data from [34], the black solid line refers to the result of the simulation for no initial velocity added. The colored lines denote individual parameter values. The parameter ζ is set constant $\zeta = 0.38$ and $v_{rand} = 0$.

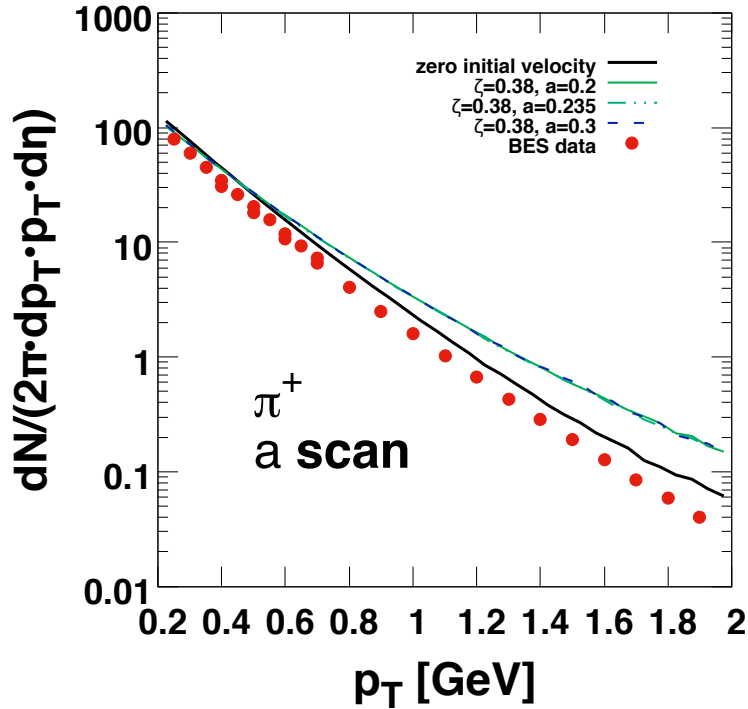


Fig. 7.5: Scan of the a parameter influence on p_T spectrum for Au+Au collision at centrality 20-30% and $\sqrt{s_{NN}} = 27$ GeV. The red points represent BES data from [33], the black solid line refers to the result of the simulation for no initial velocity added. The colored lines denote individual parameter values. The parameter ζ is set constant $\zeta = 0.38$ and $v_{rand} = 0$.

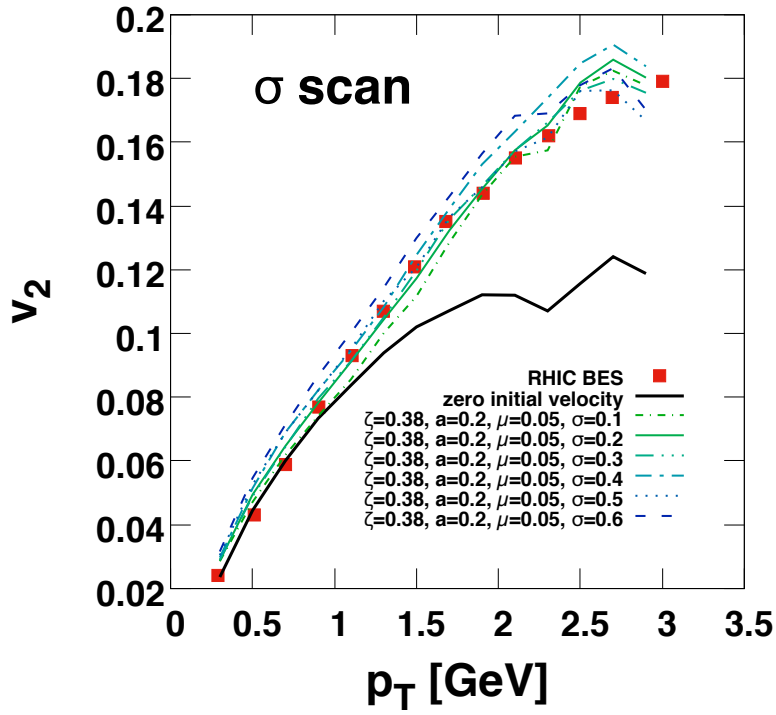


Fig. 7.6: Scan of the σ parameter influence on elliptic flow v_2 for Au+Au collision at centrality 20-30% and $\sqrt{s_{NN}} = 27$ GeV. The red points represent BES data from [34], the black solid line refers to the result of the simulation for no initial velocity added. The colored lines denote individual parameter values. The parameters ζ , a and μ are set constant, $\zeta = 0.38$, $a = 0.235$ and $\mu = 0.05$.

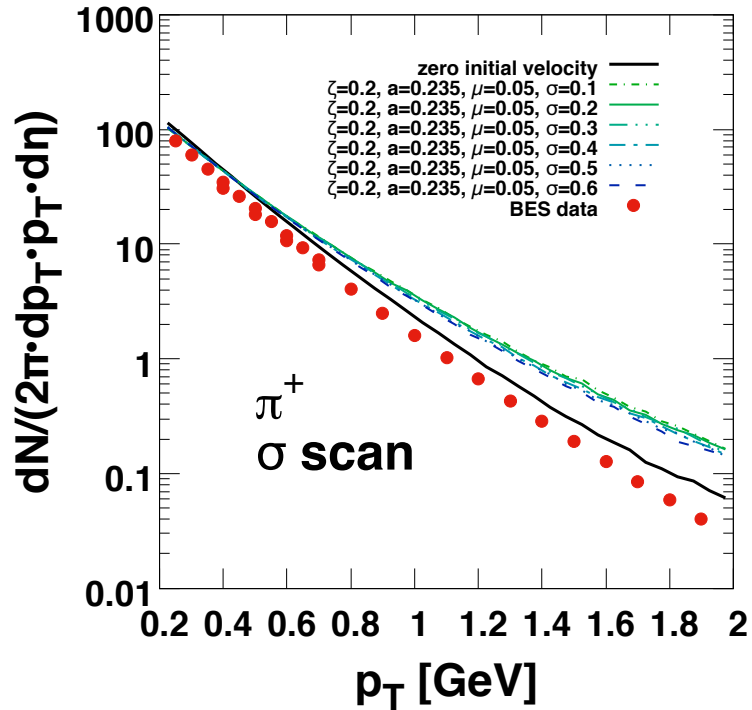


Fig. 7.7: Scan of the σ parameter influence on p_T spectrum for Au+Au collision at centrality 20-30% and $\sqrt{s_{NN}} = 27$ GeV. The red points represent BES data from [33], the black solid line refers to the result of the simulation for no initial velocity added. The colored lines denote individual parameter values. The parameters ζ , a and μ are set constant, $\zeta = 0.38$, $a = 0.235$ and $\mu = 0.05$.

Chapter 8

IMAGO: Glauber model with initial momentum anisotropy

As explained in the motivation in the previous chapter, a model which could add the elliptic flow to the simulations using vHLL hybrid package is needed. The model implemented into the vHLL during the Research project has shown at least some positive feedback, although its behaviour was not of any use. The way it was done in Research project was rather simplistic and artificial in a way that it was not based on any physical mechanism present in the model and so an idea of more realistic model arose, in order to do it more properly. Therefore, we have decided to construct completely new model for creating initial conditions for the hydrodynamic simulations. Of course, since we wanted to improve results given when Glissando was used as initial state generator, the concept of Glauber Monte Carlo model had to be kept also for the new model.

The basic idea of this new model is to implement a random walk for a transverse momentum deposition during the collision. As a result the transverse momentum field would be present as an output for each source¹. Thus, the new model was named *Initial Momentum Anisotropy Glauber mOdel*, or IMAGO.

Let us then introduce the basic principles of how the model is constructed and its working mechanism.

8.1 Basic principles of IMAGO

As stated above, IMAGO is a Glauber model and as such, the common assumptions must be kept. First, the distribution according to which the nucleons are distributed in the nucleus has to be provided.

8.1.1 Generating nuclei

As a first step, the nucleons in given nucleus have to be created for further procedure. The basic input which governs distribution of the nucleons inside the nucleus and which is commonly used in such circumstances is already well-known *Woods-Saxon* formula, which in spherical coordinates has the form

$$d^3\rho(\vec{r}) = \frac{r^2\rho_0}{1 + \exp\left(\frac{r-R}{a}\right)} d(\cos\varphi)d\theta dr. \quad (8.1)$$

¹source is meant in the same way as in Chapter 5, Glissando subsection

There are spherical coordinates r , which is the radius, φ is the azimuthal angle and θ the polar angle. The parameter ρ_0 denotes the nuclear density in the center of the nucleus and is given by tabulated values and in fact can be determined from normalization if (8.1) is considered as probability distribution. The a parameter here refers to the thickness of the skin layer of given nucleus and its values are tabulated as well. The radius of the nucleus R can be usually parametrized as a function of the nucleon number A as $R = r_0 A^{1/3}$, where $r_0 = 1.2$ fm.

However, using (8.1) only the centers of the nucleons are generated. Since the nucleons are not point like object, a certain spacing between them must be kept. This brings new condition in the process of nucleus formation. In order to secure the spacing, the following procedure is executed. If newly generated nucleon is closer to other nucleons than the spacing distance d (which can be thought of as a radius of the nucleon), a new set of the coordinates r, φ, θ is generated, until the distance between all of the nucleons is sufficient, i.e. the distance is greater than d . This method, however, changes the probability density distribution, so the shape has no more the form of (8.1), but appears to be broader. In order to keep the probability density in the right shape, a correction to the radius of the nucleus R has to be introduced as

$$R = r_0 A^{\frac{1}{3}} - 0.656 A^{-\frac{1}{3}}, \quad (8.2)$$

which is suitable (according to the [15]) for the spacing $d = 0.9$ fm. Once the radius R is corrected, the changes due to the procedure of generating of the nucleons should be sufficiently compensated.

So far, the nucleons were distributed using spherical coordinates, in further discussion the cartesian coordinates x, y and z will be used. In Fig.8.1 is presented an example of Au+Au collision at the centrality 20-30% from IMAGO.

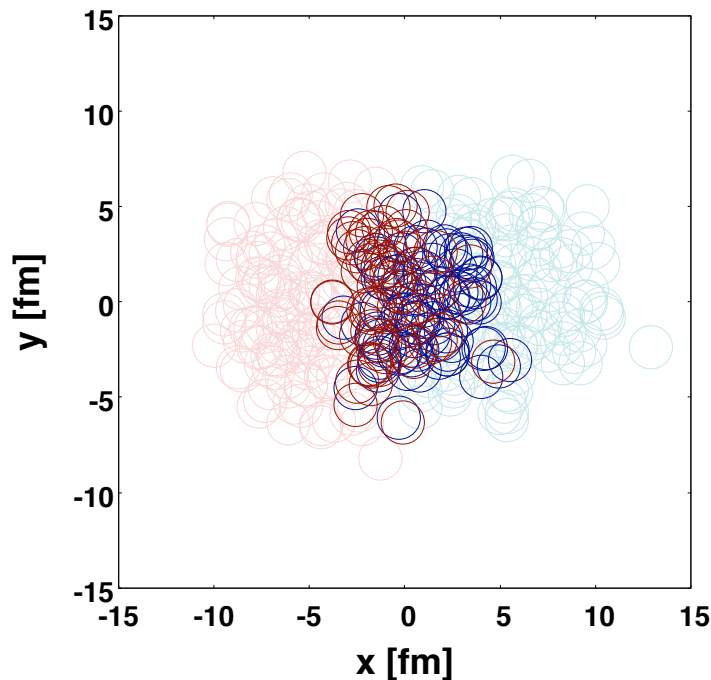


Fig. 8.1: An example of Au+Au collision at the centrality 20-30% from IMAGO. The full colored circles represent the participants, the faded circles represent the spectators. The spacing between the nucleons is set to $d = 0.9$ fm.

8.1.2 Collision of nuclei

Once the two nuclei are created, a collision should occur. Here the other basic assumption of the Glauber model appears, that the nucleons travel along straight lines, i.e. they are not reflected to the side when collided. Moreover, the collision occurs only if the nucleons flying against each other are close enough. The distance, which is sufficient for the collision is given by

$$d_{coll} < \sqrt{\frac{\sigma_{NN}}{\pi}}, \quad (8.3)$$

where σ_{NN} is the nucleon-nucleon inelastic cross section at given collision energy. Particular values for some of the collision energies can be found in Table 8.1.

| | | | | | | | |
|-----------------------|-------|-------|-------|-------|-------|-------|-------|
| $\sqrt{s_{NN}}$ [GeV] | 7.7 | 11.5 | 19.6 | 27 | 39 | 62.4 | 200 |
| σ_{NN} [mb] | 30.60 | 31.28 | 32.30 | 33.10 | 34.20 | 35.90 | 41.60 |
| α | 0.110 | 0.114 | 0.120 | 0.123 | 0.127 | 0.132 | 0.145 |

Table 8.1: Values of the inelastic nucleon-nucleon cross section σ_{NN} and the α parameter from (8.5) at given collision energies.

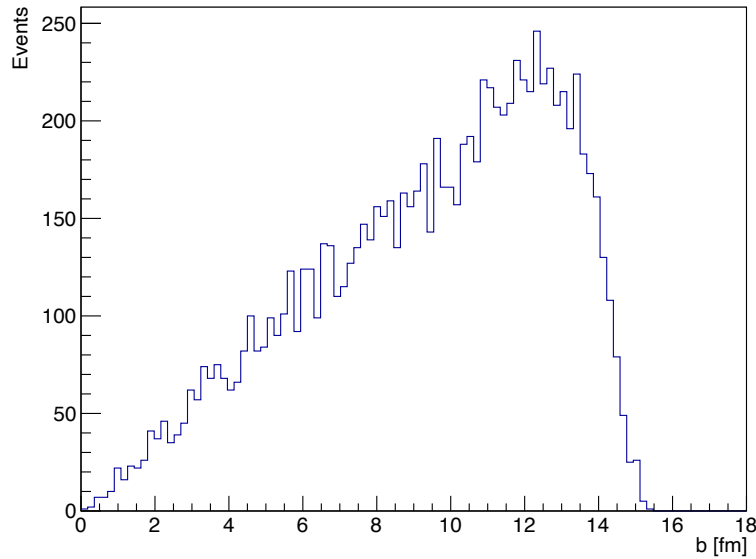


Fig. 8.2: Distribution of the impact parameter b in Au+Au collision from the IMAGO simulations. Only those collisions, where $N_{coll} > 0$ contributed.

The nomenclature here is the same as in the Chapter 2, i.e. those nucleons which undergo at least one inelastic interaction during the collision are called *participants* and their number is N_{part} and number of total amount of nucleon binary collisions is denoted by N_{coll} .

However, as mentioned before, the collisions are not head-on in most of the cases. Hence the impact parameter has to be introduced to the model. It is generated from by the probability distribution

$$\rho_b(b) = 2 \frac{b}{b_{max}^2}, \quad (8.4)$$

where the denominator gives the normalization to unity. Still, the maximal impact parameter b_{max} varies with the size of given nucleus. The distribution of the impact parameter for Au+Au

collisions can be seen in the Fig.8.2. Only those collisions, where $N_{coll} > 0$ were taken into account and the tail at the end of the distribution arises quite naturally as the nuclei start to miss each other.

Distributions for the N_{part} and N_{coll} in Au+Au collision can be found in Fig.8.3, resp. Fig.8.4.

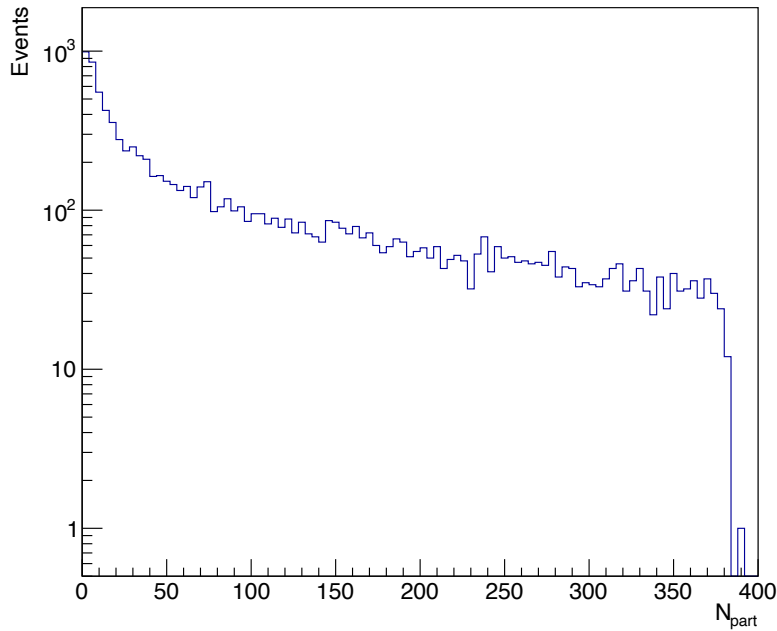


Fig. 8.3: Distribution of the number of participants N_{part} in Au+Au collisions from the IMAGO simulations.

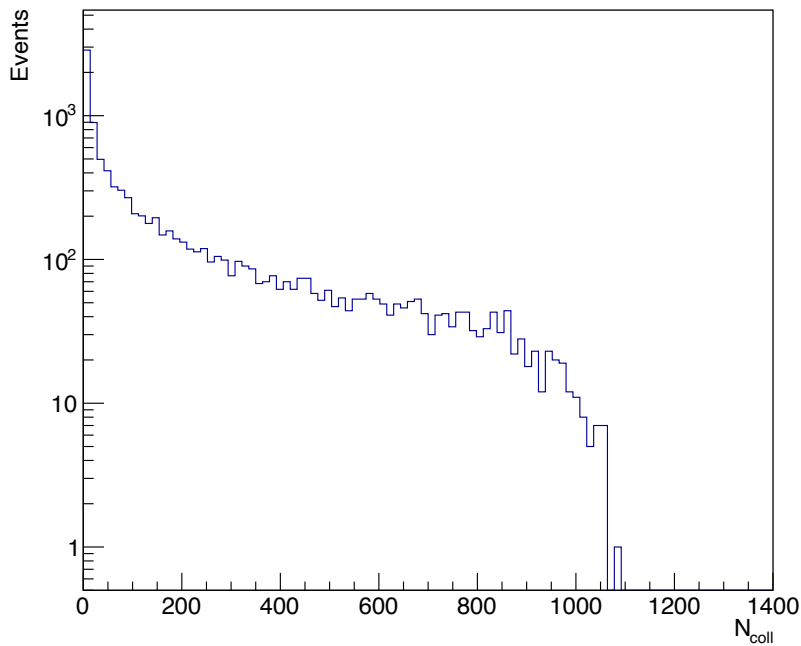


Fig. 8.4: Distribution of the number of binary nucleon-nucleon collisions N_{coll} in Au+Au collisions from the IMAGO simulations.

8.1.3 Centrality determination

It is desirable to simulate the collisions at different centralities. Nevertheless, the question of how the centrality should be determined arises quite naturally. Since the impact parameter is known in the model for each collision, defining the centrality accordingly to the impact parameter distribution could be an obvious choice. However, it is not completely appropriate choice, since the impact parameter is not known in the experiment and we would like to relate the result of the model to the experimental data. It is assumed though, that the impact parameter is a monotonic function of the particle multiplicity. Luckily enough, there is a quantity, which can be related to the particle multiplicity, called *relative deposited strength*, or RDS ([15], [16], [17]). It is proportional to the number of participants N_{part} and the number of binary collisions N_{coll} as

$$RDS = (1 - \alpha) \frac{N_{part}}{2} + \alpha N_{coll}, \quad (8.5)$$

where the α parameter is energy-dependent and as already mentioned in Chapter 5, it gives the proportionality to the soft, resp. hard part of the particle spectrum. The values of the α parameter for some of the collision energies can be found in Table 8.1. The RDS distribution for Au+Au collisions at the collision energy $\sqrt{s_{NN}} = 27$ GeV is plotted in Fig.8.5.

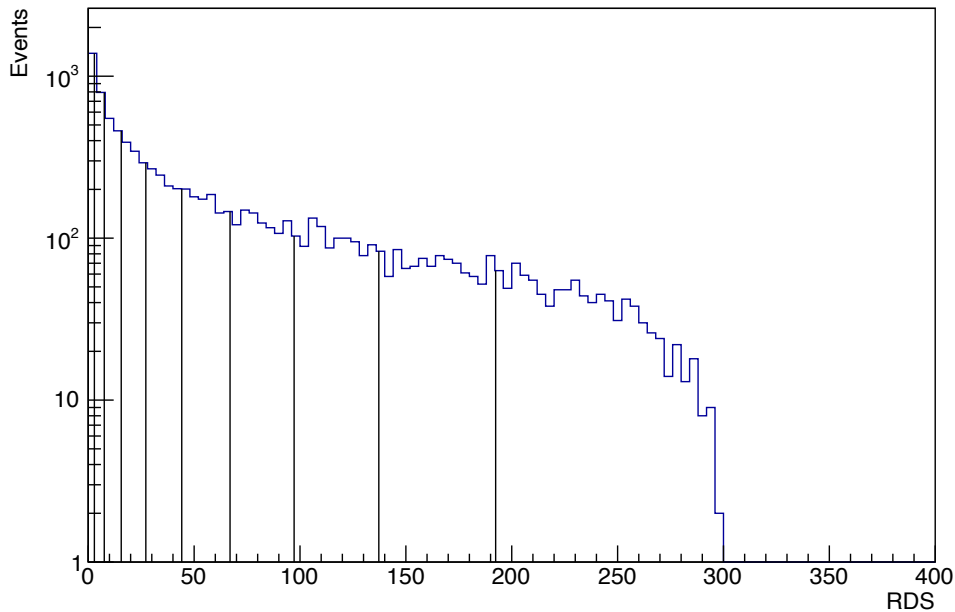


Fig. 8.5: Distribution of the RDS N_{coll} in Au+Au collisions from the IMAGO simulations. The black lines correspond to the borders of the centrality bins.

The RDS distribution was divided into percentiles of width 10% according to its cumulative distribution, i.e. the centrality classes. The borders of the centrality bins are represented by the black lines. For the model's sake, however, the RDS centrality classes need to be related back to the impact parameter. Since we know both of these quantities in the model, the mutual dependence could be constructed in Fig.8.6. In the figure, the centrality class 20-30% is illustrated. Even though the borders of the centrality class have sharp values in RDS, the borders for the impact parameter b are not clear, since for given value of RDS, the impact parameter can have many values. Therefore, the borders of the interval for the centrality class in the impact parameter are taken as maximal, resp. minimal values of b at the RDS centrality borders. These two points are depicted in the Fig.8.6 as well, b_{max} for the higher border of the interval and b_{min}

for the lower one. This is true for all centrality classes and together with the values of the RDS for Au+Au collisions at $\sqrt{s_{NN}} = 27$ GeV, they can be found in Table 8.2. It is apparent, that the centrality classes in the impact parameter overlap, so, if looked at the other way round, a collision with given impact parameter can fall into different centrality classes defined by RDS. However, only those events which has the value of RDS in the satisfactory interval are accepted.

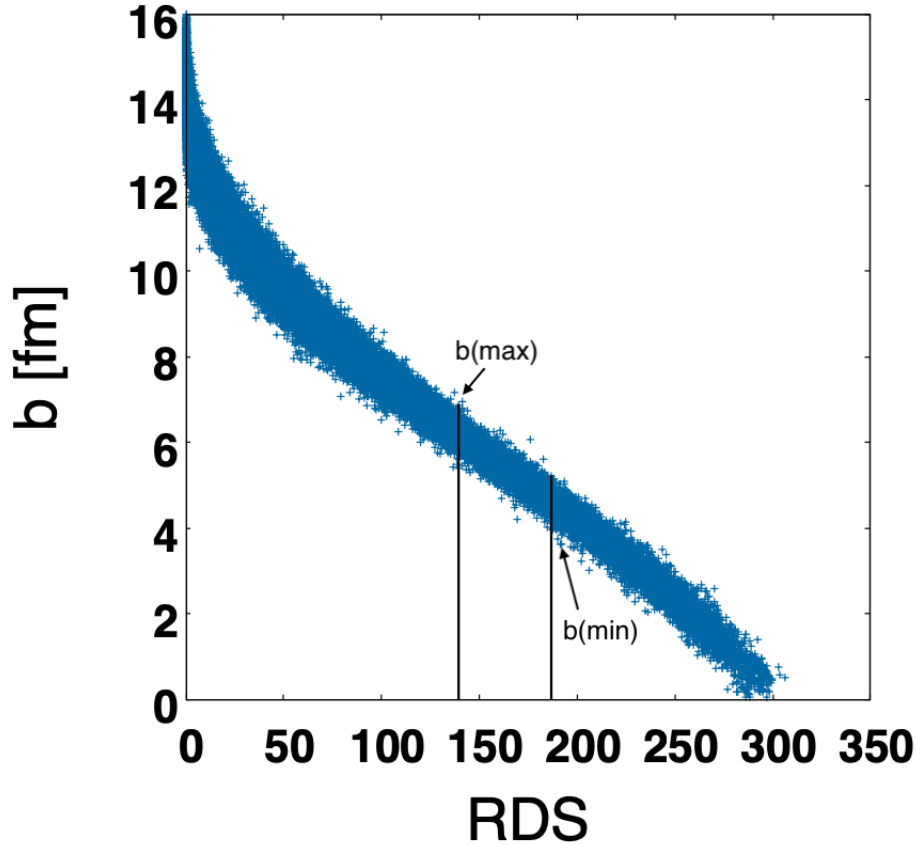


Fig. 8.6: Dependence of the impact parameter b and RDS from Au+Au collision from IMAGO simulations. The centrality class 20-30% accordingly to the RDS distribution is illustrated by the black lines.

| Centrality | b_{min} [fm] | b_{max} [fm] | RDS _{min} | RDS _{max} |
|------------|----------------|----------------|--------------------|--------------------|
| 0-10% | 0.00 | 4.92 | 192.40 | 300.00 |
| 10-20% | 3.86 | 6.93 | 137.22 | 192.40 |
| 20-30% | 5.64 | 8.55 | 97.21 | 137.22 |
| 30-40% | 6.84 | 9.62 | 66.96 | 97.21 |
| 40-50% | 7.85 | 10.81 | 44.15 | 66.96 |
| 50-60% | 8.82 | 11.81 | 27.18 | 44.15 |
| 60-70% | 9.81 | 12.85 | 15.56 | 27.18 |
| 70-80% | 10.62 | 13.87 | 7.55 | 15.56 |
| 80-90% | 11.01 | 14.67 | 2.88 | 7.55 |
| 90-100% | 11.67 | 16.00 | 0.00 | 2.88 |

Table 8.2: Values of the impact parameter b borders and RDS borders of the centrality classes in IMAGO. The values were obtained for Au+Au collisions at $\sqrt{s_{NN}} = 27$ GeV.

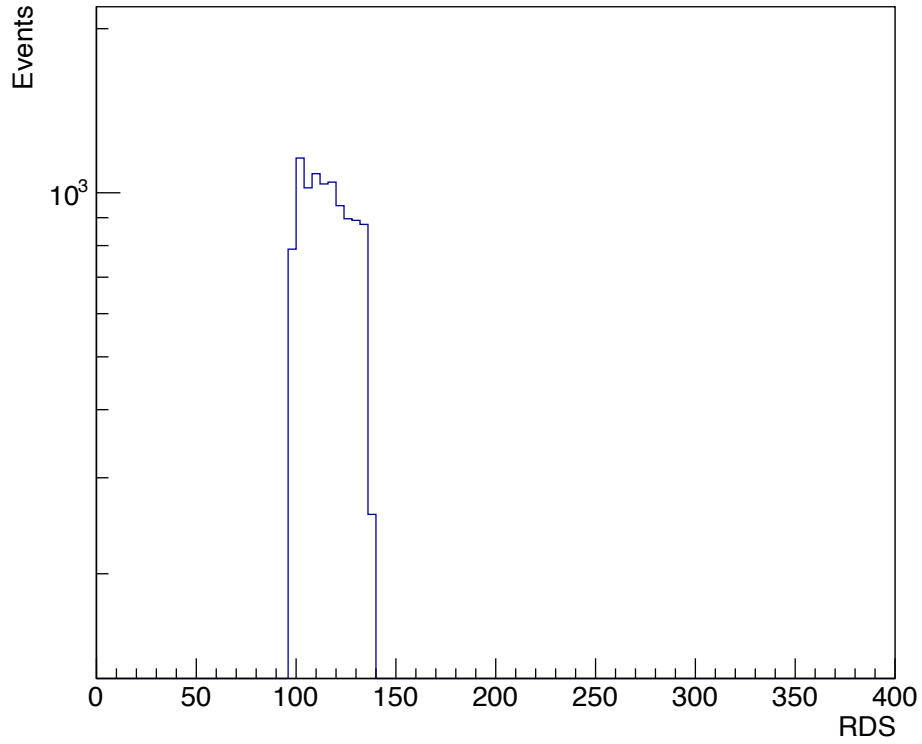


Fig. 8.7: RDS centrality class of 20-30% from Au+Au collisions in IMAGO simulations. The borders of the bin are not sharp because of the binning of the histogram.

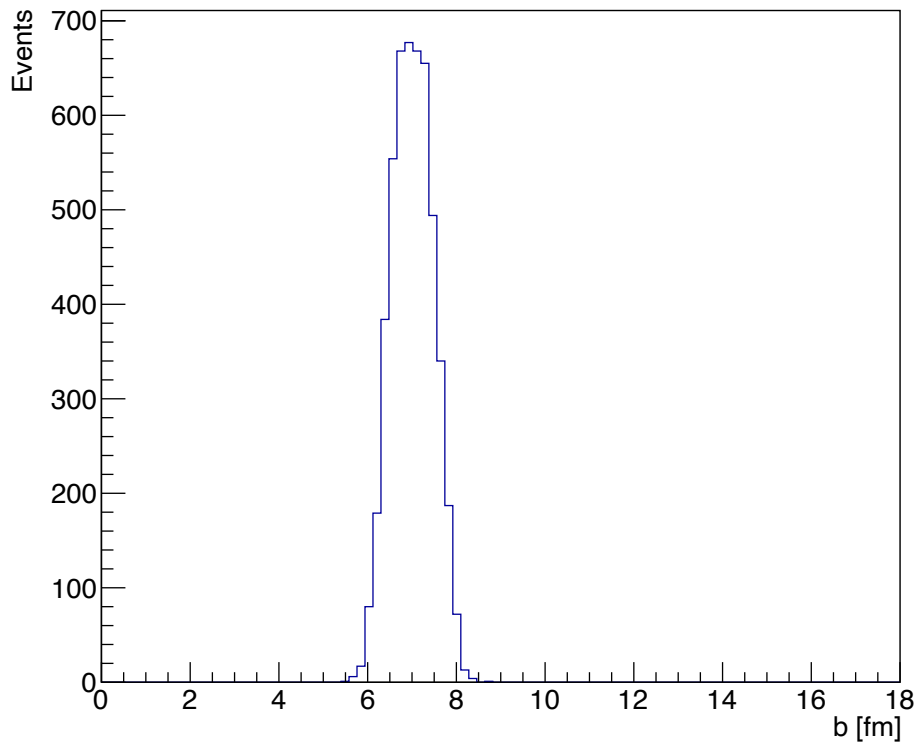


Fig. 8.8: Distribution of the impact parameter b from Au+Au collisions in IMAGO simulation in the centrality bin 20-30%.

8.2 Introducing initial transverse momentum

So far, quite common elements of Glauber Monte Carlo modelling were discussed. In this section, however, a new feature of the IMAGO model is presented. As explained earlier, we would like to introduce more elliptic flow to the simulation of the collision using vHLLE hybrid model with Glauber model as initial state generator. In order to base the elliptic flow addition on some physical mechanism, we have decided to implement a procedure for deposition of certain amount of the transverse momentum to every participant in each binary collision.

The idea is, that in every binary collision between the nucleons, the vector of distance between the nucleon centers is computed. This vector defines a direction, in which the transverse momentum is deposited in a form of p_T -kick. The size of such a kick is the parameter of the model. Of course, as the nucleons travel the opposite direction in the collision, the transverse momentum is deposited in relatively opposite direction for each nucleon. Nevertheless, the size of the p_T -kick is the same for both of the participants. A simple sketch of such binary collision with the directions of the p_T deposited can be seen in Fig.8.9.

Such deposited p_T -kicks from every binary collision of given nucleon are then summed to create final transverse momentum of the source. Doing so for every nucleon, one obtains a 2-dimensional initial transverse momentum profile of an event. Moreover, we expect that the total p_T shall point outwards from the *center of mass* of the collision, since there are more nucleons near the center of the nucleus than at its edge.

This procedure of introducing the initial transverse momentum, is in fact a random walk in p_T space, where the randomness is given by the distribution of the nucleons inside of the nuclei.

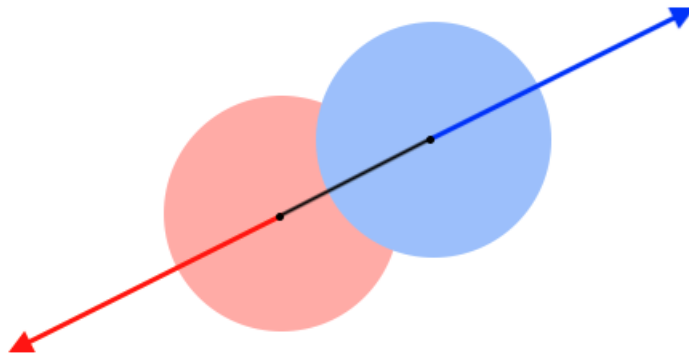


Fig. 8.9: An illustration of a binary collision. The arrows show the direction of respective p_T -kick during the IMAGO simulations. Both of the p_T -kicks has the same magnitude.

8.2.1 Output from IMAGO

The basic output from the IMAGO code is .dat file and the prefix denotes the number of the simulation. In the file, the basic quantities are written in the form

$$x \quad y \quad c \quad p_x \quad p_y,$$

where x and y are the coordinates of the source in the transversal plane in units of fm, c denotes the number of the binary collisions and p_x , resp. p_y are the components of the total transverse momentum of the source in units of GeV. In order to distinguish between the two colliding nuclei, for one of them the c values are positive and for the other one the values have negative sign.

8.3 Implementing initial p_T into vHLL hydro

Since part of the energy in the collision is deposited in the form of the p_T -kicks, the energy deposition in the initial state of the hydrodynamics must be altered. Let us discuss the procedure of transforming the output from IMAGO model into the fluid.

First, as the sources in the output from IMAGO are point-like, the energy density, baryon density and also transverse momentum need to be smeared in the transversal plane. This is done as suggested in [19] and [20]. The smearing in the transverse plane has the Gaussian form

$$g_i(x, y) = \frac{1}{2\pi\sigma_{\perp}^2} \exp\left(-\frac{(x-x_i)^2 + (y-y_i)^2}{2\sigma_{\perp}^2}\right), \quad (8.6)$$

where x_i , resp. y_i are the positions of the i -th source and $\sigma_{\perp} = 0.4$ fm is the width of the Gaussian.

Nonetheless, the transverse smearing is not the only procedure here. As the output from the Glauber model is only in the transverse plane, the profile needs to be prolonged into the rapidity. However, the energy density and the baryon density have different profiles in the rapidity.

The energy density is distributed with a plateau in the mid-rapidity which has then Gaussian tails at the ends. The form of the distribution is

$$f(\eta_{\parallel}) = \exp\left(-\frac{(\eta_{\parallel} - \eta_0)^2}{2\sigma_{\eta}} \Theta(|\eta_{\parallel}| - \eta_0)\right), \quad (8.7)$$

and $\eta_0 = \eta_0(\sqrt{s_{NN}}, N_{part})$ is the width of the plateau and $\sigma_{\eta} = \sigma_{\eta}(\sqrt{s_{NN}}, N_{part})$ is the width of the Gaussian tails. The $\Theta(|\eta_{\parallel}| - \eta_0)$ denotes the Heaviside function.

On the other hand, the baryon density is distributed by

$$h(\eta_{\parallel}) = \frac{1}{\sigma_n \sqrt{2\pi}} \exp\left(-\frac{(\eta_{\parallel} - |\eta_{n,0}|)^2}{2\sigma_n}\right), \quad (8.8)$$

where $\eta_{n,0} = \eta_{n,0}(\sqrt{s_{NN}}, N_{part})$ and $\sigma_n = \sigma_n(\sqrt{s_{NN}}, N_{part})$. This arrangement is quite different from the energy density distribution, since the baryon number is distributed in two peaks symmetrically in the rapidity. The parameters of the distributions (8.10), (8.8) are energy and centrality dependent, and for the collision energy $\sqrt{s_{NN}} = 27$ GeV they can be parametrized (see [35]) as

$$\begin{aligned}
\eta_0 &= 0.888 - 0.213 \frac{N_{part}}{2A} \\
\sigma_\eta &= 1.088 - 0.213 \frac{N_{part}}{2A} \\
\eta_{n,0} &= 1.332 - 0.319 \frac{N_{part}}{2A} \\
\sigma_n &= 0.788 - 0.213 \frac{N_{part}}{2A}.
\end{aligned} \tag{8.9}$$

The initial transverse momentum is distributed in the same manner as the baryon density. Naturally, the total energy is normalized to $\frac{N_{part}}{2} \sqrt{s_{NN}}$, the total baryon number to N_{part} and the transverse momentum is normalized to the total transverse momentum produced in IMAGO simulation. As a result, one obtains all densities distributed in three dimensions, and thus the initial fluid is created.

Second, the rest energy in each of the hydrodynamic cells has to be recomputed, because of the deposition of the part of the energy in the form of transverse momentum. Let us denote ε the original energy density without any initial transverse momentum. Since the total energy has to be conserved, the new rest energy is then

$$E_{rest} = \sqrt{E^2 - p_T^2} = \sqrt{E^2 - p_x^2 - p_y^2}, \tag{8.10}$$

and surely, the condition $E > |p_T|$ must be kept. The initial velocity of given hydrodynamic cell is then given by known formula

$$\vec{\beta} = \frac{\vec{p}_T}{E}, \tag{8.11}$$

where E is the energy, $\vec{p}_T = (p_x, p_y)$ and $\vec{\beta} = (\beta_x, \beta_y)$.

Some of the density profiles of the initial fluid can be seen in Fig.8.10-8.14 for several rapidity values. The size of the p_T -kick in data presented in Fig.8.10-8.14 is 200 MeV.

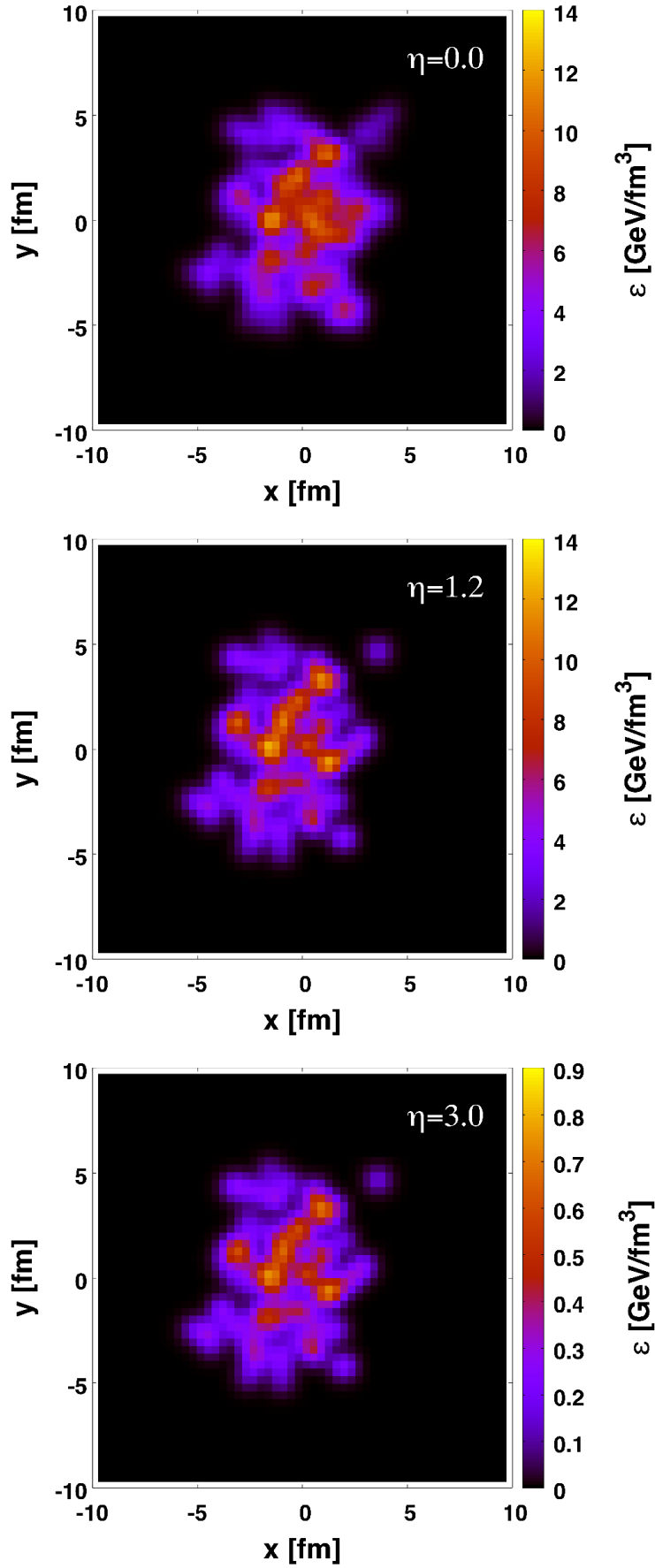


Fig. 8.10: An example of energy density ε profile before hydrodynamic evolution in Au+Au collision from IMAGO at collision energy $\sqrt{s_{NN}} = 27$ GeV and centrality 20-30%. The profiles for constant pseudorapidity η cuts are shown.

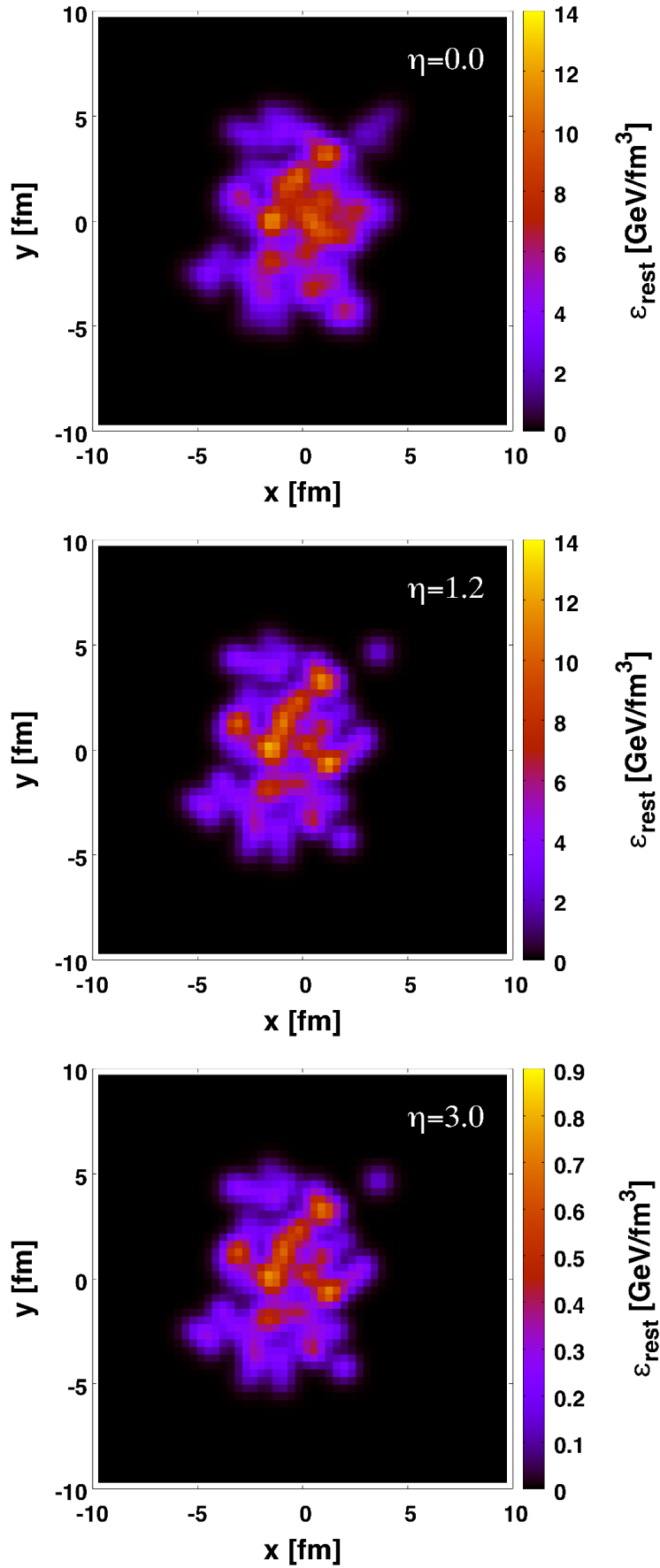


Fig. 8.11: An example of energy density ϵ_{rest} profile after subtraction of the initial p_T -kick before hydrodynamic evolution in Au+Au collision from IMAGO at collision energy $\sqrt{s_{NN}} = 27$ GeV and centrality 20-30%. The profiles for constant pseudorapidity η cuts are shown.

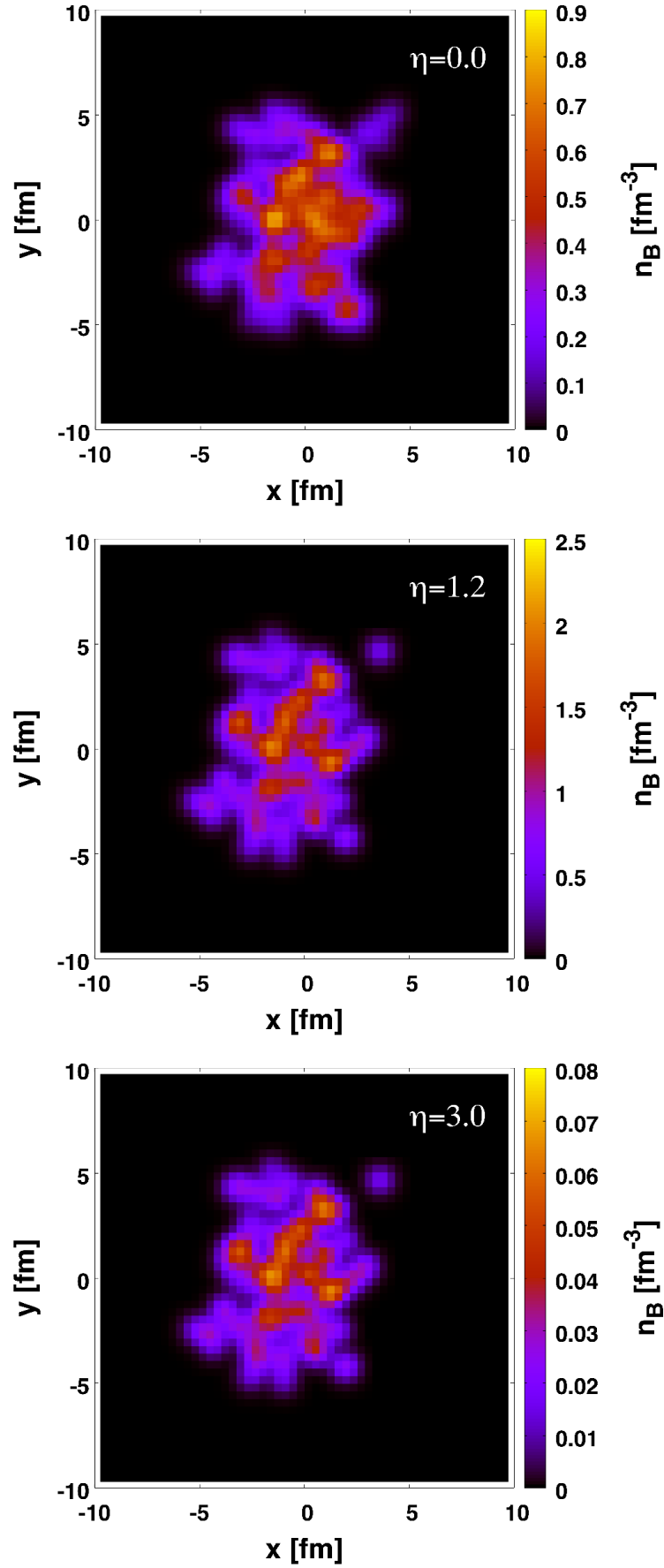


Fig. 8.12: An example of baryon density n_B profile before hydrodynamic evolution in Au+Au collision from IMAGO at collision energy $\sqrt{s_{NN}} = 27$ GeV and centrality 20-30%. The profiles for constant pseudorapidity η cuts are shown.

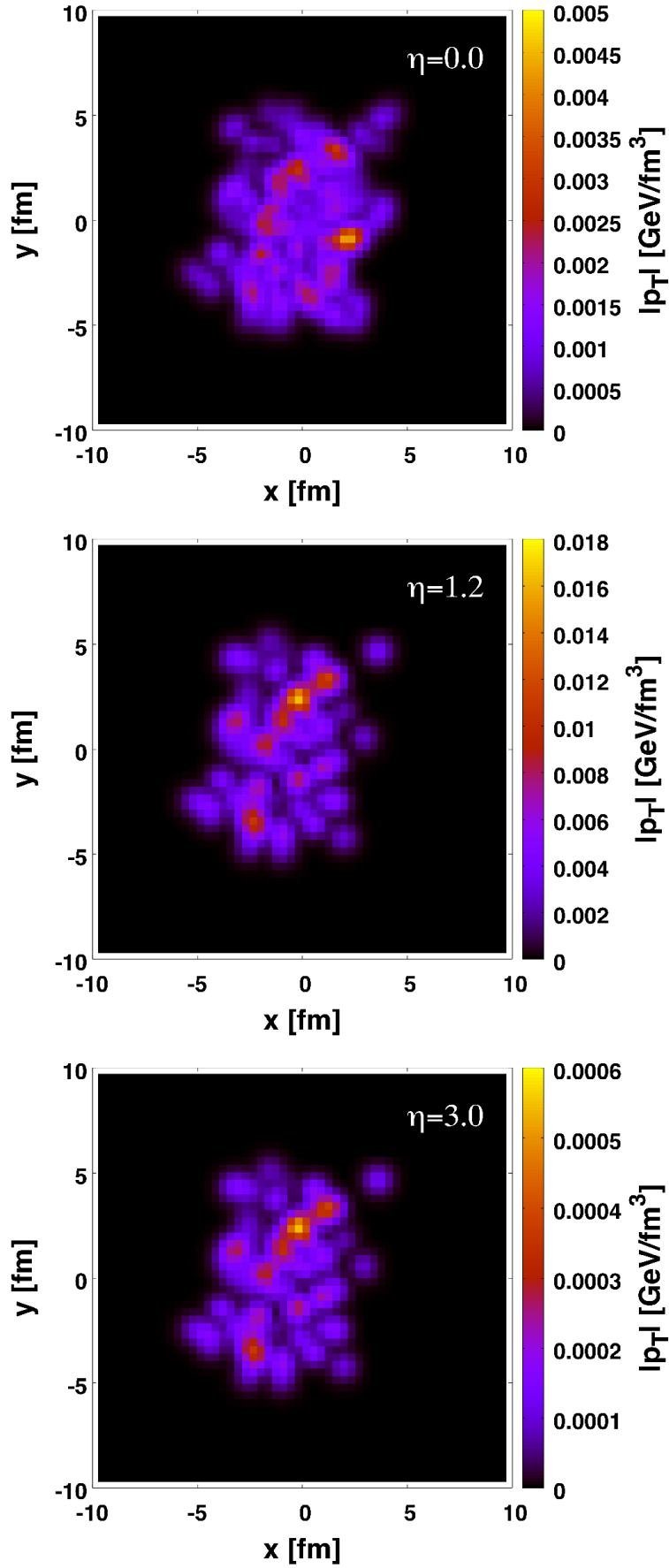


Fig. 8.13: An example of transverse momentum magnitude density $|p_T|$ profile before hydrodynamic evolution in Au+Au collision from IMAGO at collision energy $\sqrt{s_{NN}} = 27$ GeV and centrality 20-30%. The profiles for constant pseudorapidity η cuts are shown.

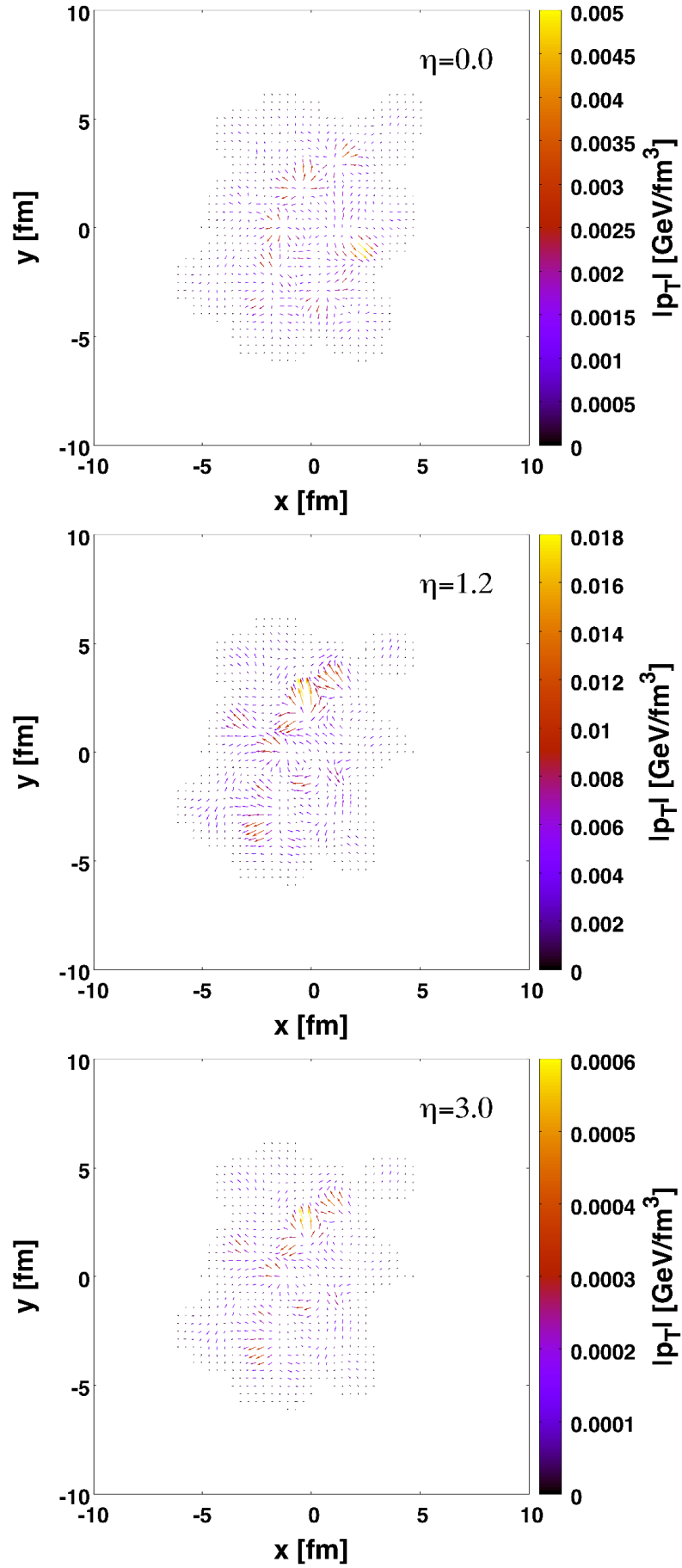


Fig. 8.14: An example of transverse momentum density $|p_T|$ profile before hydrodynamic evolution in Au+Au collision from IMAGO at collision energy $\sqrt{s_{NN}} = 27$ GeV and centrality 20-30%. The profiles for constant pseudorapidity η cuts are shown. The arrows show the direction of the p_T .

Chapter 9

Results

Using the vHLLE hybrid package, the Au+Au collisions at collision energy $\sqrt{s_{NN}} = 27$ GeV were simulated. As an initial state generator, the Glissando and the IMAGO codes were used. The new setup with SMASH was used for final state simulations. The simulations were done for three centrality classes - 10-20%, 20-30% and 30-40%. Results for several p_T -kicks in the IMAGO model are also presented.

Firstly, let us have a look at the results using the Glissando code after the bulk viscosity was introduced into the hydrodynamics and also to the hadronSampler. In comparison to the setup without any bulk viscosity (see Fig.9.1), both the elliptic flow values and the positive pion p_T spectrum for the centrality 20-30% seems to match the STAR data quite well. The bulk viscosity essentially suppresses the radial expansion of the fireball, that is why the spectrum seems steeper, and presumably redistributes the momenta in such a way, that the overall elliptic flow has higher values, so the dependence matches the experimental data. But this is only true for the centrality bin 20-30%. For the centrality 10-20% the values of the elliptic flow are generally higher than those from STAR (see Fig.9.2), but the p_T spectrum quite matches the experimental data, except for lower momenta. In the less central centrality bin 30-40%, the values of the elliptic flow are lower than STAR data and the spectrum does quite match again. The bulk viscosity helps to improve the simulations, but there is still some space for introduction of the initial transverse expansion. However, such initial transverse expansion can be provided by the IMAGO code by simulating initial p_T -kicks during the collision.

Let us compare the IMAGO code when the initial p_T -kick is set to zero, i.e. no initial transverse expansion is implemented, and the Glissando code. In Fig.9.2 can be seen, that the elliptic flow is generally lower from the simulations with IMAGO as initial state than from simulations using Glissando. The spectrum in Fig.9.3 is steeper for the IMAGO simulations, which endorses the fact that there is less flow. The differences between the two initial state generators in the elliptic flow dependence are less significant as the centrality of the collision decreases (i.e. higher percentage) and for the centrality class 30-40% the results are comparable. Nevertheless, the inconsistency of the two models can be influenced by two facts. First, the Glissando centrality classes were set accordingly to the distribution of wounded nucleons. On the contrary, the IMAGO centrality classes are given by the distribution of the RDS (as described in Chapter 8). Such disagreement may cause the v_2 values to differ. The other thing is, that the Glissando 2, [16], includes correction to the deformation of the gold nuclei, whereas in IMAGO the gold nucleus is considered round.

All in all, as the simulations with IMAGO results in lower elliptic flow (even for the centrality 10-20%), there is still room for improvement of the results by introducing the initial transverse expansion. It should be noted that for the simulations with IMAGO, the bulk viscosity is present in the hydrodynamics and hadronSampler as well.

In the Fig.9.2, there are values of the elliptic flow as a function of transverse momentum for several values of the initial p_T -kicks. Evidently, there is an influence on the elliptic flow,

since for the higher values of the p_T -kick the values of v_2 are also higher even in the uncertainty intervals. However, the influence on the p_T spectrum is far less apparent. Moreover, the simulations where the initial transverse expansion was introduced improve the elliptic flow p_T dependence, as the results are in better agreement with the STAR data. Nevertheless, there is one more point to that. The initial p_T kicks rather lead to “hot-spots” which tend to expand in all directions, as seen in Fig.8.14. The effect on the elliptic flow is then more pronounced for less central collisions, as the system is smaller.

It should be also noted, that the experimental data ([34]) of the elliptic flow plotted in Fig.9.2 were obtained by the η sub-event method (which is similar to the event plane method, only the particles are taken from the opposite hemisphere in pseudorapidity) and the results from the simulations are computed via two-particle cumulant method. However, since there is no non-flow in the simulations, both of the results should be in good agreement.

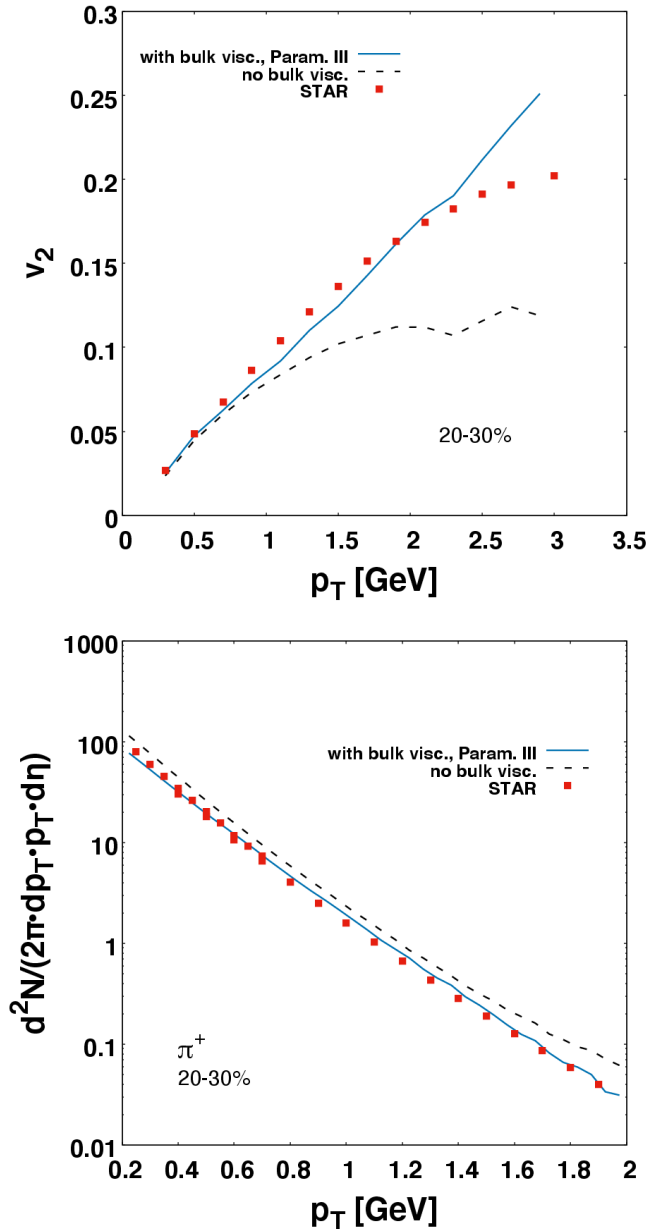


Fig. 9.1: The elliptic flow p_T dependence (upper) and positive pion p_T spectrum (lower) in Au+Au collisions at $\sqrt{s_{NN}} = 27$ GeV and centrality 20-30% from simulations using Glissando. The black line represents simulations before the bulk viscosity was implemented into the hydrodynamics and before switching to the SMASH hadronSampler. The orange line correspond to the simulations with bulk viscosity and SMASH.

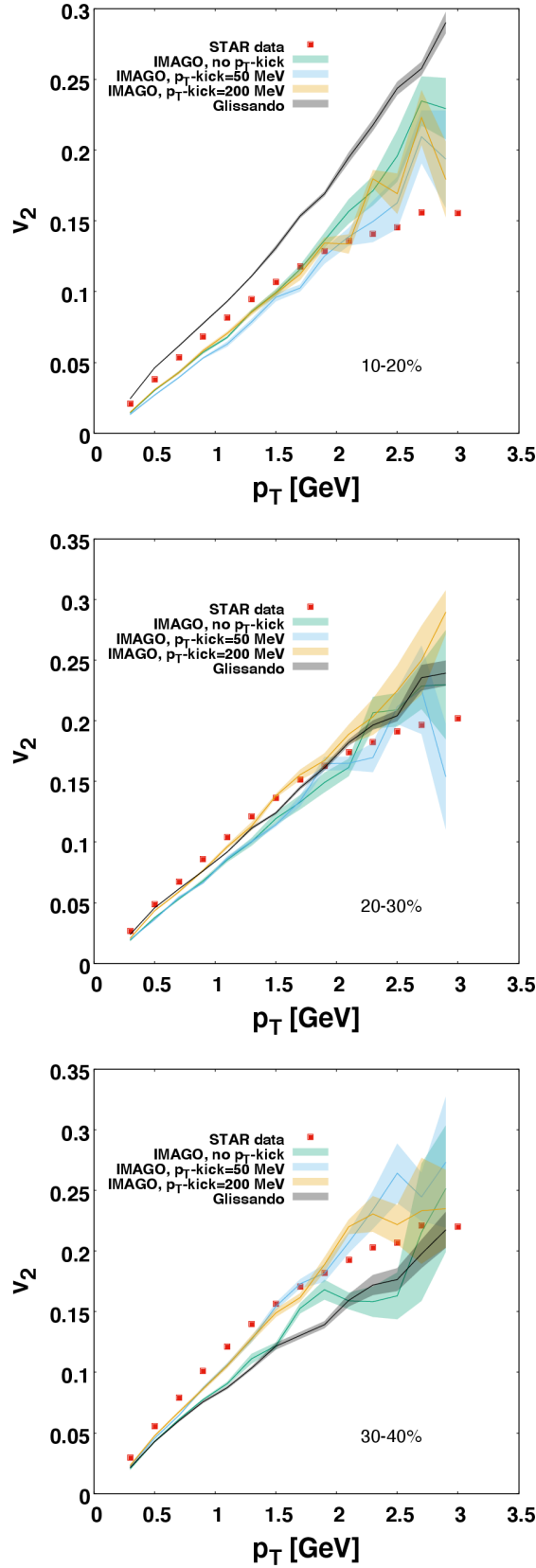


Fig. 9.2: The elliptic flow p_T dependence in Au+Au collisions at $\sqrt{s_{NN}} = 27$ GeV from simulations with IMAGO for different p_T -kicks and also using Glissando for comparison. The results are presented for three centrality classes - 10-20% (upper), 20-30% (middle) and 30-40% (lower). The black line corresponds to the simulations with Glissando, whereas the colored lines represent various p_T -kicks in IMAGO. The elliptic flow values from simulations were computed by two particle cumulant method. The STAR data were taken from [34] (Fig.6.5 for 10-20%, 30-40% and Fig.6.3 for 20-30%) and obtained by η sub-event method.

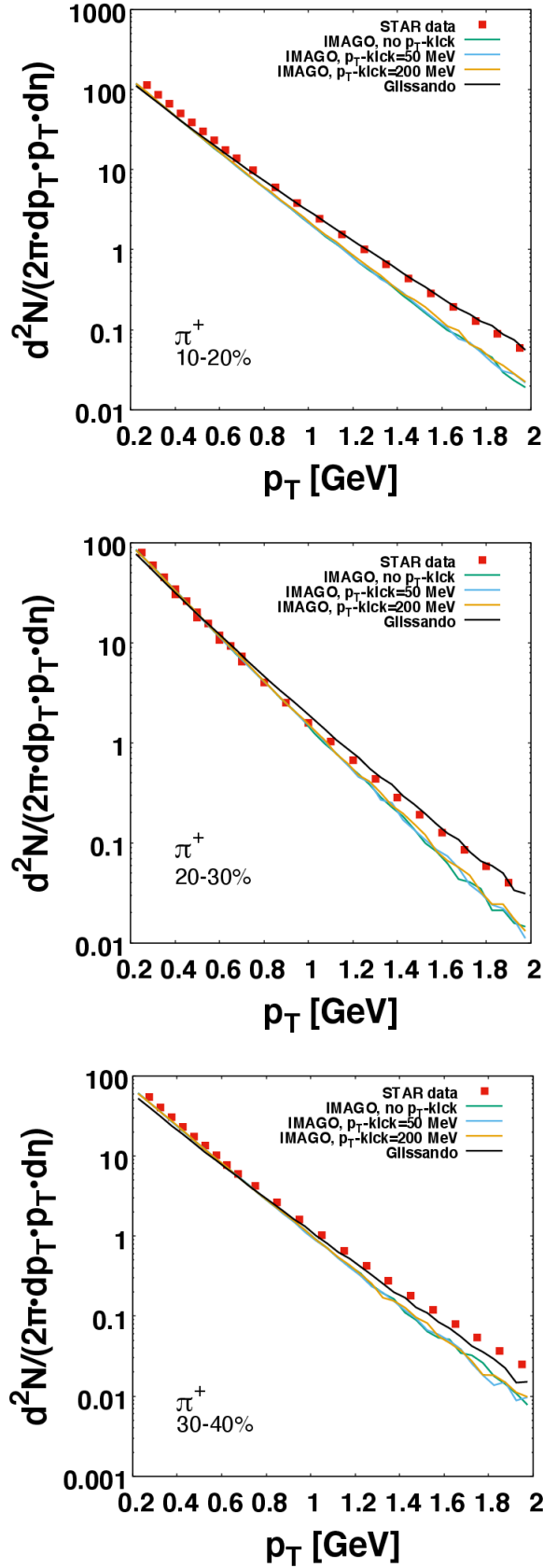


Fig. 9.3: The positive pion spectra from Au+Au collisions at $\sqrt{s_{NN}} = 27$ GeV from simulations with IMAGO for different p_T -kicks and also using Glissando for comparison. The results are presented for three centrality classes - 10-20% (upper), 20-30% (middle) and 30-40% (lower). The black line corresponds to the simulations with Glissando, whereas the colored lines represent various p_T -kicks in IMAGO. The STAR data were taken from [33] (Fig.6.2).

Conclusion

For the description of strongly interacting matter it is essential to study its phase diagram, which is, however, determined by the equation of state. A method how to study the equation of state is by means of the models for collective evolution of matter during heavy-ion collisions. Since the energy in the collision is not distributed evenly, the matter evolves anisotropically. Therefore, one of the signs of collective behaviour is anisotropic flow, which reflects the momentum anisotropy of the fireball.

Experimentally, there is an effort to probe the phase diagram at lower energies by the RHIC BES program. Some of the results reported by the STAR collaboration can be found in this work.

The efficient way to for modelling the medium in the phase of quark-gluon plasma is by means of hydrodynamic approach. Nevertheless, the evolution is highly influenced by the shape of the initial conditions for the hydrodynamic code.

In this work, a particular hydrodynamic code vHLLE is presented together with basics of the hydrodynamic modelling. In addition, the Glauber initial state generator Glissando and final state simulator SMASH are described. However, the results of the simulations of Au+Au collisions at RHIC BES energies using vHLLE with Glissando for initial conditions do not match the experimental data presented by STAR collaboration. In particular, the values of the elliptic flow as a function of transverse momentum are considerably underpredicted. The main motivation for this work is, in fact, to improve the results for vHLLE simulations with Glauber initial conditions.

At the same time, the vHLLE hydrodynamic code was improved by introducing bulk viscosity into the model. In addition to that, the final state simulator was updated to the SMASH transport code with bulk viscosity corrections.

The simulations with the bulk viscosity implemented in the code are overall improved in comparison to the previous simulations with no bulk viscosity. As the elliptic flow dependence on the transverse momentum may be improved, the outcome is still not satisfactory for all available centrality classes.

Bearing the motivation in mind, we have decided to create a new Glauber Monte Carlo model which allows for an initial transverse expansion of the fireball. It is done by means of transverse momentum deposition directly during the simulation of the collision as a random walk in p_T space with the magnitude of the one momentum deposition in one binary collision as a parameter of the model. The new model was calibrated and the centrality classes were determined.

From the comparison of the results from the Glissando and the new model (IMAGO) it is clear that the new model produces less flow, both radial and elliptic. However, unlike in the Glissando, in the new model an initial transverse expansion can be provided by setting the value of the magnitude of the momentum deposition. Such a choice of the parameter affects the elliptic flow dependence in favour for the STAR data description, but does not have a significant influence on the p_T spectra.

As an outlook for this work, there might be a possibility to alter the momentum deposition parameter in the new model simultaneously with the bulk viscosity, in order to set the corresponding values, which would be satisfactory for all of the centrality classes.

Bibliography

- [1] G. Dissertori, *The Determination of the Strong Coupling Constant*, Adv. Ser. Direct. High Energy Phys. **26** (2016), 113-128.
- [2] A. Bazavov *et al.* [HotQCD], *Chiral crossover in QCD at zero and non-zero chemical potentials*, Phys. Lett. B **795** (2019), 15-21.
- [3] R. S. Bhalerao, *Relativistic heavy-ion collisions*, AEPSHEP (2012), 219-239.
- [4] J. D. Bjorken, *Highly Relativistic Nucleus-Nucleus Collisions: The Central Rapidity Region*, Phys. Rev. D **27** (1983), 140-151.
- [5] D. Ter Haar, ON MULTIPLE PRODUCTION OF PARTICLES DURING COLLISIONS OF FAST PARTICLES, *Collected Papers of L.D. Landau*, Pergamon, 1965, Pages 569-585, ISBN 9780080105864.
- [6] A. Bazavov *et al.* [HotQCD], *Equation of state in (2+1)-flavor QCD*, Phys. Rev. D **90** (2014), 094503.
- [7] PARTICLES AND FRIENDS, *Evolution of collisions and QGP*, [Cit. 26.4.2022], available at: <https://particlesandfriends.wordpress.com/2016/10/14/evolution-of-collisions-and-qgp/>
- [8] S. Acharya *et al.* [ALICE], *Transverse momentum spectra and nuclear modification factors of charged particles in pp, p-Pb and Pb-Pb collisions at the LHC*, JHEP **11** (2018), 013.
- [9] M. L. Miller, K. Reygers, S. J. Sanders and P. Steinberg, *Glauber modeling in high energy nuclear collisions*, Ann. Rev. Nucl. Part. Sci. **57** (2007), 205-243.
- [10] R. Pasechnik and M. Šumbera, *Phenomenological Review on Quark–Gluon Plasma: Concepts vs. Observations*, Universe **3** (2017) no.1, 7.
- [11] P. F. Kolb and U. W. Heinz, *Hydrodynamic description of ultrarelativistic heavy ion collisions*, Quark-gluon plasma 4 (2003), 634-714, [arXiv:nucl-th/0305084 [nucl-th]].
- [12] K. Aamodt *et al.* [ALICE], *Elliptic flow of charged particles in Pb-Pb collisions at 2.76 TeV*, Phys. Rev. Lett. **105** (2010), 252302.
- [13] C. Gale, S. Jeon and B. Schenke, *Hydrodynamic Modeling of Heavy-Ion Collisions*, Int. J. Mod. Phys. A **28** (2013), 1340011.
- [14] M. Bleicher, E. Zabrodin, C. Spieles, S. A. Bass, C. Ernst, S. Soff, L. Bravina, M. Belkacem, H. Weber and H. Stoecker, *et al. Relativistic hadron hadron collisions in the ultrarelativistic quantum molecular dynamics model*, J. Phys. G **25** (1999), 1859-1896.
- [15] W. Broniowski, M. Rybczynski and P. Bozek, *GLISSANDO: Glauber initial-state simulation and more...*, Comput. Phys. Commun. **180** (2009), 69-83.

- [16] M. Rybczynski, G. Stefanek, W. Broniowski and P. Bozek, *GLISSANDO 2 : GLauber Initial-State Simulation AND mOre...*, ver. 2, Comput. Phys. Commun. **185** (2014), 1759-1772.
- [17] P. Bożek, W. Broniowski, M. Rybczynski and G. Stefanek, *GLISSANDO 3: GLauber Initial-State Simulation AND mOre...*, ver. 3, Comput. Phys. Commun. **245** (2019), 106850.
- [18] J. S. Moreland, J. E. Bernhard and S. A. Bass, *Alternative ansatz to wounded nucleon and binary collision scaling in high-energy nuclear collisions*, Phys. Rev. C **92** (2015) no.1, 011901.
- [19] P. Bożek and W. Broniowski, *Transverse-momentum fluctuations in relativistic heavy-ion collisions from event-by-event viscous hydrodynamics*, Phys. Rev. C **85** (2012), 044910.
- [20] P. Bożek, W. Broniowski and A. Olszewski, *Hydrodynamic modeling of pseudorapidity flow correlations in relativistic heavy-ion collisions and the torque effect*, Phys. Rev. C **91** (2015), 054912.
- [21] S. Ryu, J. F. Paquet, C. Shen, G. Denicol, B. Schenke, S. Jeon and C. Gale, *Effects of bulk viscosity and hadronic rescattering in heavy ion collisions at energies available at the BNL Relativistic Heavy Ion Collider and at the CERN Large Hadron Collider*, Phys. Rev. C **97** (2018) no.3, 034910.
- [22] B. Schenke, C. Shen and P. Tribedy, *Multi-particle and charge-dependent azimuthal correlations in heavy-ion collisions at the Relativistic Heavy-Ion Collider*, Phys. Rev. C **99** (2019) no.4, 044908.
- [23] B. Schenke, C. Shen and P. Tribedy, *Running the gamut of high energy nuclear collisions*, Phys. Rev. C **102** (2020) no.4, 044905.
- [24] I. Karpenko, P. Huovinen and M. Bleicher, *A 3+1 dimensional viscous hydrodynamic code for relativistic heavy ion collisions*, Comput. Phys. Commun. **185** (2014), 3016-3027.
- [25] J. Bobek, *Effects of Bulk Viscosity of the Quark-Gluon Plasma in Hydrodynamic Approach* [Research project], CTU, FNSPE, 2021, [Cit. 24.4.2022], available at: https://physics.fjfi.cvut.cz/publications/ejcf/VU_Josef_Bobek.pdf
- [26] J. Weil, V. Steinberg, J. Staudenmaier, L. G. Pang, D. Oliinychenko, J. Mohs, M. Kretz, T. Kehrenberg, A. Goldschmidt and B. Bäuchle, *et al. Particle production and equilibrium properties within a new hadron transport approach for heavy-ion collisions*, Phys. Rev. C **94** (2016) no.5, 054905.
- [27] I. A. Karpenko, P. Huovinen, H. Petersen and M. Bleicher, *Estimation of the shear viscosity at finite net-baryon density from A + A collision data at $\sqrt{s_{NN}} = 7.7 - 200$ GeV*, Phys. Rev. C **91** (2015) no.6, 064901.
- [28] A. Schäfer, I. Karpenko, X. Y. Wu, J. Hammelmann and H. Elfner, *Particle production in a hybrid approach for a beam energy scan of Au+Au/Pb+Pb collisions between $\sqrt{s_{NN}} = 4.3$ GeV and $\sqrt{s_{NN}} = 200.0$ GeV*.
- [29] <https://github.com/smash-transport/smash-hadron-sampler>
- [30] M. McNelis and U. Heinz, *Modified equilibrium distributions for Cooper–Frye particlization*, Phys. Rev. C **103** (2021) no.6, 064903.

- [31] S. Pratt and G. Torrieri, *Coupling Relativistic Viscous Hydrodynamics to Boltzmann Descriptions*, Phys. Rev. C **82** (2010), 044901.
- [32] G. Odyniec [STAR], *Beam Energy Scan Program at RHIC (BES I and BES II) – Probing QCD Phase Diagram with Heavy-Ion Collisions*, PoS **CORFU2018** (2019), 151.
- [33] L. Adamczyk *et al.* [STAR], *Bulk Properties of the Medium Produced in Relativistic Heavy-Ion Collisions from the Beam Energy Scan Program*, Phys. Rev. C **96** (2017) no.4, 044904.
- [34] L. Adamczyk *et al.* [STAR], *Inclusive charged hadron elliptic flow in Au + Au collisions at $\sqrt{s_{NN}} = 7.7 - 39$ GeV*, Phys. Rev. C **86** (2012), 054908.
- [35] J. Cimeterman, I. Karpenko, B. Tomášik and B. A. Trzeciak, *A benchmark of initial state models for heavy-ion collisions at $\sqrt{s_{NN}} = 27$ and 62 GeV*, Phys. Rev. C **103** (2021) no.3, 034902.
- [36] J. Štěrba, *Initial conditions for hydrodynamic simulations of collisions at RHIC-BES energies* [Research project], CTU, FNSPE, 2021, [Cit. 24.4.2022], available at: https://physics.fjfi.cvut.cz/publications/ejcf/VU_Jakub_Sterba.pdf
- [37] R. Snellings, *Elliptic Flow: A Brief Review*, New J. Phys. **13** (2011), 055008.
- [38] P. Romatschke and U. Romatschke, *Relativistic Fluid Dynamics In and Out of Equilibrium* Cambridge University Press, 2019, ISBN 9781108651998.
- [39] D. S. Balsara, *Numerical PDE Techniques for Scientists and Engineers*, [Cit. 24.4.2022], available at: https://www3.nd.edu/~dbalsara/Numerical-PDE-Course/ch5/Chp5_RP_Euler.pdf
- [40] A. Deur, S. J. Brodsky and G. F. de Teramond, *The QCD Running Coupling*, Nucl. Phys. **90** (2016), 1.
- [41] B. A. Trzeciak, I. Karpenko, *Selected topics from relativistic nucleus-nucleus collisions* [lecture], CTU, FNSPE, academic year 2020/2021
- [42] K. Křížková Gajdošová, *Physics of ultrarelativistic heavy-ion collisions* [lecture], CTU, FNSPE, academic year 2020/2021
- [43] K. Šafařík, Heavy Ions (High-Energy Physics), *Encyclopedia of Physical Science and Technology (Third Edition)*, Academic Press, 2003, Pages 293-307, ISBN 9780122274107.